An Analytical Approach for Assisting Scoliosis Brace Casting

by
Steffen Adria

A thesis submitted in partial fulfillment of the requirements for the degree of

Master of Science

Department of Biomedical Engineering
University of Alberta

Abstract

Adolescent idiopathic scoliosis (AIS) is a spinal disorder causing abnormal curvature of the spine in three dimensions (3D), starting in the patient's adolescence, and having no known cause. Bracing is the most common non-surgical method of treating AIS, but the brace design is heavily reliant on orthotists' experience. As more research is done, objective approaches have been shown to lead to more consistent results. Thus, numerical analysis of brace treatment and better brace construction are the focus of this research. The aims of this research are to 1) generate a mathematical model to estimate spinal flexibility to assist brace treatment; 2) develop and test a 3D brace casting frame to assist orthotists to make braces; and 3) design a simulation algorithm to predict the casting outcomes.
The mathematical model of spinal flexibility used a single-variable linear regression as a function of 5 predictor variables to determine the best predictors. Fourteen patients' data were used to develop and validate the model. The highest coefficient of determination was 0.43 for thoracic curve with the length of the curve acting as the predictor.

In addition, a novel brace casting frame was designed and built to hold a patient in place with forces applied to the body in three-dimensions. Force and angle measurements were recorded during casting for modeling purposes. The frame had been used in brace casting clinics on two occasions, demonstrating its durability and feasibility to assist brace casting.

The correction algorithm was developed in MATLAB using lumped element analysis, based on data from radiographs and spinal flexibility information from ultrasound measurements. The pads' force magnitudes and locations were simulated to obtain the optimal in-brace correction, with an allowed force value between -70 N and +70 N. The forces could take 5 values between these limits and the program was iterated with progressively smaller windows. Promising simulation results were obtained on a sample of 11 patients, including one validated in the clinic, with results within reasonable deviation

of the actual in-brace corrections. This research ultimately will allow an increase in the objectification and quantification of brace casting for AIS, leading to better brace treatment.

Preface

This thesis is an original work by Steffen Adria.

The research project, of which this thesis is a part, received research ethics approval from the University of Alberta Research Ethics Board "Determine the Optimum Applied Pressure for the Brace Treatment of Scoliosis", No. 00028133, March 1 2012 – February 28, 2017; and "Determine the Curve Flexibility with Adolescent Idiopathic Scoliosis Using Ultrasound", No. 00042282, October 1, 2013 - September 26, 2018

Portions of the material in this thesis have been published and presented:

S. Adria, E. Lou, "Understanding Real-time 3D Spinal Curvature Response to Improve Brace Treatment for Scoliosis**".** Glenrose Summer Student Summer Camp, August 14, 2015. To produce this presentation, I performed a literature review and improved devices for measuring the response of scoliotic curves to mechanical forces, followed by the actual collection and analysis of the data. Dr. Lou provided the basic devices that I improved and assisted in all stages, particularly with designing the methodology. I prepared and presented the finished presentation.

S. Adria, E. Lou, "Can Spinal Flexibility Be Predicted for Female Brace Patients With Adolescent Idiopathic Scoliosis (AIS)?" Women's and Children's Health Institute Research Day, November 26, 2016. I gathered much of the raw data, while Dr. Lou furnished some of the rest. I performed the mathematical analysis with Dr. Lou's assistance in designing the methods. I prepared and presented the poster.

S. Adria, E. Lou, "Prediction of curve flexibility using demographic and radiographic information for girls with adolescent idiopathic scoliosis (AIS)". Faculty of Engineering Graduate Research Symposium FEGRS 2016. June 22, 2016. I gathered more raw data here, partly using Dr. Lou's data. I created the analysis method, partly based on prior work by Dr. Lou and me. Dr. Lou assisted in the creation of my analysis program in MATLAB. I prepared and presented the poster.

Acknowledgements

I would like to thank Dr. Edmond Lou for his endless patience, guidance and support. I would like to thank Dr. Kajsa Duke for her insightful advice in technical matters.

I would also like to thank NSERC for its generous financial support, making this thesis possible.

My lab mates, especially Andrew, Kenwick, Rachel and Fraaz, were always there for my inquiries.

Finally, I would like to thank Maisie Goh because she is always super helpful any time administrative issues arise.

Table of Contents

Chapter 1: Introduction 1

1.1 Motivation 2

1.2 Hypotheses 2

1.3 Objectives 3

1.4 Outline of Thesis 3

Chapter 2: Background 4

2.0 Summary 4

2.1 Anatomy of the Spine 4

2.2 Scoliosis Overview 6

2.3 Brace Treatment 10

2.3.1 CTLSO 10

2.3.2 TLSO 10

2.3.3 Night-Time Brace 12

2.3.4 Brace Construction 12

2.3.4.1 Plaster Casting 12

2.3.4.2 Plaster and CAD/CAM Casting 13

2.3.4.3 Surface Topography and CAD/CAM Casting 13

2.4 Numerical Modeling of Scoliosis 13

2.5 Conclusion 14

Chapter 3: Principles and Construction of Six Commonly Used Braces in the Treatment of Adolescent Idiopathic Scoliosis 16

3.0 Summary 16

3.1 Brace Construction and Principles 16

3.1.1 Boston Brace 17

3.1.2 Chêneau Brace 18

3.1.3 Lyon ARTbrace 19

3.1.4 Providence Brace 19

3.1.5 Charleston Brace 21

3.1.6 Glenrose Custom Brace 21
3.2 Biomechanics of Bracing 22
3.2.1 Passive Mechanisms 22
3.2.2 Active Forces 24
3.2.3 IVD Swelling 25
3.3 Current 3D Concepts of Bracing 25
3.4 Factors Affecting Brace Effectiveness 27
3.4.1 Curve Severity 28
3.4.2 Curve Location 28
3.4.3 Spinal Flexibility 28
3.4.4 Gender 29
3.4.5 Skeletal Maturity 29
3.4.6 Adherence 30
3.4.7 Brace Wear Quality 31
3.4.8 In-Brace Correction 31
3.5 Conclusion 32
Chapter 4: Development of a Linear Regression Model to Estimate Spinal Flexibility for Brace Candidates with Adolescent Idiopathic Scoliosis 33
4.0 Summary 33
4.1 Importance of Flexibility of the Scoliotic Spine 33
4.1.1 Review of Different Methods to Measure Flexibility 34
4.2 A Pilot Study to develop a model to predict Spinal Flexibility 39
4.2.1 Patient Selection 39
4.2.2 Method of Determining Curve Flexibility 39
4.2.3 Factors for the Spinal Flexibility Model 40
4.2.4 Data Measurements 41
4.2.5 Model Development and Analysis 42
4.3 Results 46

4.3.1 Intra-rater Reliability and Accuracy 46
4.3.2 Factors and Flexibility 46
4.3.3 Regression Results 47
4.4 Discussion 49
4.5 Conclusion 50
Chapter 5: Development and Validation of 3D Brace Casting Frame for Assisting Brace Design 51
5.0 Summary 51
5.1 Review of Existing Casting Methods 51
5.2 Frame Construction 54
5.2.2 Tools Used to Construct Brace Frame 55
5.2.3 Design Criteria 56
5.2.4 Existing Design: Aluminum Collar Clamp on Metal Frame 56
5.2.5 Design Process 59
5.2.6 Three-Dimensional Wooden Frame 60
5.2.7 Bolster Supports 61
5.2.7.1 Construction Tools for Bolster Holders 61
5.2.8 Plastic Collar Clamp (CP) Bolster Holder 62
5.2.9 Plastic Collar Clamp with Rubber 65
5.2.10 Screw System 66
5.2.11 Steel Collar Clamp 67
5.2.12 Final Bolster Support Design 69
5.3 Challenges in Constructing Frame 71
5.4 Experiments and Validation 71
5.4.1 Pressure and Angle Sensor Measurements 72
5.4.1.1 Angle Measurements Accuracy and Reliability 72
5.4.1.2 Determination of the Accuracy and Reliability of Pressure Sensors 75
5.4.1.3 Force Testing for Airbags 76
5.4.2 Validity of the 3D frame Design in Laboratory Setting 79
5.5 Preliminary Clinical Trial 82
5.5.1 Evaluation of the 3D Frame with Subject with AIS 82

5.6 Conclusion 88

Chapter 6: Development of Simulation of Pad Placement for Use with Brace Casting Frame 89

6.0 Summary 89
6.1 Literature Review of Numerical Simulation of Scoliosis Bracing 89
6.2 Motivation 90
6.3 Simulation Model and Method 90
6.3.1 Subjects for Model Development and Validation 91
6.3.1 Geometry of the Spine 92
6.3.2 Mechanical Properties of the Spine 94
6.3.2.1 Personalization of Simulation to Specific Patients 95
6.3.2.2 Beam Bending Model 96
6.3.3 Analysis Method 98
6.4 Results of Simulation and Comparison to In-Brace Results 100
6.4.2 Accuracy of Geometry Acquisition 107
6.4.3 Simulation Evaluation on Subject 11 109
6.4.4 Linearity 111
6.5 Discussion 111
6.6 Conclusion 113

Chapter 7: Conclusion, Limitations and Future Recommendations 114

7.0 Summary 114
7.1 Contributions and Achievement 115
7.2 Future Recommendations 116

References 118

Appendix A. Results of Brace Simulation 126

Appendix B: MATLAB Code for Simulation 133

Section 1: Iterator 133
Section 2: Main Calculating Function 136
Section 3: geometryZ 144

Section 4: AlphaFinder 148
Section 5: Fergpoints 15050

List of Tables

Table 4-1: Most effective flexibility test by curve location and magnitude 37
Table 4-2: Curve summary of the 14 participants 39
Table 4-3: Data Used in Analysis 45
Table 4-4. Reliability of measurements of measured Cobb angle, AVR, bending angle and flexibility 46
Table 4-5. Sub-category means and standard deviation for each measured variable 47
Table 4-6: R^2 for all sub-categories and factors 48
Table 4-7: Median absolute residual values for all sub-categories and factors 48
Table 5-1: Calibration results for angle sensors 74
Table 5-2: Calibration results for airbags 76
Table 5-3: Subject measurements for airbag calibration procedure 77
Table 5-4: Effective Contact Area for Bolsters 78
Table 5-5: Test subject information 83
Table 5-6: Test results for patient 86
Table 6-1: Demographic and curve information for the eleven included subjects 92
Table 6-2: Pre-personalization stiffnesses 95
Table 6-3. First three segments of stiffness matrix **K** 96
Table 6-4: Overall results for the simulation process in the thoracic region 101
Table 6-5. Overall results for the simulation process in the thoracolumbar and lumbar regions 101
Table 6-6. Deviation correction 102
Table 6-7. Stiffness coefficients associated with each patient 103
Table 6-9: Radiographic and input geometry comparisons. 108
Table 6-10. Force magnitudes, force locations and results from test on subject 11. 109

List of Figures

Figure 2-1. Anatomic planes and directions from Human Anatomy 5
Figure 2-2. a) left lateral view of healthy spine b) posterior view of healthy spine 6
Figure 2-3. A postero-anterior radiograph of a patient with scoliosis and the two measured Cobb angles are 44° and 38° in thoracic and thoracolumbar curves, respectively. 7
Figure 2-4. Schematic diagram of HVP acting on a single vertebra (not to scale) 9
Figure 2-5. Anterior, lateral and posterior views of a Milwaukee (CTLSO) brace 10
Figure 2-6. A custom designed anterior-opening full-time TLSO 11
Figure 3-1. (Clockwise from top left) a) Boston brace; b) Chêneau brace; c) Lyon ARTbrace; d) Providence brace; e) Charleston bending brace; and f) Glenrose custom brace 17
Figure 3-2. A volunteer subject on a Providence stabilizing board with bolsters applied 20
Figure 3-3. Three-point bending system (simplified 2D) 23
Figure 3-5. Measurements required for Stokes method 26
Figure 3-6. Illustration of Risser sign 29
Figure 3-7. Brace treatment success rate versus wear time per day, taken from Weinstein et al., 2013 . 31
Figure 4-1. Patient undergoing fulcrum bending test for a right thoracic curve 35
Figure 4-2. A push-prone bending test is performed with a physician applying lateral forces to the patient 36
Figure 4-3. Suspension flexibility test 36
Figure 4-5. (a) The Cobb angle measurement on a PA radiograph and (b) the left prone maximum side-bending angle on an ultrasound image 40
Figure 4-6. The selected landmarks on a vertebra to measure AVR using in-house software. 42
Figure 4.7. Flowchart for development of model 43
Figure 4-8. Results for Thoracic curves with Length factor 49
Figure 5-1. Volunteer on Providence board with bolsters labeled 52
Figure 5-2. Ultrasound equipment and patient a) ultrasound console, b) position tracking system (GPS), c) ultrasound transducer 53
Figure 5-3: Pressure airbag schematic 55
Figure 5-4. Aluminum Collar Clamp on Steel Frame 57
Figure 5-5. Back of old frame, demonstrating ultrasound access slot 58
Figure 5-6. Aluminum collar clamp A 58

Figure 5-7. Rotations allowed on old frame 59
Figure 5-8. Completed frame configured for right thoracic, left lumbar curve 60
Figure 5-9. Plastic collar clamp set 62
Figure 5-10. Plastic collar clamp A 63
Figure 5-11. PCA mounted on crossbar 63
Figure 5-12. Plastic collar clamp B 64
Figure 5-13. Plastic Collar Clamp with Rubber 65
Figure 5-14. Complete Screw System 66
Figure 5-15. Screw System middle piece 66
Figure 5-16. Steel collar clamp crossbar connector 67
Figure 5-17. Mounting of SCA 68
Figure 5-18. Steel Collar Clamp Middle Rotator 68
Figure 5-19. Aluminum rod holder 69
Figure 5-20. Final design for 5 DOF 70
Figure 5-21. Axes of rotation of angle sensor 72
Figure 5-22. Rotating protractor with angle sensor attached 73
Figure 5-23. Plot of measured angle from sensor unit 1 versus actual angle from the protractor 73
Figure 5-24. Plot of measured pressure versus actual pressure for sensor 1 to allow calibration. 75
Figure 5-25. a) mounting of load cell onto bolster support, and b) a load cell 77
Figure 5-27. Ultrasound images of spine with all pad pressures set to a) 30 mmHg b) 60 mmHg and c) 90 mmHg 80
Figure 5-28. a) test with thoracic and lumbar bolsters at 90 mmHg b) test with thoracic, lumbar and trochanter bolsters at 90 mmHg 81
Figure 5-28. Radiograph taken at time of brace prescription for test subject 83
Figure 5-29. The right bending test ultrasound image. Black lines are centre-of-lamina measurements. 84
Figure 5-30. Subject standing in frame 85
Figure 5-31. a) Test 1 ultrasound image b) Test 2 ultrasound image c) Test 3 ultrasound image 87
Figure 6-1. Simulation Flowchart 91
Figure 6-2. Coordinate system used 93
Figure 6-3. The AP radiograph shows the 73 points for the geometry extraction 94
Figure 6-4. Model schematic 97
Figure 6-5. Bending moment diagram for beam model of spine 98

Figure 6-6. a) initial curve; b) Ferguson-corrected curve; c) deviation-corrected curve 100
Figure 6-7. Subject 1. 105
Figure 6-8. Subject 2. 106
Figure 6-9. Subject 3. 107
Figure 6-10. Plot of radiographic Cobb against geometry acquisition Cobb 108
Figure 6-11. Subject 11. 110
Figure 6-12. Plot of moment response of thoracic vertebrae. ϕ_z is the rotation used in this simulation 111
Figure A-1. Subject 4. 127
Figure A-2. Subject 5 127
Figure A-3. Subject 6. 128
Figure A-4. Subject 7. 129
Figure A-5. Subject 8. 130
Figure A-6. Subject 9 132
Figure A-7. Subject 10 132

List of Equations

(2-1) Stiffness of a system of finite elements 25

(4-1) Spinal flexibility equation 43

(4-2) BMI definition 52

(4-3) Standard error of measurement definition 53

(5-1) Pressure definition 64

(5-2) Area as a function of pressure 85

(5-3) Contact area as a function of waist width, for lumbar airbag 85

(5-4) Contact area as a function of waist width, for axilla airbag 85

(5-5) Contact area as a function of chest width, for thoracic airbag 86

(5-6) Contact area as a function of non-angled airbag, for lumbar at an angle 86

(5-7) Contact area as a function of non-angled airbag, for thoracic at an angle 86

(6-1) Reaction moment as a function of force 105

(6-2) Reaction force as a function of force 105

(6-3) Equivalence between Cobb angle and Ferguson angle 106

(6-4) Matrix equation for solving finite element system 107

List of Abbreviations

2D	Two-dimensional
3D	Three-dimensional
A	Area
ABS	Acrylonitrile butadiene styrene
ACA	Aluminum collar clamp A
ACB	Aluminum collar clamp B
AIS	Adolescent idiopathic scoliosis
AVR	Axial vertebral rotation
BMI	Body mass index
CN	Cervical vertebra N
CAD/CAM	Computer aided design/manufacturing
CBMI	Classified body mass index\
CP	Plastic collar clamp bolster holder
CTLSO	Cervicothoracolumbosacral orthosis
DOF	Degrees of freedom
F	Force
FDM	Fused deposition modeling
FEA	Finite element analysis
GAG	Glycosaminoglycans
GPS	Guidance positioning system
HVP	Heuter-Volkmann Principle
IBC	In-brace correction
ICC	Intraclass correlation
IVD	Intervertebral disc
IVJ	Intervertebral joint
K	Stiffness
LN	Lumbar vertebra N
M	Moment
MAD	Mean absolute difference
MAR	Median absolute residual

P	Pressure
PA	Postero-anterior
PCA	Plastic collar clamp A
PCB	Plastic collar clamp B
PLA	Polylactic acid
R^2	Coefficient of determination
R	Rotations
RMSE	Root mean square error
SCA	Steel collar clamp A
SCB	Steel collar clamp B
SD	Standard deviation
SEM	Standard error of measurement
TN	Thoracic vertebra N
TLL	Thoracolumbar-lumbar
TLSO	Thoracolumbosacral orthosis
U	Displacement
α_L	Stiffness multiplier for lumbar IVJ
α_T	Stiffness multiplier for thoracic IVJ
Δ_{max}	Difference between the sensor value and the correct value
ϕ_z	Rotation of the IVJ around Z

Chapter 1: Introduction

Adolescent idiopathic scoliosis (AIS) is a three-dimensional (3D) spinal disorder which includes a curve in the coronal plane, diminished or exaggerated curvature in the sagittal plane, rotation of vertebrae in the transverse plane, and a rib hump. It has no known cause and affects approximately 3% of adolescents [1]. For many years, the aspects of the deformity other than coronal curvature were largely ignored. However, as the imaging technology becomes more advanced, more recent studies started treating the deformity in 3D. There are primarily two types of conservative treatment for AIS: specific exercise and bracing. Among these two, bracing is the only proven method that can treat AIS effectively [2]. Brace effectiveness is partially affected by compliance, both in terms of wear time and wear tightness, brace construction, in-brace correction, curve characteristics such as size and flexibility, and patient maturity [3]. Flexibility, the amount the curve corrects in a bending test, is an important factor that has not been included much in bracing largely due to radiation from radiographic methods and as-yet poor adoption of ultrasound in the field [4].

Designing a good brace is important because it affects brace effectiveness. However, the process of casting a brace has traditionally been a fairly subjective process. At the time of casting, the internal alignment of spine is not visible, so a follow-up in-brace radiograph is needed to determine whether the brace provides enough correction. If it does not, the brace may need to be adjusted. There have been attempts made to turn this into an objective, quantitative science [5].

As part of the improvements to brace casting that are being attempted, 3D design is increasingly used. Some older braces may not consider 3D aspects of the deformity at all, focusing entirely on coronal curvature. Other braces attempt to perform 3D correction but are ineffective at doing so. Some of the most modern braces incorporate 3D effects into their basic theory, design process, and construction, but this is not widespread [6].

The research done in this thesis attempts to improve the casting process by expanding the ability to incorporate flexibility into casting; improving objectivity and use of quantitative data; and allowing casting to move into fully 3D territory. It reports a mathematical model to incorporate flexibility into brace casting in order to improve objectivity, the production of a frame used to improve 3D methods and objectivity, and a simulation to assist in bracing using the frame objectively.

1.1 Motivation

Spinal flexibility, a measure of how much the spinal curvature can be reduced when performing a bending test, is not routinely used in scoliosis brace treatment because it usually requires the use of radiography, which exposes the patient to harmful ionizing radiation. Also, the flexibility has not been widely reported in brace casting as most studies are done for surgical cases. 3D clinical ultrasound has been developed and used to measure flexibility, but it is not widely available. As a result of these limitations, flexibility measurements are reserved for surgical cases [7]. Fully 3D casting is currently rare in North America, and braces used elsewhere have not been fully proven to be effective The traditional thoracolumbosacral orthosis (TLSO) has been demonstrated to be effective in treatment of AIS [1], so improvement of this type of brace is the focus of this thesis. Currently, patients receiving custom TLSO are cast to reduce the coronal curvature. 3D correction is added later in software (CAD/CAM method) or by modifying the plaster cast (traditional method) after the body shape file is obtained.

During the casting process, if the orthotist can monitor and control 3D aspects, a better brace should result. Additionally, flexibility should be made part of the casting process whether in 2D or 3D.

Simple simulation models have existed for some time, but typically use technology such as surface topography to generate geometry [6], which is not available at all clinics. The 3D frame was expected to be difficult to use owing to the large amount of adjustability, dealing with four pads moving in three dimensions with variable force limits on it. An automated way of determining pad locations could save time and improve results.

1.2 Hypotheses

In this thesis, three assumptions were made:

a. Spinal flexibility can be estimated based on demographic and radiographic parameters.
b. Scoliosis brace casting can be improved by performing the casting step in full 3D, rather than casting in 2D and modifying the model taken from the patient.
c. The final hypothesis was that a treatment of the spine as rigid bodies connected with springs can adequately represent the scoliotic spine, allowing a simulation to be constructed.

1.3 Objectives

The objectives of this study were:

a. Generate a mathematical model that allows estimation of flexibility with data already available to most clinics without requiring extra image. Using five parameters known or thought to affect scoliosis, a mathematical model is to be developed to predict the flexibility.
b. To develop and validate a standing brace casting frame capable of providing forces in three dimensions.
c. To design a software simulation to assist brace casting in the frame by suggesting initial position and pressure values for the pads.

1.4 Outline of Thesis

This thesis consists of seven chapters.

The first chapter contains the introduction, motivation, hypotheses and objectives of this thesis. It also describes the outline of the entire thesis.

The second chapter provides the background of scoliosis, broad information on brace treatment, and finally a review of numerical methods.

A report on six specific braces, including their construction methods, theories of action, 3D spinal correction concepts, and effectiveness was produced in chapter 3.

Flexibility is examined in chapter 4, describing the definition and importance of spinal flexibility. Five commonly used spinal flexibility assessment methods are described. A pilot study to determine the spinal flexibility based on radiographic and clinical data was performed, using linear regression to construct the mathematical model.

Construction and verification of a frame used for casting patients in full 3D is reported in chapter 5. It begins with a literature review on 3D brace casting, followed by details on the design and refinement of a frame allowing 3D brace casting to occur. Verification and testing of the frame follow. A simulation was developed and validated for brace casting predictions in chapter 6, using a lumped rigid body analysis of an AIS spine, built to reduce the complexity of the frame.

The conclusion is found in chapter 7 with future work recommended.

Chapter 2: Background

2.0 Summary

This is the first of the two literature review chapters. It explains the anatomy and anatomic terminology as it applies to adolescent idiopathic scoliosis; the characteristics, statistics and biomechanics of scoliosis and scoliosis bracing; methods of brace construction; and numerical modeling of scoliosis. Section 2.1 begins with terminology used in scoliosis, including anatomical terms consists of planes and directions, and spinal movement and spinal anatomy terminology. Section 2.2 provides an overview of scoliosis, including effects on patients, statistics, measurement and treatment methods, further terminology and biomechanical principles of scoliosis progression. Brace treatment is discussed more in-depth, discussing the three main types of brace (CTLSO, TLSO and night-time) and several construction techniques in section 2.3. Finite element analysis, as it applies to AIS, is discussed in section 2.4. Finally, the chapter is concluded in section 2.5.

2.1 Anatomy of the Spine

Figure 2-1 shows the anatomic planes of a human body. The coronal or frontal plane divides the body into front and back (anterior and posterior), the median sagittal plane is highlighted on the body which is the plane of symmetry for left-right and the transverse or horizontal plane into top and bottom (superior and inferior). These planes can have a translational position anywhere on the body but retain the orientation, with transverse planes often being described at a vertebral level.

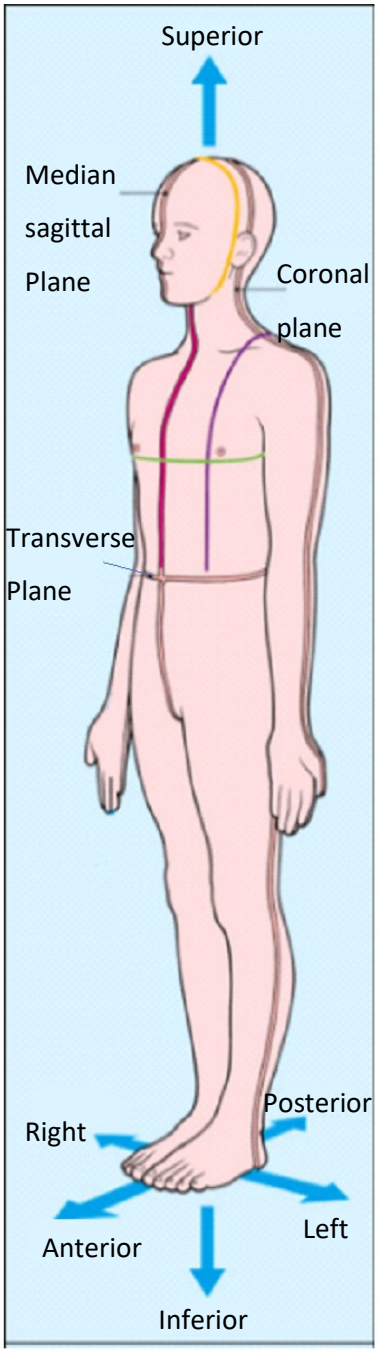

Figure 2-1. Anatomic planes and directions from Human Anatomy [8].

The spine is comprised of five sections, numbered from the top: 1) the cervical spine which consists of seven cervical vertebrae (C1 – C7); 2) the thoracic spine which consists of 12 thoracic vertebrae (T1 - T12); 3) the lumbar spine which consists of five lumbar vertebrae (L1 – L5); 4) the sacrum, which is the fusion of five sacral vertebrae; and 5) the coccyx. Between the vertebrae, intervertebral discs (IVD) are present. Figure 2-2 shows left lateral and posterior views of a healthy spine

with the five regions identified. Ribs are attached to the thoracic vertebrae to provide structure to the thorax and protect the lungs and heart. Spinal lordosis refers to anterior convexity while spinal kyphosis refers to anterior concavity. In healthy individuals, the lumbar and cervical regions are lordotic while the sacrum and thoracic regions are kyphotic. In addition, when viewed in the coronal plane, a normal spine should be straight.

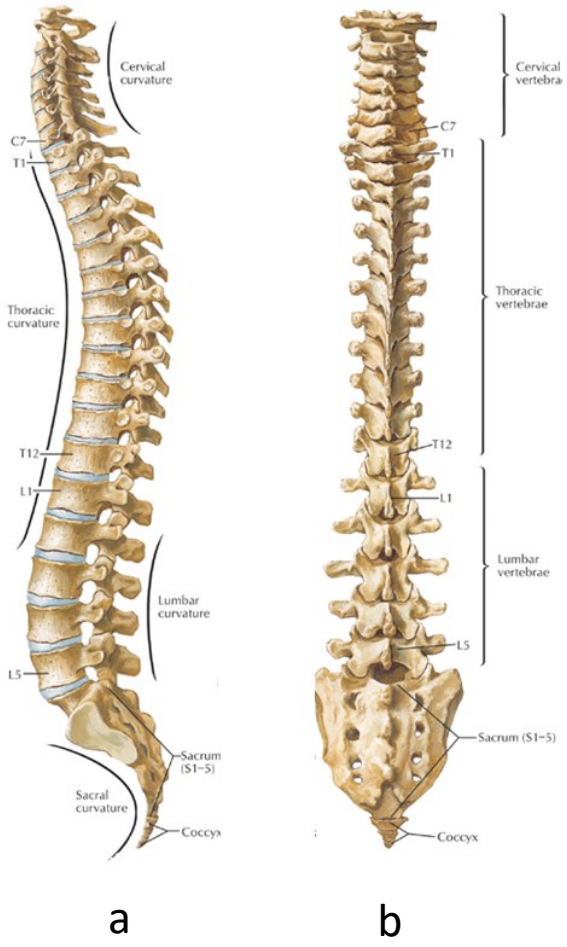

Figure 2-2. a) left lateral view of healthy spine b) posterior view of healthy spine [9].

2.2 Scoliosis Overview

Scoliosis is a spinal disorder characterized by abnormal curvature of the spine. Traditionally, it has been viewed as a two-dimensional (2D) curvature primarily focusing on the coronal plane, but in recent decades, scoliosis has been described more often as a three-dimensional deformity. Besides the coronal and often abnormal sagittal curvature, axial vertebral rotation exists, which may cause a rib hump [10]. The rib hump is a prominence in the rib cage around the apex of the curve that is the

primary cosmetic issue for the disorder [11]. However, the standard diagnostic method remains based on the Cobb angle. The Cobb angle is a measure of how tilted the vertebrae are. It is defined using the vertebral body end plates of the vertebrae terminating the curve. The end points of the curve are determined by identifying the most tilted superior end plate above the apex, and the most tilted inferior end plate below the apex. The Cobb angle is defined as the angle made between lines running parallel to these end plates [12].

10° is the minimum Cobb angle for the diagnosis of scoliosis. Figure 2-3 shows an X-ray image, or radiograph, viewed from behind (described as postero-anterior) of a patient with right thoracic and left thoracolumbar curve, with lines constructed coincident with the most tilted endplates drawn to form two Cobb angles. The thoracic Cobb angle is 44° while the thoracolumbar Cobb angle is 38°.

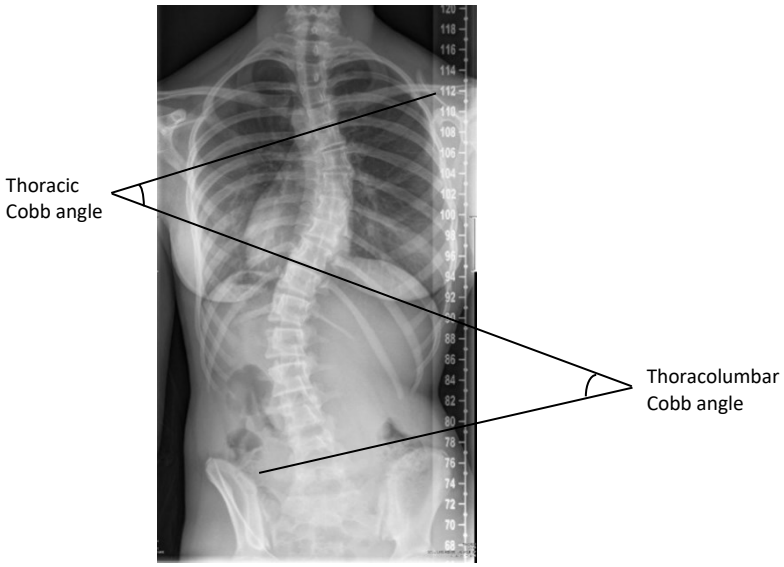

Figure 2-3. A postero-anterior radiograph of a patient with scoliosis and the two measured Cobb angles are 44° and 38° in thoracic and thoracolumbar curves, respectively.

Some forms of scoliosis have a clear cause such as congenital abnormalities of the spine or neurological disorders, such as cerebral palsy, but these are in the minority. Most scoliosis cases, about 80% [13] are idiopathic in nature which means it has no known cause. Idiopathic scoliosis can be divided into three main categories based on the chronological age of the patient at diagnosis: infantile (0-3 years), juvenile (4-9 years), and adolescent (10-18 years) [14]. Infantile and juvenile scoliosis have recently been grouped together and referred to as early onset scoliosis. 80% of idiopathic scoliosis is detected during the adolescent stage [15]. Once it is detected, 90% of cases are stable but approximately 10% of cases progress continually [16]. Progression is defined as an increase of Cobb

angle magnitude by at least 6° between clinic visits, typically at six-month intervals. The progression risk depends primarily on the skeletal maturity of the patient, chronological age and the severity of the curvature [17]. Early onset scoliosis rarely stabilizes, while scoliosis that occurs near the end of growth may not progress [18].

According to a study by Weinstein et al., in 2003 [19] Health and Function of Patients With Untreated Idiopathic Scoliosis, adolescents with scoliosis can live normally with little intrusion. Mental health is typically in the normal range and social functioning such as rate of marriage is not affected. The issues that most patients may have include poor self-image, difficulty with physical and social activities, and back pain. However, if the Cobb angle is large, generally greater than about 80° [16], or if scoliosis is coupled with significant rib fusions that limit growth, health problems such as difficulty breathing and even early death can occur [20].

In term of gender distribution, Rogala et al., [21] reported that at the 10° Cobb angle level, approximately equal numbers of males and females have scoliosis. However, when the Cobb angle reaches 30°, girls outnumber boys by a ratio of 5.4:1.

There are several curve types of AIS depending on the location of the apex of the curve, the vertebra most displaced from the centerline. If the apex of the curve is higher than T11 and below T8, it is thoracic. If the apex is at T8 or above, it is considered an upper thoracic curve. If the apex is between T12 and L1, it is thoracolumbar, and if it is below L1, it is lumbar. There may be more than one curve present in one individual. Thoracic primary curves are the most common at 47%, followed by thoracolumbar or lumbar curves at 43%, double major curves at 8% and double thoracic curves at 3% [1].

The nature of the initiation of AIS is unknown and likely multi-factorial, but the biomechanical theories which cause the progression of curve have been reported in the literature [21]. It has been reported that the intervertebral disc (IVD) wedging may be the start of vertebral body deformation that leads to scoliosis [22]. Once the wedging exists, the uneven loading condition on the vertebral body may cause the curve to increase. IVDs compress differentially under loading, furthering wedging as the deformity progresses [23]. According to the Hueter-Volkmann principle (HVP), bones under compression grow more slowly than bones under tension [24]. As the severity of the deformation progresses, the differential loading increases and thus the rate of deformation increases. This phenomenon is called the Stokes' cycle, or the vicious cycle [25]. As adjacent vertebrae wedge, vertebrae start tilting and a curve then results. Figure 2-4 shows a schematic diagram of the HVP acting on a vertebra.

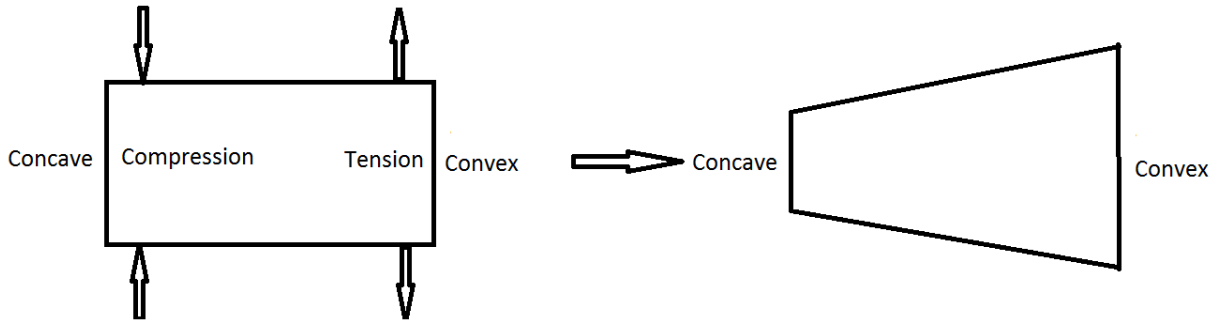

Figure 2-4. Schematic diagram of HVP acting on a single vertebra (not to scale)

Treatments for scoliosis may involve observation, physical therapy including scoliosis intensive rehabilitation, bracing and surgery [26]. Observation is used in cases that are not currently progressive but have the potential to get worse (e.g. small curves on young patients or patients who are near the end of their growth). It involves taking radiographs at every visit (often at six-month intervals) to watch for a change in the condition. Upon evidence of progression occurring, a more active treatment is sought.

Physical therapy instructs the patient to do exercises specific to scoliosis treatment. The objective of physical therapy is to prevent progression of the curve, not to correct it. Exercises with "autocorrection", or the ability to straighten the spine in three dimensions, are the focus of physical therapy. It can be used as an alternative to or in addition to bracing. It has been found to be effective in limiting progression in a systematic review [27].

Bracing is typically used for immature patients with curves between 20°-40°. Braces are devices that provide physical forces on the torso to straighten the spine mechanically. The goal of brace treatment is arresting the progression; correction is possible but rare and not the primary objective. Section 2.3 describes the theory of bracing in more detail and chapter 3 describes the principles of six commonly used braces.

Surgery is a last-ditch effort, typically performed when the Cobb angle is over 45°. It provides correction, in comparison with other methods are meant to merely stop progression. During surgery, screws are inserted into the vertebrae and rods are attached to hold the spine in a corrected position. Bone is crushed and added between vertebrae to allow them to fuse together. It can correct the spinal curvature by up to 70% [28] but has all of the risks associated with major surgery.

2.3 Brace Treatment

The main non-surgical treatment for AIS is bracing. The goal of bracing is to maintain the curve at its existing level during growth spurts. Braces can be either rigid or non-rigid. Rigid braces are by far more common. Among rigid braces, there are cervicothoracolumbosacral orthosis (CTLSO), TLSO and night-time braces.

2.3.1 CTLSO

A CTLSO brace, as shown in Figure 2-5, extends from the neck to the hip and is highly restrictive and undesirable for the patient. It is now mainly used for high thoracic curves with the apex located at the T6 vertebral level or higher. The Milwaukee brace is the main example. Although it is unattractive and uncomfortable to patients, there are no alternatives for upper thoracic curves [29]. Its use has declined in most scoliosis cases after the development of TLSO in the 70s.

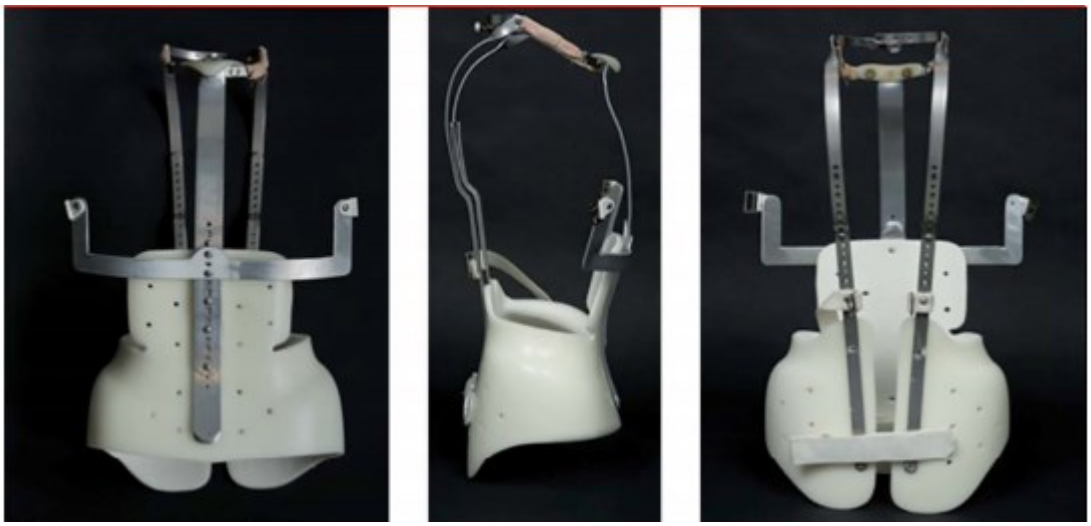

Figure 2-5. Anterior, lateral and posterior views of a Milwaukee (CTLSO) brace [26]

2.3.2 TLSO

A TLSO brace extends from the region between the axilla and the middle of the thoracic region to the hip area. This is the most common type of brace and it is prescribed in most scoliosis clinics. Adolescents can conceal this type of brace under their clothing, which makes it preferable to patients. Also, there are many subtypes of TLSO using different materials, construction methods and principles of operation.

A TLSO is made primarily of thermoplastic as the structural material, with some varieties including metal supports and occasionally using carbon fiber or 3D printed materials [8]. Foam pads are often used to distribute pressure on the body although there is some debate whether this is worth the thermal compromise; shaping the structural material to provide forces may produce cooler braces. They are usually prescribed for wear between 16 (“part-time”) to 23 (“full-time”) hours per day. They enclose the torso between the hips and the armpits and are fastened by straps either on the front or back. Figure 2-6 shows a custom designed anterior-opening full-time TLSO.

The location of the opening is important, according to simulations. Whether it should be posterior or anterior depends on the rest of the brace such as: the pad placements; the curve size; and the location of the curve [6]. There are a few common types of TLSO including the Boston brace [31], the Chêneau brace [32] and the Lyon ARTbrace [33] and their prescriptions are mainly dependent on the clinic locations. Custom designed braces are also used, and they apply some of others’ principles. These braces will be discussed in more detail in Chapter 3.

Figure 2-6. A custom designed anterior-opening full-time TLSO

2.3.3 Night-Time Brace

Night-time braces are worn only at night and the shell may extend further, in both the superior and inferior directions, than a TLSO as mobility is not required. Night-time braces are commonly prescribed when compliance with a TLSO is expected to be poor. Night-time braces are also made primarily of thermoplastic or occasionally carbon fibre. They are prescribed to be worn around 8 hours per night, and they tend to aim for more in-brace correction than TLSO, often as high as 100%. The Charleston bending brace [34] and the Providence brace [35] are the two main types of night-time braces.

2.3.4 Brace Construction

Brace construction varies with brace type and practitioner. Plaster casting is largely outdated, while hybrid plaster computer-aided design and manufacturing (CAD/CAM) and surface topography CAD/CAM methods are commonly used today. In most cases, for any method, the patient is held in a maximally corrected position by the orthotist (brace designer), subject to patient tolerance, while measurements are taken, either by a plaster jacket or a visual scanner.

2.3.4.1 Plaster Casting

The classic method of construction is plaster casting. In this method, a jacket with wet plaster is wrapped around the patient. The patient is then held in the targeted posture by the orthotist or by external bolsters until the plaster hardens. The hardened plaster jacket is then cut off with a cast scissor or saw, and then a positive model is constructed by pouring plaster inside the plaster jacket and allowing it to harden. The positive model is then modified by adding or removing plaster to relieve or increase forces on the patient. A sheet of heated thermoplastic is then draped around the modified plaster positive under vacuum to form the rough brace. Pads and straps are then added to apply forces to the torso. The roughly shaped brace is trimmed to fit the patient's body (e.g. around the axilla and hips to prevent contact) and holes are cut opposite to pads to relieve pressure on the skin. In some bracing theories such as the Chêneau, holes are made to allow active correction [36].

2.3.4.2 Plaster and CAD/CAM Casting

Plaster-based computer-aided design/computer-aided manufacturing is a more recent development. In this method, the negative model is taken from the patient with a plaster jacket, and the jacket is scanned with a surface topography device. These CAD/CAM systems may use one of two systems: raster stereography, which uses a grid of lights on the target and a camera to determine 3D shape; or laser scanning, which uses a laser stripe instead of the grid. A handheld laser scanner is used at the Glenrose Rehabilitation Hospital, Edmonton, Alberta, Canada. It is an Ohio Willow Wood (Mt Sterling, Ohio) brand OMEGA scanner. It offers 18,000 measurements per second with an accuracy of ±0.5 mm and a depth of field of 30 cm. The surface topography system produces a 3D model that is then modified digitally, removing material to areas intended to provide relief to the torso and adding material from areas intended to provide pressure to the patient. A positive physical model based on this digital model is then carved from foam using a carving machine. The brace is cast around this positive model and modified in a similar fashion as plaster casting. CAD/CAM plaster casting methods are easier to use than traditional plaster casting methods while offering similarly effective braces [37] but the equipment tends to add expense.

2.3.4.3 Surface Topography and CAD/CAM Casting

In surface topography, a grid of lasers or lights are projected onto the patient in the corrected shape and the shape of the torso is measured. This may be combined with biplanar radiographs to generate a thorough model of both the interior and surface of the torso. From this, a 3D model is generated in a computer. This 3D model is, similarly to the plaster CAD/CAM method, modified electronically and sent to a carving machine to produce a positive model for casting. This has the same advantages of plaster CAD/CAM but completely removes plaster from the method, resulting in a cleaner, easier process.

2.4 Numerical Modeling of Scoliosis

For numerical modeling of scoliosis, using finite element analysis (FEA) model on braces is frequently used. In deformable body mechanics, partial differential equations are used. However, computers are better equipped to dealing with algebraic equations than partial differential equations. Finite element analysis breaks the system down into small, deformable components called “finite

elements". For this, partial differential equations simplify to algebraic equations with little error due to the small size of the elements. Linear algebra can then be used to solve the system.

FEA is well-suited to situations with complicated geometries, loadings and material properties, which is the case for scoliosis braces {Citation}. The geometry of the problem must be developed first. Typically, in developing a 3D model for a brace, lateral and postero-anterior radiographs are used in conjunction with surface topography scans to develop the geometry. The 3D model is then fed into the FEA software such as ANSYS (Ansys, Inc., Pennsylvania, United States) and the element type can be chosen from one of the three types: one-dimensional (line), two-dimensional (plane) and three-dimensional (solid). The number and size of elements are chosen, and the model is then meshed. Material properties need to be inputted in the form of a stiffness matrix, and then external loadings and constraints are added. The software then solves Equation 2-1:

$$F = K\,U \qquad (2\text{-}1)$$

In this equation, $\mathbf{F}$ is the external force matrix, of a size n x 1, where n is the number of degrees of freedom of the model, $\mathbf{K}$ is the n x n stiffness matrix and $\mathbf{U}$ is the n x 1 displacement matrix

The software solves for the displacement matrix **U** to find displacements of each node and then working backwards, determines stresses (using stiffness properties) and strains (using geometric properties). Interpolation using a shape function, dependent upon the elements chosen, is used to find these values at locations other than nodes. Most FEA methods use forces and displacements only, although the principle extends to moments and rotations as well.

The FEA method has been used for purposes such as improving braces [27, 38] with reasonably good results, in one case claiming an error of 1° compared to clinical results [39]. Incorporating muscle activity seems to be the main challenge facing FEA. The activation pattern is not known and the system involving muscles is statically indeterminate. Muscle activation in FEA is being researched [40], but it has not been used in scoliosis yet. FEA is useful for allowing better analysis of braces than older techniques (such as column buckling theory [41] which relies on assumptions that do not hold in spinal analysis) but tends to be time and computationally intensive. A more detailed review of FEA simulation is given in section 6.1.

2.5 Conclusion

Scoliosis is a 3D spinal deformity, defined mainly by curvature when viewed from behind, primarily affecting adolescents, and particularly young girls more than young boys. It can be treated by

observation, physical therapy, bracing and surgery. Bracing is the most common conservative treatment and is the focus of this thesis. Six common brace types are explored in more detail in following chapters, building on what was described here to develop an understanding of bracing as it currently exists.

Chapter 3: Principles and Construction of Six Commonly Used Braces in the Treatment of Adolescent Idiopathic Scoliosis

3.0 Summary

In this chapter, the brace construction and principles of five commonly used spinal braces in North America and Europe including Boston, Chêneau, Lyon ARTbrace, Providence and Charleston, and a custom designed brace based on the Providence brace approach are described in section 3.1. In section 3.2, the details of the biomechanical theory of bracing in terms of passive effects, active effects, and intervertebral disc effects are reported. Section 3.3 discusses the three-dimensional techniques used in modern scoliosis treatment which should be applied into future designed braces. The final section reports the factors which influence brace success.

3.1 Brace Construction and Principles

Rigid spinal braces have been the principal non-surgical treatment for AIS since the Milwaukee brace was invented in 1946. Modern rigid braces are typically thermoplastic based but some incorporate metal components. They are usually clamshell style, with an opening either on the front or the back and are closed using straps. Pads apply corrective forces are added based on orthotists experienced. The various design decisions depend on the specific brace type, and even within the brace types between practitioners. Figure 3-1 shows the 6 different types of braces that are examined in this chapter.

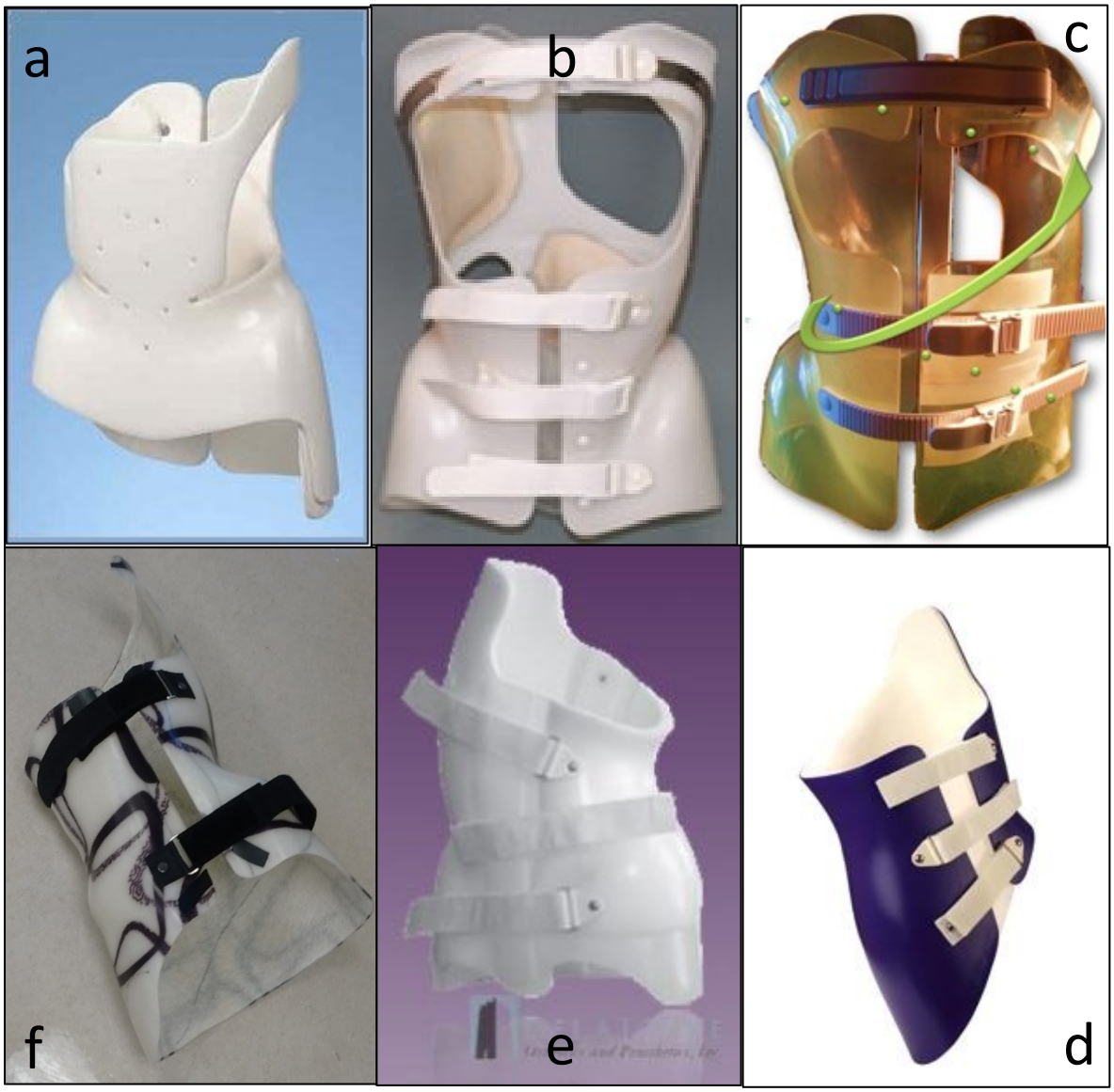

Figure 3-1. (Clockwise from top left) a) Boston brace [42]; b) Chêneau brace [43]; c) Lyon ARTbrace [44]; d) Providence brace [45]; e) Charleston bending brace [46]; and f) Glenrose custom brace

3.1.1 Boston Brace

The Boston brace (Boston Orthotics and Prosthetics, USA) is the most commonly used thoracolumbosacral orthosis in North America [47]. It is a rigid brace designed for full-time wear. It uses three- and four-point bending principles to provide coronal correction, depending on the nature of the curve; double curves call for 4-point systems. It features lumbar and pelvic flexion with a posterior

opening. Its manual [48] describes how the brace is designed and built. The traditional method is the orthotist measuring the size of the patient and ordering a standardized module per the patient's torso shape. The module is symmetric and extends from the iliac crest to the mid-thoracic region. After receiving the module, the orthotist modifies the brace. The orthotist adds pads to concentrate forces at the curve apex and removes material opposite to the major pads, to accommodate the patient's comfort and enhance correction. The company has also started to provide surface topography tools to determine the patient's dimensions in addition to computer-aided design and computer-aided manufacturing methods of manufacturing the brace. Its use has yet to be published. To treat a curve in a high thoracic area (higher than T8), an axilla extension is necessary. A trochanteric extension is placed on the convex side of the lumbar curve, acting as a moment arm for upper forces. Sagittal correction is generally not attempted except with one subtype which induces thoracic kyphosis. Derotation pads are present to reduce rotational deformities. From the literature, users of the Boston brace aim for 50% in-brace correction and is prescribed for 16-23 hours per day [49].

3.1.2 Chêneau Brace

The Chêneau brace is a rigid full-time hypercorrective brace focusing on 3D correction of the curve and is the most commonly recommended brace in Europe [50], initially created in 1979 by Dr. Jacques Chêneau. The Chêneau brace is custom designed by each orthotist depending on practitioner experience. The Chêneau brace is less standardized than other designs, being a collection of principles. Examples of the non-standardization of this method are given in a consensus paper: 52% of practitioners put the thoracic pad at one vertebra above the apex, 48% at the apex, and 0% below; five dorsal rib hump pad shapes are considered and have consensuses between 5-33%; and 56% put high priority on the pad at the ventral rib hump area, 22% medium priority, and 22% low priority [50]. No manual has been published in English but its design principles are elucidated by Kotwicki et al [36]. Like the Boston brace, it uses three- and four-point bending principles to correct curves in the coronal plane. It features a physiologically balanced sagittal profile. Derotation pads are used to manage the rib hump. It uses large open spaces to allow the body to expand during activity into the correct position. It is open at the top to allow what's known as the "cherry stone effect" to occur, whereby the brace pushes on the body to lengthen the spine vertically and to straighten the spine. Active effects, particularly from growth and breathing, are thought to be significant. Growth effects include the bones of the torso readjusting in

response to the brace, while breathing generates pressures against the brace. In-brace correction can reach 100% and it is prescribed for 23 hours per day [51].

3.1.3 Lyon ARTbrace

The Lyon ARTbrace, developed by the same group as the original Lyon brace, is a rigid full-time TLSO using detorsion and elongation principles. The concept of the brace is designed to be adjustable, activity-accommodating, decompressive, stable and transparent. ART stands for Asymmetric, Rigid and Torsion, which is designed using CAD/CAM system. Three 3D scans of the body in different standing positions, a) self-elongation, b) lumbar shift and physiological lumbar lordosis, and c) thoracic shift and physiological thoracic kyphosis, are taken. These scans are combined with each other with OrtenShape software and each scan is used to define features in a different part of the brace. Instead of the usual three- or four-point bending systems for coronal curvature, the brace squeezes the torso to force the spine to elongate and straighten. To correct rotation and the rib hump, the whole torso is twisted counter to the natural rotation. Physiological thoracic kyphosis and lumbar lordosis are incorporated. Active effects from breathing are used, with the pressure from the inhaling torso expansion adding to the pad passive pressure. It is prescribed for 24-hour wear and the average in-brace correction is 70% [33].

3.1.4 Providence Brace

The Providence brace is a rigid hyper-corrective nighttime-only brace, using three-dimensional forces in three- and four-point bending systems to produce coronal correction, developed by Spinal Technology, Inc, USA. As described in the Providence Scoliosis System Manual by d'Amato and McCoy [52], brace construction is done using a stabilizing measuring board and pre-designed braces or casting. The stabilizing board is a board with a mesh of perforations on which the patient lies. Bolsters are placed in several of the perforations and pressed against the patient until they reach the desired position (Figure 3-2), based on the orthotist's judgement. In the lumbar region, the pad is expected to squeeze to displace about 25-50 mm of tissue while in the thoracic region, 20-40 mm of displacement is suggested. Pressure measurements are done using a pressure-sensing film to ensure comfort [53].

Figure 3-2. A volunteer subject on a Providence stabilizing board with bolsters applied

In most cases, measurements are taken from the board and patient. They are then submitted to Spinal Technology, Inc. A brace is constructed based on the measurements and a database of prior brace constructions. In cases that are not suited to mass-produced construction (large curve, large or small patient, abnormal body shape), casting may be used. Wet plaster bandages- are wrapped around the patient first and the patient is then asked to lie on the frame, where the bolsters are re-applied in the previously determined configuration, until the plaster hardens into a cast. The negative cast produced this way is scanned and modified using a CAD/CAM software. Following this, a positive is carved using a computerized milling machine and the final brace is shaped around this positive. Instead of the holes opposite to pads used in the Boston brace, the Providence brace uses empty spaces, or voids, between the brace and the patient to relieve pressure, typically opposite to pads. The use of voids and the consequent continuous shell allows pressure to be maintained more uniformly. Derotation is one of the key features of this type of brace. During the design, the brace is divided into thoracic and lumbar regions and derotation is done separately. For the thoracic region, derotation is produced by rotating the top half of the brace with respect to the bottom half. For the lumbar section, derotation is accomplished by applying a posterior lateral force in the lumbar pad. This system is more objective and repeatable than other braces described in this chapter because the patient is held firmly in place during casting. Quantified skin pressure information theoretically improves compliance by improving comfort. This brace can be used to treat a double curve and the focus is to balance the torso. Furthermore, this brace develops a higher thoracic moment arm by elevating the shoulder compared to a typical underarm TLSO, which is limited by mobility requirements. Similarly, a higher lumbar lateral moment

can be developed because hip mobility is not a requirement as this brace is designed as a nighttime brace. The Providence brace uses a trochanteric extension on the side of the thoracic convexity. According to the construction manual, the maximum in-brace correction achieved for primary curves and compensatory curves can be up to 96% and 98%, respectively [35]. However, as this Cobb angle reduction is comparing standing position to the supine in-brace Cobb angle, this is not directly comparable to values given for full-time braces. As it is a nighttime brace, it is prescribed for 8 to 10 hours per night.

3.1.5 Charleston Brace

The Charleston brace is an aggressive, nighttime, rigid hypercorrective brace that works by bending the entire torso laterally opposite to the curve [46]. Like the Providence brace, hypercorrection can be accomplished by applying a longer moment arm as low as the pelvis instead of the iliac crest. Bending is allowed due to not requiring the head to be centred above the pelvis. This brace aims to treat a single curve. In addition, this brace does not attempt to derotate the spine [54]. The immediate in-brace correction can be up to 97% for the primary curve [54] but in practice the brace design may be less aggressive due to comfort concerns; like the Providence, this is a comparison between standing Cobb and supine in-brace. The main advantage of this brace is that compliance may be better than for full-time braces because it is only worn at night for 8 hours. Some drawbacks include the fact that it may exacerbate or even initiate compensatory curves [54] and comfort may be problematic.

3.1.6 Glenrose Custom Brace

The custom brace used at the Glenrose Rehabilitation Hospital, Edmonton, Canada, is a rigid full-time brace mainly using the Providence bracing principles. It primarily uses three- and four-point bending systems to induce coronal correction. Voids are placed to provide relief opposite forces. It is asymmetric in the coronal plane with a sagittal design partway between physiological standing and flat back. It is opened in the front and 2 to 3 straps are used to secure the brace while the brace is worn. The transverse positions of the thoracic and lumbar pads are decided upon to oppose the curve's rotation. The casting method is very similar to the Providence system with a stabilizing board and bolsters used to hold the patient in position with the curve reduced. A similar CAD/CAM method to the Providence is used. The target in-brace correction is 50%.

3.2 Biomechanics of Bracing

These braces all use the Hueter-Volkmann principle. The goal of brace treatments is to bring the spine to a more physiologically balanced shape such that the previously compressed bone growth plates on the concave side are unloaded or even in tension and vice versa for the other side [24]. Three main mechanisms can be used to explain this action: a) passive forces - the interface pressures between a brace and the body which force the spine into the desired shape; b) active forces - patients pull away from the high-pressure points to pull the spine into the desired shape; and c) IVD swelling - correctly-shaped IVD applies force more equally to the vertebra when they swell in daily cycles. Different braces have different theories to treat the deformity.

3.2.1 Passive Mechanisms

In term of the passive force used in the brace treatment, the simplest method of correcting the coronal curvature is to apply lateral pad forces to the spine, transmitted either through ribs in the thoracic region or soft tissue in the lumbar region. Passive brace forces have been unambiguously shown, using finite element analysis, to influence the correction [55, 56]. For a single curve, a three-point pressure system is applied Figure 3-3, pushing the convex side of the curve towards the centre by having forces applied towards the apex with counter forces. For a double curve, a four-point pressure system is used Figure 3-4 with forces on both apices and counter forces above and below. As the two main curves tend to be opposite, each provides a counterforce for the other apex. The force magnitudes applied to the body are largely limited by the skin tolerance. According to a Reuler et al. study, skin pressure tolerance may be as low as 70 mmHg for exposure on the order of several hours [53] so longer moment arms allow higher moments to act on the spine itself. All braces use a hip force and in many cases an axilla force. When the hip force is applied, it is always on the same side as the thoracic force. Similarly, when the axilla force is used, it is always on the same side as the lumbar force. In addition, the Boston brace uses a supero-lateral force on the ribs for the thoracic pad and a lateral force for the lumbar region. The Providence brace uses a lateral force in the thoracic region and a postero-lateral force on the lumbar region. The Chêneau brace pushes on the convexity of the curve, although it is not standardized as to where and in what direction it pushes, except in some way opposite to it. The Glenrose custom brace uses a posterior pad in the thoracic region and an anterior pad in the lumbar region. The Charleston and ARTbrace do not use pads in the traditional sense. Gravity acts on the body in a distributed manner, adding a significant vertical load to the hypothetical three- and four-point

pressure systems shown in Figures 3-3 and 3-4. It is likely that higher brace forces lead to better results; however, skin break-down may occur if high loads are applied for a long period. Therefore, maximizing applied forces within the constraints of skin tolerance is a requirement for an optimum brace.

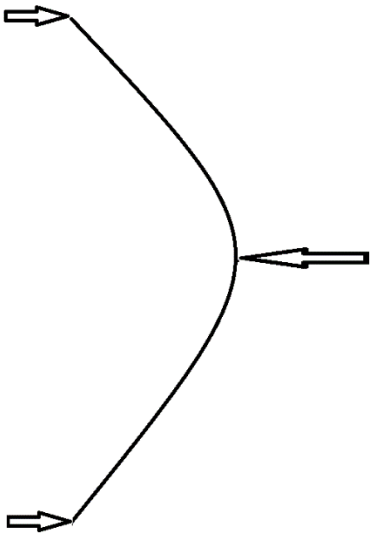

Figure 3-3. Three-point bending system (simplified 2D)

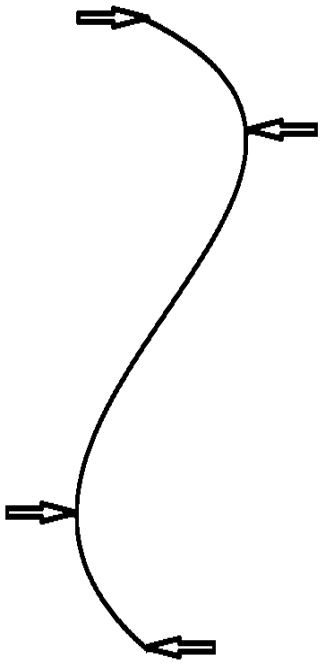

Figure 3-4. Four-point bending system (simplified 2D)

In addition to horizontal forces, other mechanisms exist. Elongation is used by the Chêneau, the Lyon ARTbrace and, to a smaller extent, the Glenrose custom brace, to correct coronal curvature, with the brace squeezing the body and forcing the tissue of the trunk to move upwards to maintain its volume, thereby straightening the spine.

Another method of correcting coronal curvature is the use of sagittal forces. Among the six types of brace described in this chapter, only the Boston brace uses lumbar sagittal forces to correct coronal curvature. These lumbar forces are not designed to correct the sagittal curvature, per the bracing manual. It is angled to produce a 15° lordosis on the lumbar region of the spine. According to Van Loon et al and Clin et al studies [6, 57], no consistent results verified that lumbar flexion could improve coronal deformity in double major curves cases.

3.2.2 Active Forces

In addition to passive forces, active muscle forces may play a significant role in correcting the curvature. The Boston brace and the Chêneau brace [48, 58]claim that active action is important in the brace treatment; however, the actual effects have not been fully documented and proven to have an effect. The earliest study on investigation of active forces was conducted in 1988 by Wynarsky and Schultz [58], which used electromyography to look for muscle activation in braces. However, only a small number of muscles were monitored, and the authors did not find any additional muscle activation during brace wear. A later study in 2003 by Odermatt et al [59], analyzing a larger group of back muscles, showed increased muscular activation while wearing a brace and concluded that active effects may have an impact. They examined more muscles than the Wynarsky and Schultz study and found that the activity tended to be in the lateral muscles instead of the expected medial muscles. The actual resulting force was not reported in that study. Another study, in 1991 again by Wynarsky and Schultz [60], used an FEA simulation to model the effects of active forces in conjunction with passive forces and suggested that active forces affected correction. One limitation of that study was that muscle activation patterns in spinal support muscles were not known.

FEA studies using only passive forces tend to have a discrepancy between simulated correction and the actual correction. For example, an FEA model study in 2003 by Périé et al., by demonstrating that passive forces were not enough to produce clinical results, suggested that there were factors other than passive brace forces providing correction in a brace [56]. A further passive FEA study by Clin et al. in 2011 [55] incorporating the effect of gravity on the torso showed a predicted range of corrections

averaging around 25% worse than actual corrections. All these studies suggest there may have other loading factors influencing brace treatment.

3.2.3 IVD Swelling

The IVD in scoliosis is wedge shaped and has the nucleus pulposus of the disc translated convexly, which applies loads that exacerbate the curvature [22]. The IVD contains glycosaminoglycans (GAG) which imbibe water, primarily at night when the load from standing is removed. These are primarily found in the nucleus pulposus, held within a collagen matrix. In AIS, there is more collagen in the apical and adjacent IVDs, theoretically leading to more swelling and consequently, higher forces on the adjacent vertebrae [22]. The normal pressure applied by the Charleston brace is at most 1 MPa at the apex of the curve [35]. In comparison, the IVD can produce pressures up to 0.2 MPa in a healthy individual [61]. Due to the increased GAG at the apex, it may be even higher in scoliosis. As a result, the loads from the IVD's swelling may not be able to be ignored. Braces change the shape of the IVD closer to the normal flat shape [22] so the swelling pressure partially evens out the forces on the vertebra, reducing progression based on the Hueter-Volkmann principle.

3.3 Current 3D Concepts of Bracing

The above methods primarily address the coronal curvature of the spine, but several deformation aspects are found in scoliosis: sagittal deformity (hyperkyphosis or hypokyphosis), axial vertebral rotation (AVR), a rib hump and coronal curvature. While traditionally coronal curvature was the primary concern, 3D bracing corrects the other aspects of the deformity. Not all braces attempt to correct the curve in all three dimensions. The Boston brace, the Providence brace and the Charleston brace are generally not focused on sagittal curvature correction and may create hypokyphosis on patients [47, 52, 58]. However, the Boston, Providence and Glenrose custom braces still attempt to correct AVR while the Charleston brace does not. Among the six braces described in this chapter, only the Chêneau [51] and Lyon ARTbraces [33] offer full 3D correction.

3D bracing has historically been somewhat limited due to the imaging and analysis tools available. For many years, two-dimensional radiography was the primary tool with which to analyze scoliosis. From this view, sagittal deformities are not visible and AVR is not measured in a straightforward manner. CT scans can measure the full 3D deformity but they are undesirable due to radiation exposure concerns and may still not be perfectly accurate [62].

Cobb proposed a method to measure AVR based on the spinous process [12] but due to vertebral deformation, the spinous process translates on the radiograph both from deformational and rotational processes. The pedicles were then pursued because they tend to deform less and so their translation on the radiograph is closer to pure rotation. It was not until 1986 that the Stokes method came into being [62]. With this method, it became possible to estimate AVR using a PA radiograph. Figure 3-5 shows the vertebra labeled as required to calculate the angle using the Stokes method. To calculate the rotational angle, Equation 3.1 is used:

$$\theta = \left(\left(\frac{a-b}{a+b}\right) \times \frac{w}{2d}\right) \quad (3\text{-}1)$$

Measurements *a* and *b*, the projected distances between the pedicles and the vertebral body centroid from the coronal view, are taken from the radiograph and then a table (found in Stokes et al., 1986 [62]) is used to determine the ratio *w/d*, where *w* is the distance between pedicles, perpendicular to the axis of the pedicles, and *d* is the distance between the pedicles and the vertebral body centroid in the transverse plane. *w/d* is specific to each vertebra level but consistent between patients.

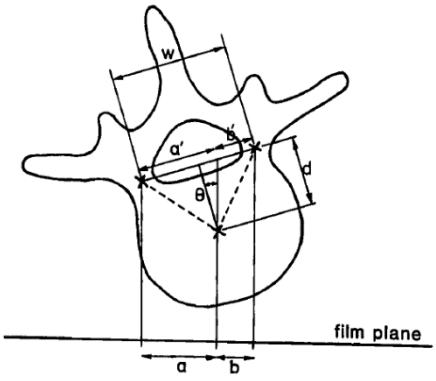

Figure 3-5. Measurements required for Stokes method

In addition to the Stokes' method, ultrasound has been used to measure AVR. In 1989, Suzuki et al. [63] used ultrasound to measure AVR in scoliosis patients using an ultrasound transducer with an attached inclinometer. To measure rotation, the ultrasound transducer would be rotated until the transducer was perpendicular to the spinous process and the inclinometer reading would be measured. More recently, 3D ultrasound has been used [64]. In this method the ultrasound transducer is held perpendicular to the surface of the back. The scan begins at T1 and the transducer traces the spine down to L5. Coronal, sagittal and transverse views are generated. On the coronal ultrasound image, the centres of the laminae or transverse processes are identified manually. The 3D location of these points is determined by software and the rotation of the vertebrae is determined.

Biplanar radiographs can be used to produce a 3D model of the spine, including transverse plane deformity. The EOS low dose biplanar radiograph system (EOS Imaging, Paris, France), first mentioned in scoliosis research in 2003 [65], is a means of getting more information than is available on AP radiographs [66]. It produces only about 11-33% of the ionizing radiation exposure as with a conventional radiograph and produces accurate measurements of scoliosis in all three dimensions [67].

For acquiring sagittal information, the most straightforward means is simply taking a lateral radiograph. 3D ultrasound can also determine the sagittal shape of the spine accurately [64].

The rib hump is hard to study because as yet there has been no means of quantifying the deformity. Some braces attempt to qualitatively reduce it while others seem to overlook it altogether.

3.4 Factors Affecting Brace Effectiveness

Contrary to the importance of 3D brace effects above, brace effectiveness is usually defined in terms of the coronal Cobb angle or necessity of surgery. The Scoliosis Research Society suggests that studies on scoliosis bracing measure as outcomes 1) percentage of curves that have progressed less than 6 degrees and 2) percentage of curves with a final Cobb angle greater than 45 degrees, or the patient needing surgery or having it recommended [68]. These guidelines do not yet include three-dimensional deformity as a primary outcome measure of bracing, although they do suggest reporting it where available.

From literature, a variety of factors have been reported affecting or related to brace treatment outcomes: [36, 37, 39] Factors intrinsic to the spinal disorder include curve and patient characteristics such as:

1. Cobb angle
2. Axial vertebral rotation
3. Curve location
4. Spinal flexibility
5. Gender
6. Patient skeletal maturity

Factors that can be controlled by the patient or orthotist include:

1. Compliance
2. Brace wear quality
3. Brace design

4. In-brace correction

3.4.1 Curve Severity

Curves with larger Cobb angles [69] and curves with larger AVR [69] tend to have a higher bracing failure rate. This ties into the vicious cycle theory of scoliosis progression wherein progression leads to further progression due to increasingly asymmetric forces. While braces attempt to balance the spine to prevent the vicious cycle by reducing asymmetric forces, full time braces do not have 100% correction and nighttime braces are only worn for 8 hours per day, so complete reduction of asymmetric growth is not feasible.

3.4.2 Curve Location

For many braces, high thoracic curves are problematic for bracing success; in many of these cases, the Milwaukee brace is called for. The Boston brace, for instance, has trouble managing curves with an apex above T8, with optimal in-brace correction at T10 and below [70]. The Providence brace, likewise, has a better success rate for lower curves, with a success rate of 94% for lumbar curves; 93% for thoracolumbar curves; and 63% of thoracic curves [35]. The likely reason for this effect is that most braces have as their upper limit the axilla and so the allowable moments on higher thoracic curves are smaller than that for lower thoracic or lumbar curves.

3.4.3 Spinal Flexibility

Spinal flexibility is a measure of how much the spine can be reduced in size with the application of forces. Spinal flexibility may also have an impact on brace outcomes as more flexible spines yield better in-brace correction [71]. Most flexibility measurements are primarily reserved for surgery, as they are done using radiographs which are undesirable due to radiation exposure concerns, which is viewed as an unacceptable risk for bracing patients. Flexibility measurements are discussed in Chapter 4. With the advent of ultrasound Cobb angle measurements, it may now be possible to routinely do flexibility testing on brace patients.

3.4.4 Gender

Gender has an impact on brace outcomes. Males tend to have worse results with bracing than females. The main reason may due to worse compliance [72], which results from a “greater psychological burden” for boys [73]. In-brace correction also has an impact, which is lower in boys possibly due to a less flexible spine [72].

3.4.5 Skeletal Maturity

Skeletal maturity refers to how close to growth completion the patient is. It is often defined using the Risser sign, a measure of how calcified the iliac apophysis is. It ranges between 0, no calcification, and 5, complete calcification of the apophysis [74]. This is visible on a radiograph as progression of a white front from the lateral to the medial side of the hip as shown in Figure 3-6. Another measure is growth velocity with maturity being defined as less than 1 cm of growth in a six-month period [75]. Menarche also indicates skeletal maturity in girls by indicating the start of puberty [76]. Finally, chronological age can be used, although because adolescents mature at different rates, this may be less accurate than the other methods used by Little et al., [75]. Skeletal maturity has an impact on bracing as less mature patients tend to progress more but are easier to treat.

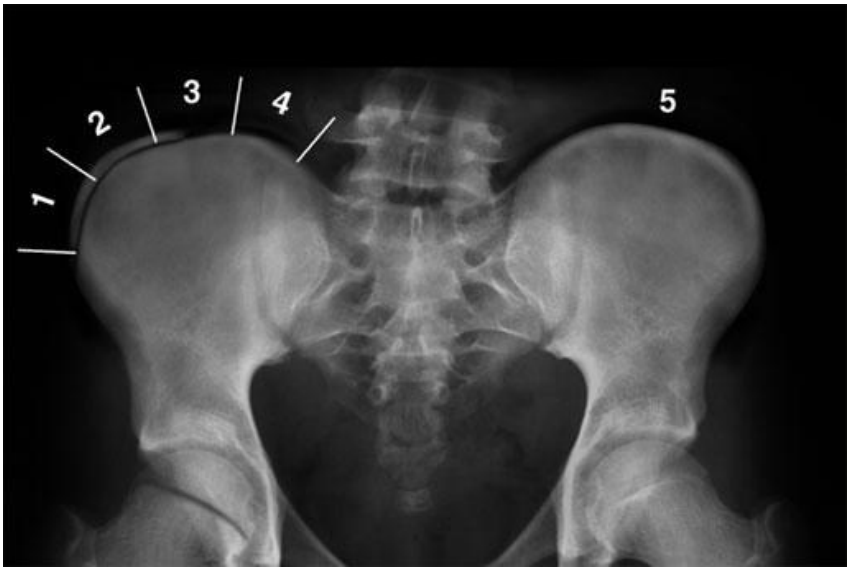

Figure 3-6. Illustration of Risser sign [75]

3.4.6 Adherence

Adherence is defined as how much time the brace has been worn. It is often described as either as a percentage of wear time relative to the daily prescribed time, or the number of hours per day that the brace is worn. HVP theory suggests that increased compliance should yield better results as the spine is held in a corrected position during more of a day's growth, and this is supported by research showing that improved compliance leads to improved results [77]. Weinstein et al. showed that, for daytime TLSO, increased brace wear yields better treatment results [2]. Figure 3-7 shows a plot of brace treatment success versus wear time per day, showing an increase in success as the hours of wear increase. Success exceeds 90% with just 12.9 hours of wear time per day. For a long time, patient questionnaires were used to determine compliance but this was found to be excessively optimistic, so objective brace wear monitors were developed that use either force, temperature or both, to determine if the patient is wearing the brace, and how tightly [42]. Compliance was found in one study to be 75% compared to reported compliance of 85% [78]. One study found that brace wear time for a TLSO is about the same for a 16 and 23 hour per day prescription [79]. Compliance in night-time braces has not been evaluated with objective monitors but is thought to be a higher percentage than for full-time wear. Efforts are being made to improve compliance. One method to improve compliance with treatment is simply educating the patient [80]. Compliance monitoring, with the patients being made aware that they are being monitored, has a strong effect on compliance, increasing wear time by 3.2 hours per day [80]. A questionnaire was developed to try to predict compliance before bracing even begins to allow pre-emptive strategies for improving compliance. The results of the questionnaire were found to correlate to compliance [81]. Brace materials and designs are being changed to try to improve compliance especially by improving comfort. Heat and moisture are thought to be the areas with the most improvement available [82].

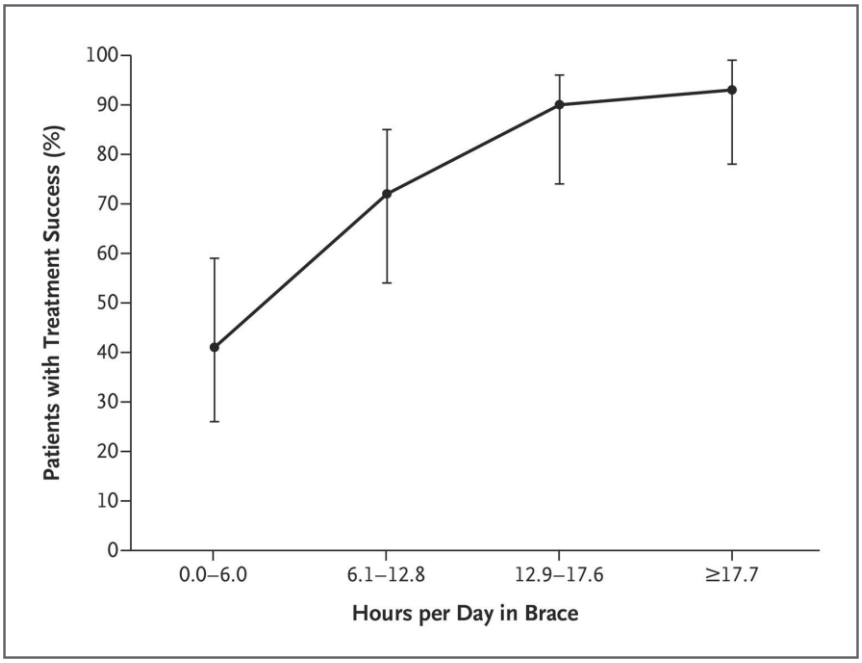

Figure 3-7. Brace treatment success rate versus wear time per day, taken from Weinstein et al., 2013 [2]

3.4.7 Brace Wear Quality

Brace wear can also be described in terms of quality, the amount of time spent wearing the brace at the prescribed tightness. If the brace is not being worn at the correct tightness, its efficacy may be less. Force-based compliance monitors can measure this. However, with growth and adaptation to the brace, in addition to positional effects, in-brace forces may change even with the same strap tension and adjustments are therefore required [83]. Quality of wear may correlate to bracing success by improving in-brace correction [3].

3.4.8 In-Brace Correction

In-brace correction (IBC) is another factor which correlates with treatment outcomes. Improved in-brace correction leads to improved bracing outcomes [70]. IBC is a measure of how much the coronal aspect of the deformity is reduced by a brace. This depends on the brace type and construction quality as well as the patient's characteristics. Different values are sought for different brace philosophies. For example, the Boston brace tends to achieve about 50% in-brace correction [70], the ARTbrace around 70% [33], and the Providence brace can reach nearly 100% [35].

3.5 Conclusion

Correction of scoliosis requires the vertebrae and IVD to adopt a more physiologically normal shape, which reverses or slows the Stokes' cycle per the Hueter-Volkmann principle. Active correction is often invoked but only three studies have been done on it specifically, none of them conclusive. Evening out IVD swelling, which in an untreated scoliosis patient is highly asymmetric, may be a reason that braces are effective. Most modern braces are of the rigid variety, and most use pads to apply corrective forces to the body. Three-dimensional correction is essential. Among the braces reported on in this thesis, only the Chêneau brace and the Lyon ARTbrace address all three-dimensional correction directly; the Boston, Providence and Glenrose custom braces only affect the rib hump incidentally in their AVR correction, and the Charleston does not address it at all. There is often a shortage of evidence related to brace designs with some brace features being contrary to the literature. As more evidence is produced, braces should be changed to match the best practices of the time. The following chapter does a quantitative analysis of flexibility, one of the factors affecting bracing efficacy.

Chapter 4: Development of a Linear Regression Model to Estimate Spinal Flexibility for Brace Candidates with Adolescent Idiopathic Scoliosis

4.0 Summary

As discussed in chapter 3, spinal flexibility is one factor that affects brace effectiveness. This chapter reports a pilot study to develop a model to predict spinal flexibility in brace candidates with AIS. The methodology included using measurements from standard postero-anterior (PA) radiographs, patients' demographical information and ultrasound measurements from maximum prone side-bending to develop the model. A single linear regression method was applied to generate the model and leave-one-out cross-validation was used to validate the model.

4.1 Importance of Flexibility of the Scoliotic Spine

Spinal flexibility is the reduction of the scoliosis curve in a flexibility test where forces or body movement are used to reduce the magnitude of the curve. Side-bending is the most common test and involves the patient bending towards the curve direction and then the Cobb angle is measured. Understanding the flexibility of the spine for scoliotic patients is important for both surgical and brace treatments planning. It can be calculated using Equation 4-1.

$$Spinal\ Flexibility\ = \frac{Standing\ Cobb\ Angle\ –The\ corrected\ Cobb\ angle\ at\ the\ flexibility\ test}{Standing\ Cobb\ Angle} \times 100\% \quad (4\text{-}1)$$

For surgical planning, orthopaedic surgeons use flexibility information to estimate the amount of curvature correction in spinal fusion as well as determine whether a curve is structural or functional. Structural curves are permanent and may require surgical correction, while functional curves can be corrected with position and do not warrant surgery [4]. Brace patients who have stiff spines, with a flexibility of less than 20% do not benefit from bracing [84]. Also, there is a strong positive correlation between flexibility and in-brace correction which affects brace treatment outcomes [71]. To estimate the spinal flexibility, there are many methods which can be used, described in detail in section 4.1.1.

4.1.1 Review of Different Methods to Measure Flexibility

There are several radiographic methods which can estimate spinal flexibility, five of which are reported here. The five methods are a) supine side bending, b) fulcrum bending, c) push-prone, d) traction, and e) suspension. Typically, flexibility tests are done for surgical cases as the exposure to radiation is considered unacceptable for bracing patients. Using Equation 4-1, 0% indicates that the curve is rigid, and the spinal curve cannot be reduced by the patient's motion, self-weight or tolerable external forces, depending on the test. A value of 100% indicates the spine can completely correct which brings the corrected Cobb angle to 0^{o}. Overcorrection, which means the flexibility exceeds 100%, is possible but rare.

Among the five methods, the most common technique is the supine side-bending test [4]. For this test, patients are instructed to lie on a bed in supine position and then asked to bend as much as possible in the direction toward the convex side of the curve while keeping the pelvis and shoulders flat to the bed [85]. A radiograph of the spine is taken at this posture. This method is convenient as it requires no special equipment. However, the bending correction depends on the patient's effort and it is difficult to quantify the bending moment.

The fulcrum bending test is another method wherein the patient is laying over a plastic cylinder. The plastic cylinder is positioned under the apex of a lumbar curve or under the rib corresponding to the apical vertebra [85]. Figure 4-1 shows a patient undergoing a fulcrum bending test for a right thoracic curve. There are three standardized sizes of cylinders with diameters of 19 cm, 23 cm or 27 cm. The size of the cylinder is chosen depending on the curve type: if the curve is lumbar, the cylinder is chosen to keep the pelvis off the bed; if the curve is thoracic, the shoulder is to be off the bed. Once the patient is in position, a radiograph is taken.

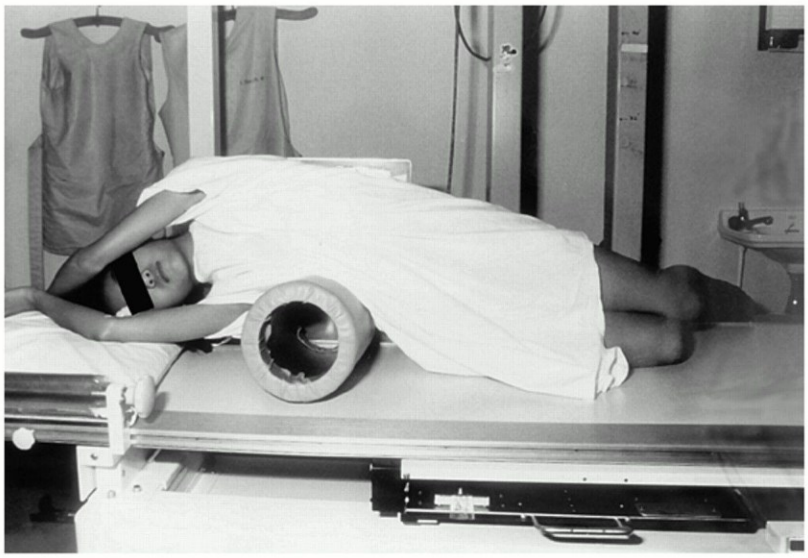

Figure 4-1. Patient undergoing fulcrum bending test for a right thoracic curve [85]

The third method is the push-prone bending method, which requires the patient to be in a prone position and a physician subjectively applies lateral forces to the patient to reduce the spinal curvature (Figure 4-2). In the corrected position, a radiograph is taken. In early versions, the physician would hold the patient in the corrected position while the radiograph is taken. Due to concerns about radiation safety, bolsters have been introduced to hold the patient in order to reduce radiation exposure for the physician [86].

Figure 4-2. A push-prone bending test is performed with a physician applying lateral forces to the patient [87]

The fourth described method is traction which involves applying an axial tension between the neck and the lower body with the patient in a supine position [88]. Forces of up to 180 N are used, dependent on patient tolerance [89]. While under this force, a radiograph is taken. It is usually done under general anaesthesia depending on surgeon preference; however, this does not result in statistically significant differences [90].

The suspension method is a more recent approach, which was first published in 2009 [91]. In this, the patient is suspended vertically in a frame with a harness around the axillae (Figure 4-3), allowing their body weight to straighten their curve. A radiograph is then taken.

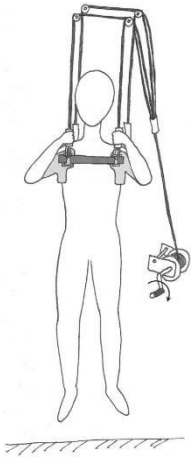

Figure 4-3. Suspension flexibility test [91]

The relative accuracies of each flexibility test in predicting surgical correction depends on the curve. For curves >60°, traction appears to be the best option [92]. For curves smaller than 60°, fulcrum bending is superior to side-bending for main thoracic curves. For upper thoracic curves, side-bending is superior to fulcrum bending. For thoracolumbar-lumbar curves, they are similarly accurate. Push-prone consistently yields worse results than other methods [2, 14, 15]. Table 4-1 summarizes these results.

Table 4-1: Most effective flexibility test by curve location and magnitude

Curve Magnitude (°)	Curve Location	Best test
>60	Any	Traction
<60	Main Thoracic	Fulcrum
<60	Upper Thoracic	Side-Bending
<60	Thoracolumbar-Lumbar	Side-Bending = Fulcrum

Little data is available for suspension's accuracy as of yet. As flexibility measurements are rarely used for bracing, there has been no evaluation of the various types of flexibility tests for this purpose. However, researchers have started looking for non-ionizing imaging methods to estimate flexibility; ultrasonography has been proposed for this purpose. Ultrasound imaging is a radiation-free method of measuring spinal characteristics such as Cobb angle. Basically, an ultrasound transducer is moved down the spine to determine the position of vertebral landmarks based on wave reflections. It was originally introduced in 1989 by Suzuki et al. for measuring AVR [63] but is still not common. Ultrasound requires specialized equipment that is not standard at scoliosis clinics, as well as a degree of training. In addition, Cobb angle was unable to be measured directly from ultrasound images. Previously, relationships were attempted to be formed between AVR [63] or spinous process angle [93] and Cobb angle by measuring AVR and spinous process angles with ultrasonography and comparing them to radiographic Cobb angles. Starting in 2012, Chen et al. [94] introduced the centre-of-lamina method to measure the proxy Cobb angle from the ultrasound image. The lamina is a landmark on each side of the posterior of a vertebra, which shows up clearly as a bright spot on the ultrasound method due to its strong reflection characteristics. To perform the actual measurement, the upper and lower most-tilted vertebra are first identified. This is done by drawing lines between each pair of lamina centres on each vertebra, demonstrated in Figure 4-4.

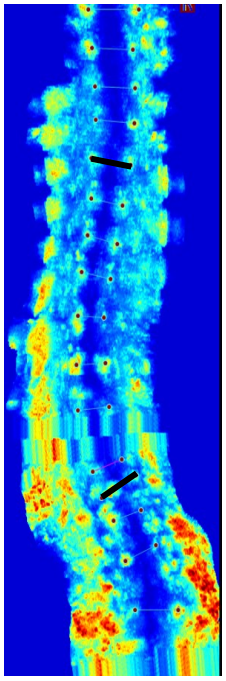

Figure 4-4. The proxy Cobb angle measure on ultrasound image using centre-of-lamina method.

Like the Cobb method on PA radiograph, the superior and the inferior most-tilted vertebrae within the curve are identified and the angle between the slopes of these two vertebrae defines the proxy Cobb angle. It has been found to be accurate and reliable for Cobb angle determination with an error of 2.7±1.9° compared to a radiograph [17] and with a mean absolute difference (MAD) less than 2.1° compared with MRI [95]. For AVR it has also been shown to be accurate with a MAD of 0.3°-0.9° [94]. The centre-of-lamina technique for determining Cobb angle from ultrasound also offers a MAD, compared to radiographic Cobb angle, of 4.8° [96]. Ultrasound has been used to measure spinal flexibility for surgical cases in a limited study, showing comparable results to radiography [7]. Because radiography is undesirable, and ultrasound is not universally available, a method for predicting flexibility without using a bending radiograph or ultrasonography is proposed. In order to allow all clinics to use flexibility, single linear regression analysis was applied to find a mathematical relationship between information taken from a standing postero-anterior radiograph and clinical records and the spine's flexibility.

4.2 A Pilot Study to develop a model to predict Spinal Flexibility

4.2.1 Patient Selection

Fourteen females who were diagnosed with adolescent idiopathic scoliosis and prescribed braces, were recruited from the local scoliosis clinic. Ethics approval was granted by the local ethics board and all patients signed the consent forms before being enrolled into the study. Both major and minor curves were included for analysis. The average age was 13.3±1.7 years old and the average major Cobb angle was 32.3±7.5°. A total of 24 curves were identified, including: eleven thoracic (all right; six minor, three major, two double major), nine thoracolumbar (eight left, one right; seven major, two double major) and four lumbar curves (all left; one minor, one major, two double major). Table 4.2 contains the curve information; thoracolumbar-lumbar is the combination of thoracolumbar and lumbar.

Table 4-2: Curve summary of the 14 participants

Type	Total	Major	Minor	Double	Right	Left
Thoracic	11	3	6	2	11	0
Thoracolumbar	9	7	0	2	1	8
Lumbar	4	1	1	2	0	4

4.2.2 Method of Determining Curve Flexibility

A prone side-bending flexibility test was used and investigated using ultrasound. The flexibility of a curve was defined using Equation 4-1 [97]. To acquire the side-bending information, the patient was asked to lie in a prone position and told to bend towards the convex side of the curve as far as possible while keeping the pelvis fixed in place. The ultrasound scan began at the C7 vertebra and terminated at the L5 vertebra, following the curve of the spine. C7 is identified by having the patient bend his or her neck forward until the C7 spinous process becomes apparent. L5 is determined by counting vertebrae from C7. To determine the location of the vertebrae, the spinal process was palpated by the operator. This was performed twice when the patient has a double curve, once in left bending and once in right bending. The vertebrae belonging to the curve were determined using the Cobb method on the standing PA radiograph; the most tilted upper and lower vertebrae around the apex were used to determine the bounds. These same vertebrae are identified on the side-bending ultrasound image and the angle found

on the bending ultrasound image was measured using the centre-of-lamina method. Figure 4-5(a) shows the PA radiograph of a patient with a double curve, right thoracic (T5-T10) and left lumbar (T10-L4). The thoracic Cobb angle is 32° while the lumbar Cobb angle is 33°. In Figure 4-5(b), it shows a maximum left prone side-bending ultrasound image with an angle of 14° on the same lumbar curve. The spinal flexibility for the lumbar curve is calculated to be 58% using Equation 4-1. The PA radiograph was taken on the day that the brace was prescribed while the side-bending ultrasound was taken during the brace casting clinic which was usually within two weeks of the brace prescription date.

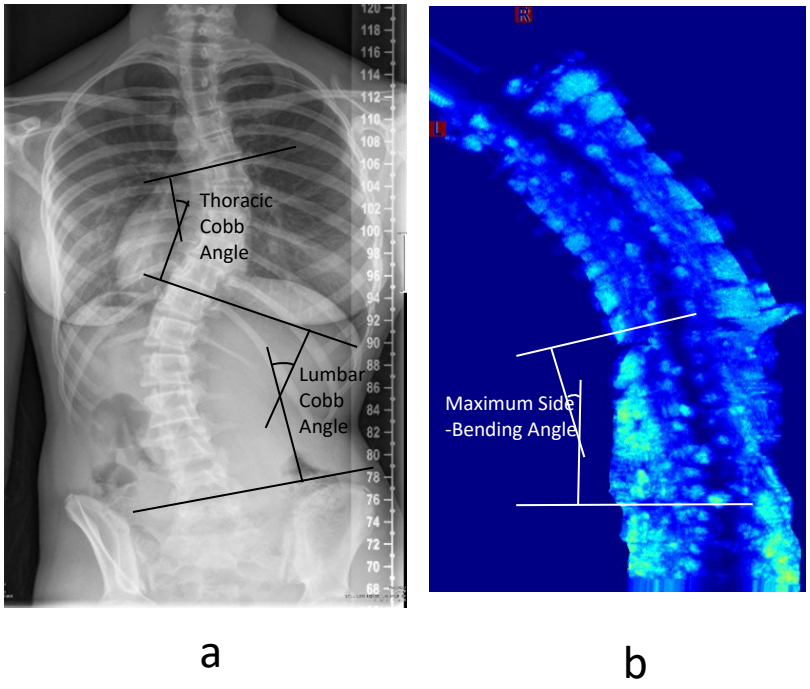

Figure 4-5. (a) The Cobb angle measurement on a PA radiograph and (b) the left prone maximum side-bending angle on an ultrasound image

4.2.3 Factors for the Spinal Flexibility Model

Five factors, which could be obtained from the standing PA radiographs and clinical records, were selected as prediction factors: i) Cobb angle (Cobb), ii) Risser sign (Risser), iii) apical axial vertebral rotation magnitude (AVR), iv) classified body mass index (CBMI) and v) number of vertebrae involved in the curve (Length). The Cobb, Risser and apical AVR were known factors influencing progression of

scoliosis [[23, 96] so it was hypothesised that they might have impacts on spinal flexibility. Body mass index (BMI) may reflect muscularity due to which a higher BMI likely predicts less movement of the spine in adolescents.

Due to limitations in the accuracy of Cobb angle and AVR, they were divided into bins of width 5 degrees each and assigned an index. For Cobb angle, 11-15° was index 0, 16-20° was index 1, etc. AVR magnitude was divided in the same way, with 0-4° being 0, 5-9° being 1, etc. BMI was converted into CBMI. CBMI classifies the BMI as underweight, normal weight, overweight and obese and assigns an index from 0-3 accordingly [97]. Length, counted here as the number of vertebrae within the curve, was included from a mechanical perspective as a longer structural element typically bends more than a shorter one under the same loading conditions. Two sets of measurements (Cobb angle, Risser sign, AVR and number of vertebrae in a curve) were taken one week apart by one rater with little experience in order to determine repeatability. The Cobb angle and the Risser sign were measured and identified from the radiograph, respectively.

4.2.4 Data Measurements

The apical AVR was measured using an in-house developed software which uses Stokes' method on a standing PA radiograph [62]. In the case of an apex between two vertebrae, the AVR value for each vertebra was measured and the larger value was used. To measure the AVR, the apical vertebra was first identified by observation of the most lateral deviation on the PA radiograph. Two ellipses were then overlaid on the area of the pedicles as demonstrated in Figure 4-6. The lateral bounds of the vertebral body at the narrowest point were marked and the vertebra level was identified, indicated by the line in the figure. The AVR for this vertebra is 7.2° rotated in counterclockwise direction when viewing from superior.

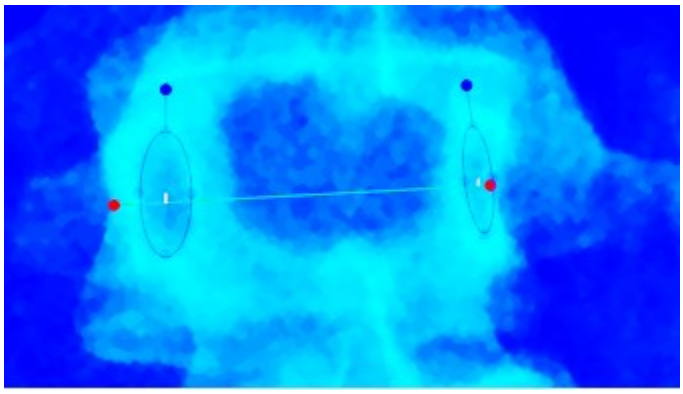

Figure 4-6. The selected landmarks on a vertebra to measure AVR using in-house software.

The BMI was calculated from the clinical records per the formula [97]

$$BMI = \frac{weight}{height^2} \quad (4\text{-}2)$$

In this equation, weight is in kilograms and height is in metres. Due to the extreme variability in percentile values, it was decided to assign patients CBMI based on Center of Disease Control classifications: underweight (BMI<5 percentile, classification 0), normal weight (5≤BMI<85 percentile, classification 1), overweight (85≤BMI<95 percentile, classification 2) and obese (BMI≥95 percentile, classification 3) [97].

4.2.5 Model Development and Analysis

To determine the intra-rater reliability on Cobb angle, AVR and prone maximum side bending angle, the intra-class correlation coefficient ICC[2,1] using a two-way random model with absolute agreement, MAD and standard error of measurement (SEM) were calculated using two sets of measurements taken a week apart. According to the Currier criteria, an intraclass correlation (ICC[2,1]) value of 0.90-0.99 indicates high reliability; 0.80-0.89 indicates good reliability; 0.70-0.79 indicates fair reliability; and <0.70 indicates poor reliability [99]. Standard error of measurement was calculated as [100].

$$SEM = SD\sqrt{1 - ICC} \quad (4\text{-}3)$$

where SD is the standard deviation of the measurement of a single trial.

To determine the relationship between the factors and the spinal flexibility, a single linear regression with leave-one-out cross-validation method was performed. Figure 4.7 contains the flowchart demonstrating the procedure.

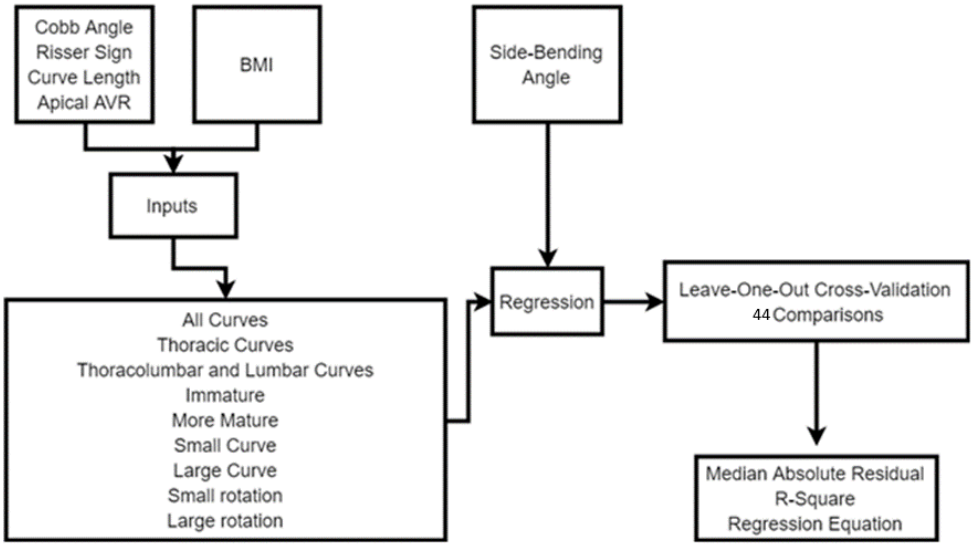

Figure 4.7. Flowchart for development of model

Linear regression was chosen due to it being a simple, well-established method which produces accurate results, and because the function was expected to be linear. Single regression was used instead of multiple due to the small data set. In leave-one-out cross-validation, each data set is repeatedly broken into a training set of N-1 data points and a test set of 1 data point, where N is the total number of data points. A linear regression is performed on the training set and then the residual is calculated from the test set. This method is repeated N times such that each point serves as the test set once. The difference between the predicted value of the test point from the regression and the actual value of the test point is the residual. The median of the absolute value of the residuals (MAR) is calculated as the validation statistic. The final linear regression uses all data points as its training set and produces a regression based on this. The validation statistic was used to evaluate the final regression. Another method of validation is called jackknifing, but for single linear regression this is equivalent to leave-one-out cross-validation. Leave-K-out cross-validation is another method, which is like leave-one-out cross-validation but instead of one point in each test set, there are K points, and there are N/K tests instead of N. Leave-one-out cross-validation is more accurate than leave-K-out cross-validation, so leave-K-out cross-validation is most appropriate for larger data sets when performing N tests would be excessively computationally difficult, requiring either too much computational time or too much computer memory.

Due to the small size of the data set, leave-K-out cross-validation with K greater than one is not appropriate; the computation time was less than a tenth of a second.

Several categorizations of the data were used. Each factor was matched with every subgroup, and the overall group, to try to determine if some groups, e.g. thoracic curves or large curves, can be better predicted than the aggregate group.

Nine sub-categories were considered. The first was the aggregate group, consisting of all curves. Two were made based on the region of the curve apex: thoracic (apex above T11), thoracolumbar (apex between T11 and L1) and lumbar (apex below L1). Due to the small sample size of data, thoracolumbar and lumbar made a combined set for analysis. This approach has been applied in [101]. Two sub-categories divided the data, based on curve severity, into Large Curves (Cobb >30°) and Small Curves (Cobb <=30°), with 30° chosen as the cut-off value because both the mean and median Cobb angles of all curves in this study were 30°. Two sub-categories divided the data based on bone maturity: Immature (Risser 0-1) and Mature (Risser 2), with Risser 2 being the maximum value found in the data set. For the latter sub-category, all values of Risser sign were identical, so doing a linear regression based on the Risser factor was not meaningful and therefore not performed for this sub-category. AVR was divided into Small Rotation (AVR Index <2) and Large Rotation (AVR Index>=2). Combining the nine sub-categories with five factors, and performing single linear regression on each combination, except Risser 2 sub-category with Risser factor, yields 44 tests to be performed. Table 4-3 shows the demographical and curve information of the 14 subjects. TL-L refers to curves which are either thoracolumbar or lumbar.

Table 4-3: Data Used in Analysis

Patient Number	Location	Flexibility (%)	Cobb Index	Risser	AVR index	CBMI	Length
1	T	54	0	0	3	1	4
	TL-L	76	2	0	2	1	3
2	T	95	6	1	1	1	6
	TL-L	81	6	1	2	1	5
3	T	50	2	0	0	1	4
	TL-L	92	5	0	3	1	5
4	TL-L	91	6	2	4	1	7
5	TL-L	85	4	0	3	1	5
6	T	69	3	2	1	1	5
	TL-L	70	5	2	3	1	5
7	T	77	2	2	0	1	5
	TL-L	78	4	2	0	1	4
8	TL-L	70	2	2	1	1	6
9	T	72	5	2	2	2	6
	TL-L	85	4	2	0	2	5
10	T-L	67	2	0	0	0	5
	TL-L	68	3	0	1	0	6
11	T	96	3	0	0	1	6
	TL-L	43	2	0	0	1	5
12	T	50	5	0	0	1	6
13	T	94	4	2	0	1	6
	Tl-L	41	4	2	0	1	4
14	T	87	2	2	0	1	7
	Tl-L	100	2	2	0	1	6

The “regstats” function in MATLAB 2016a was used to perform the linear regressions, yielding coefficient of determination R^2 and linear regression coefficients, slope m and y-intercept b (regression equation: Flexibility = m × Factor + b). The MAR was calculated for each regression.

4.3 Results

4.3.1 Intra-rater Reliability and Accuracy

Intra-rater reliability ICC [2,1], MAD and SEM of Cobb angle, AVR and bending angle are contained in Table 4-4, along with the repeatability reported in literature. All ICC[2,1] values are greater than 0.80, suggesting good reliability for Cobb, AVR, bending angle and flexibility, while MAD±SD stayed within the literature repeatability values. The SEM values were also smaller than the literature repeatability. Clinically, an error in Cobb angle smaller than 5° is deemed acceptable [102] while approximately a 6° error in AVR is expected [103], indicating that measurements were acceptable.

Table 4-4. Reliability of measurements of measured Cobb angle, AVR, bending angle and flexibility

Variable	ICC[2,1]	MAD	SEM	Literature repeatability
Cobb (n = 24)	0.96	(1.9 ± 1.4)°	2.3°	±4.9 [102]
AVR (n = 24)	0.82	(2.5 ± 1.8)°	2.9°	±6 [102]
Bending Angle	0.84	(2.1 ± 1.2)°	2.3°	±4.1 [104]
Flexibility	0.88	(7 ± 4)%	8%	Unpublished

4.3.2 Factors and Flexibility

The factors and associated flexibilities are presented in Table 4-3, divided into sub-categories, as described in section 4.2.5. The average and standard deviation of each factor and the curve's flexibility are shown. For the entire data set, the range of Cobb angle was 13° to 44°, yielding indices between 0 and 6, average 3.5±1.6. Risser value varied between 0 and 2 with an average of 1.1±1.0. AVR was between -24.1° and 11.2°, indices between 0 and 4 based on the absolute value, average 1.1±1.4. CBMI varied between 0 and 2 with an average of 1.0±0.4. Length was between 3 and 7 vertebrae with an average of 5.6±1.1 vertebrae. Flexibility had a minimum value of 41% and a maximum value of 100% with an average of 80.3±13.4%.

Table 4-5. Sub-category means and standard deviation for each measured variable

		Variable					
		Flexibility (%)	Cobb Index	Risser	AVR Index	CBMI	Length
Subcategory	Aggregate (n = 14)	80.3±13.4	3.5±1.6	1.1±1	1.1±1.4	1±0.4	5.6±1.1
	Thoracic (n = 11)	73.7±17.7	3.1±1.8	1±1	0.6±1	1±0.4	5.5±0.9
	TL-L (n = 13)	75.4±17.5	3.8±1.5	1.2±1	1.5±1.5	1±0.4	5.1±1
	Immature (n = 7)	80.3±16.9	4±1.4	0.1±0.4	1.4±1.3	0.9±0.4	5.3±1.1
	More Mature (n = 7)	82±10.1	2±0	2±0	1.5±1.8	1.2±0.4	5.8±1.2
	Small Curve (n = 8)	74.1±13.7	2.4±0.5	1±1.1	0.6±0.7	0.9±0.4	5.3±1.3
	Large Curve (n = 9)	80.8±14.9	4.9±0.8	1.2±1	1.8±1.6	1.1±0.3	5.6±0.9
	Small Rotation (n = 10)	76.6±15.6	3.5±1.6	1.1±1	0.5±0.8	1±0.5	5.8±0.7
	Large Rotation (n = 8)	80.5±9.7	4.1±1.4	1.1±1	1.9±1.4	0.9±0.3	5.2±1.1

4.3.3 Regression Results

Table 4-6 contains the coefficient of determination R^2 values for each factor and sub-category calculated from the linear regression method. Larger is better and a value of 1.0 is a perfect result, indicating that the independent variable completely predicts the flexibility. In this test it ranges from 0 (no correlation), for the Thoracic category with CBMI as the independent variable, to 0.43 for the Thoracic category as a function of Length. Table 4-7 shows the MAR values, which indicates the median value of the leave-one-out linear regression errors. They range from 5.6 for the Large Rotation category with AVR as the independent variable, to 21.7 for the Thoracic category with CBMI as the independent

variable. Smaller values indicate better results. The More Mature subcategory could not be performed with the Risser sign because all values of the independent variable were identical.

Table 4-6: R^2 for all sub-categories and factors

Subcategory \ Factor	Cobb Index	Risser	AVR Index	CBMI	Length
Aggregate	0.01	0.01	0.01	0.00	0.02
Thoracic	0.12	0.21	0.06	0.00	0.43
TLL	0.36	0.02	0.18	0.22	0.00
Immature	0.08	0.01	0.17	0.04	0.11
More Mature	0.01	0.15	0.11	0.1	0.00
Small Curve	N/A	N/A	0.05	0.24	0.33
Large Curve	0.05	0.02	0.03	0.03	0.22
Small Rotation	0.01	0.02	0.08	0.05	0.01
Large Rotation	0.02	0.08	0.01	0.11	0.05

Table 4-7: Median absolute residual values for all sub-categories and factors

Subcategory \ Factor	Cobb Index	Risser	AVR Index	CBMI	Length
Aggregate	11.6	13.2	11.9	12.1	11.1
Thoracic	17.7	14.9	20.1	21.7	9.7
TLL	9.6	9.5	10.9	6.1	12.4
Immature	14.2	17.0	12.4	15.2	19.1
More Mature	N/A	N/A	13.0	10.6	11.9
Small Curve	13.8	8.3	10.1	10.5	10.8
Large Curve	12.4	14.3	10.6	13.6	13.8
Small Rotation	10.6	12.7	10.0	10.8	12.3
Large Rotation	10.7	11.1	5.6	10.2	12.0

Figure 4-8 contains the plot of the regression results for Thoracic curves with Length, which had a mean absolute residual of 9.7% and a coefficient of determination of 0.43, the best of the data set.

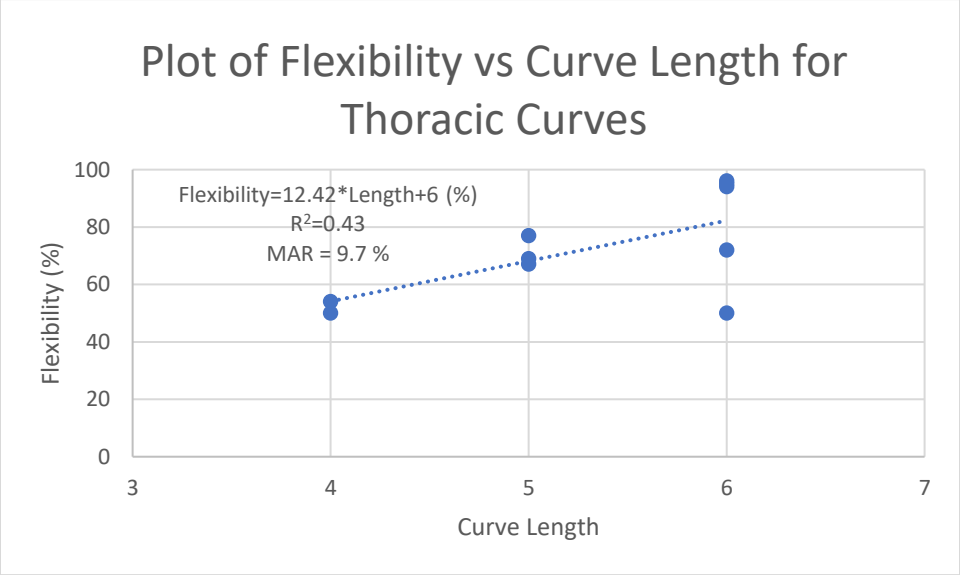

Figure 4-8. Results for Thoracic curves with Length factor

4.4 Discussion

With these fourteen patients, the highest coefficient of determination that could be found was 0.43, for Thoracic curves with Length as the predictive factor. For a single linear regression with only fourteen patients, this is an acceptable start. MAR was as low as 5.6%, indicating that results could be accurate to a good degree.

There may be a difference in flexibility between prone ultrasounds and supine radiographs because of the position, as there is coupling between sagittal shape and coronal curve [33, 34]. Further comparison may be possible in the future if brace patients become routinely tested for flexibility, which may result from wider application of ultrasound flexibility tests.

Contrary to a previous study [105], curve magnitude (R^2=0.01) and skeletal maturity (R^2=0.01) were not good predictors for the aggregate group, although in that study the average Cobb angle was 56 degrees and perhaps not directly comparable as a result.

The shortage of patients with high Risser signs was a limitation. Based on the Scoliosis Research Society brace study recommendations [68], it would be better to divide patients into Risser 0-2 and Risser 3+, instead of Risser 0-1 and Risser 2, but there were no patients with Risser 3+.

As the aggregate group, the intuitive group to choose if only one category was to be used, did not yield the best results despite having the highest number of data points, the strategy of dividing data points into categories seems to have paid off.

As this was a pilot study, there is room for improvement by increasing the number of patients. This would smooth out random variation and allow multiple linear regression, which could yield better results

4.5 Conclusion

In this chapter, a pilot study of flexibility measured using ultrasound for fourteen brace subjects was reported. Single linear regression was used and revealed results that are perhaps useful but should be improved with a larger data set. R^2 reached 0.43 and the linear regression test statistic was as low as 5.6% so estimates of flexibility can be performed with some confidence, but more testing should be performed. There were insufficient numbers of patients to do a good analysis on Risser sign in particular, due to having no patients with a Risser sign of 3+. The separation of data points into separate categories seems to have paid off by producing better results. All considered, this research is a good first step towards allowing widespread flexibility use in scoliosis bracing.

Chapter 5: Development and Validation of 3D Brace Casting Frame for Assisting Brace Design

5.0 Summary

This chapter describes the process of research and development of a new 3D brace casting frame to assist orthotists to design better braces to treat adolescents with idiopathic scoliosis. In section 5.1, the background and motivation behind the frame construction are reported; a review of brace construction techniques has been performed and the method which has been used to design a brace was explained. In section 5.2, the design process and evolution of a three-dimensional wooden frame is fully described, in which the design process mainly focuses on the bolster supports. The final design is reported in section 5.2.12. The design challenges encountered are explained in section 5.3. Durability verification of the frame and associated tools which are used to help brace design are described in section 5.4, while laboratory trial on two patients is outlined in section 5.5. The chapter is concluded in section 5.6.

5.1 Review of Existing Casting Methods

In section 2.3.4 of this thesis, the general casting process for scoliosis braces is described. A research study which introduced using ultrasound scans to assist brace casting was conducted at the Glenrose Rehabilitation Hospital, Alberta, Canada. Using ultrasonography during the bracing process, the number of brace adjustments – and in turn, the number of in-brace radiographs – was greatly reduced [106], indicating the usefulness of this technology. Under this study, a customized Providence-style frame was developed and used. As mentioned in section 3.1.4, the Providence system uses up to four bolsters: axilla, thoracic, lumbar and trochanter as shown in Figure 5-1. These apply loads to correct the spinal curvature. The patient stood against a standing board and the Providence system bolsters were applied to the body at up to four sites, depending on the curve pattern (Figure 5-1) (see section 3.1.6 for more details).

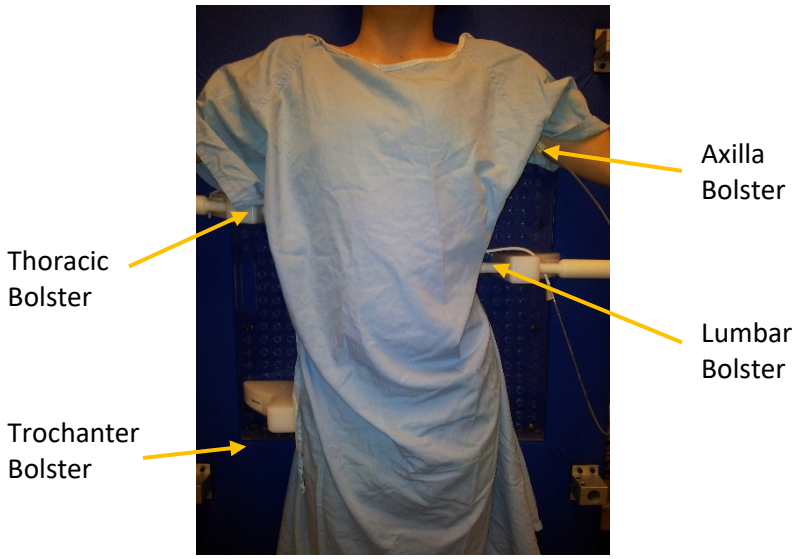

Figure 5-1. Volunteer on Providence board with bolsters labeled [52]

This configuration generates 2D correction, working only in the coronal plane. An ultrasound scan was taken to confirm results in which the orthotist was aimed for based on the experience; if the result was deviated from the expectation, the position and the pressure applied by the bolsters would be adjusted. The ultrasound scan had the patient in a standing position and the scanner was moved from C7 to L5 along the curve of the spine. Figure 5-2 contains an image of the ultrasound system and a patient being scanned. This is not a brace casting scan, but the figure serves to illustrate the ultrasound components which are explained in this chapter.

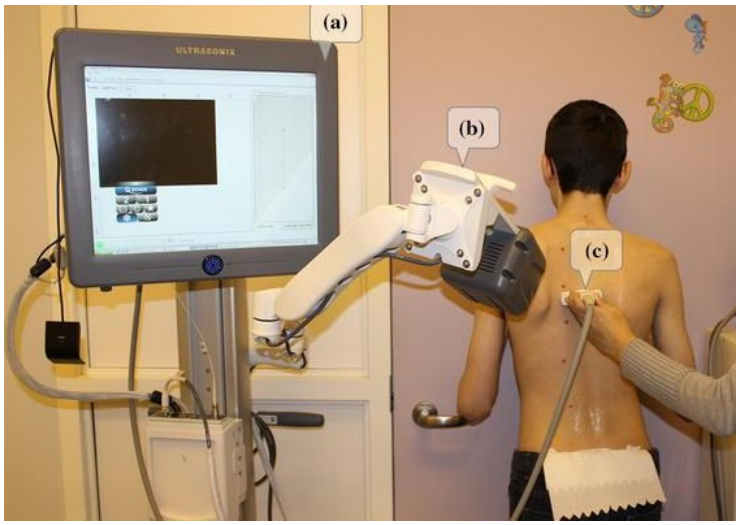

Figure 5-2. Ultrasound equipment and patient a) ultrasound console, b) position tracking system (GPS), c) ultrasound transducer [107]

Using subjective judgment, the clinic in the Glenrose Rehabilitation Hospital attempts to achieve correction of 35-50% immediate correction, although less correction may be subjectively deemed acceptable in the case of a particularly stiff spine. Once the pad placement was decided, the patient was wrapped in plaster bandages and requested to lay on a Providence brace design system. The bolsters were applied in the same positions as those in the standing position in order to obtain similar correction to that measured in the standing frame. After the plaster mold of the body was dried and removed from the patients' body, it was then scanned with a handheld laser scanner (OMEGA, USA) to generate a 3D CAD model. This 3D CAD model would then be modified digitally to produce the final form of a brace, including 3D correction.

The frame helped hold the patient in place for ultrasound scanning and followed the same procedure as performed by Zheng et al, 2014 [108]. The ultrasound system included a guidance positioning system (GPS) transducer which was thought to receive interference from nearby metal. The ultrasound system was used to aid in casting by allowing the orthotists to see the effects of the pad forces on the patient's curve before the follow-up visit; this technique was found to reduce the likelihood of requiring a brace modification and only one out of seventeen patients cast with this technique required an adjustment while eight out of 17 traditionally-cast patients required an adjustment [109]. As a result, there was reduced radiation exposure and a reduced cost due to needing fewer follow-up appointments and radiographs.

Ultrasound has also been used by Li et al., 2012 [110] to improve bracing results by selecting an optimal thoracic pad position. They measured the spinous process angle rather than the proxy Cobb

angle. In that study, only the location of the thoracic pad was modified. Prior to finalizing the thoracic pad location, the first location was subjectively designed by the orthotist based on the radiographs. They then scanned the patient using ultrasound while the patient was wearing the brace. The spinous process angle was used as the determining criterion. To determine the spinous process angle, the spinous process was identified as a bright spot in the ultrasound scan. The spinous process angle was determined by summing the angles between consecutive spinous processes. There was a prescribed pad location going into the casting clinic, and there were only five options for pad placement: prescribed level based on radiograph, 1 and 2 cm above the prescribed level, and 1 and 2 cm below the prescribed level. At these various settings, the spinal process angle was measured at each pad location.

The Glenrose study was more flexible, involving three or four pads depending on whether it was a single or double curve, and allowing large changes in the location and force levels, with some pads moving several vertebrae up or down. Centre-of-lamina proxy Cobb angle was used instead of the Li et al. study's spinous process angle. Bolsters were adjusted during casting measurements instead of changing the thoracic pad with the already-built brace. Like the Glenrose method, the Li et al. method yielded better results than the traditional method, indicating that whether spinous process angle or proxy Cobb angle is used as the metric, ultrasonography in brace development can yield better results in the in-brace correction radiograph.

Ultrasonography allows the results of the casting to be viewed immediately rather than having to wait several weeks to do a follow-up radiograph. Pressure measurements allow optimization of loads while avoiding discomfort without having to fit the brace to the patient to find problems.

Ultimately, existing casting methods are passable but call for improvement. Generally, loads are unknown during casting and the ultrasound method is essentially guess-and-test, and this process can be improved with increased measurements during the casting process. Fully 3D casting is rare in North America and should be implemented to produce better results overall.

5.2 Frame Construction

The ultimate goal of the research found in this chapter is to increase the objectivity in brace casting, assist the use of real-time feedback, and require fewer brace adjustments and therefore fewer radiographs. The existing Providence-style bracing board is basically limited to apply two dimensional coronal forces to patients. The 3D correction is subjectively adjusted by the orthotist using the CAD/CAM software post-casting. To investigate the 3D spine response during brace casting, a frame

which can accommodate bolsters to move three-dimensionally is necessary. Having full 3D information available at the time of casting may potentially reduce the number of adjustments and improve prediction of in-brace correction. As part of increasing objectivity, ultrasound and pressure measurements were used, which allowed quantification of correction at time of casting and a suggestion of patient comfort before making the brace, respectively.

5.2.2 Tools Used to Construct Brace Frame

Bolster contact pressures, angles and forces were desired. The contact pressure is important to the casting process as it prevents excessive pressure on the skin which can lead to discomfort while the latter two are important for casting analysis purposes, to be used in the simulation constructed in Chapter 6 which reports on a developed algorithm that helps to predict brace casting efforts. To acquire this information, a pressure/angle acquisition system was developed by Chalmers et al. [111]. It consisted of an air bag system to measure pressure which consisted of a pressure sensor, pump and valve pressure mechanism and an inertia sensor which consists of a 3-axis accelerometer and 3-axis gyroscope. A schematic for the pressure airbag system is shown in Figure 5-3.

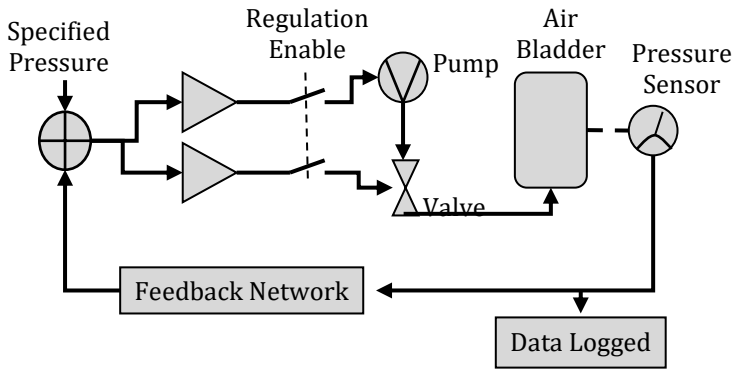

Figure 5-3: Pressure airbag schematic [111]

Three methods were considered for determining the forces applied: pressure airbags, strain gauge, and load cells. Strain gauges were difficult to incorporate into the geometry of the bolster supports while the load cells were too expensive, costing several hundred dollars per load cell. The pressure system was decided upon.

To calculate the force from the pressure airbags, the pressure needs to be multiplied by the contact area (Equation 5-1)

$$F = P \times A \tag{5-1}$$

In Equation 5-1, F is the force in newtons, P is the pressure in pascals and A is the area in square metres. The contact area between a deformable airbag and the human body is difficult to determine analytically so tests were performed using a load cell to find a linear model of the contact area as a function of patient thoracic and lumbar circumference and bolster angle.

5.2.3 Design Criteria

A standing frame was required as the basis of the design. It supports the patient in a standing position while applying forces through bolsters. By using the Providence-style system, up to four bolsters were required. The axilla and trochanter bolsters only required three degrees-of-freedom (DOF) (translation only – up, down; anterior, posterior; left, right) and two bolsters required five DOF (three DOF translation; rotation around the superior-inferior axis; rotation around the anterior-posterior axis). The ability to provide forces up to 128 N per bolster was required, based upon the maximum pressure expected (about 125 mmHg) [112] and the maximum surface area of the selected air bag was 7500 mm^2. The design needed to be user friendly and able to be adjusted without using any tools.

5.2.4 Existing Design: Aluminum Collar Clamp on Metal Frame

Prior to my study, a steel and aluminum frame with six bolsters was designed. The frame, showed in Figure 5-4, was constructed from aluminum. All of the bars had channels for T-nuts which allowed connection and movement of components. It featured a casting board against which the patient stood, supported by aluminum bars. The casting board had a 114 mm wide slot in the back to allow the ultrasound scanner access to the spine, as shown in Figure 5-5.

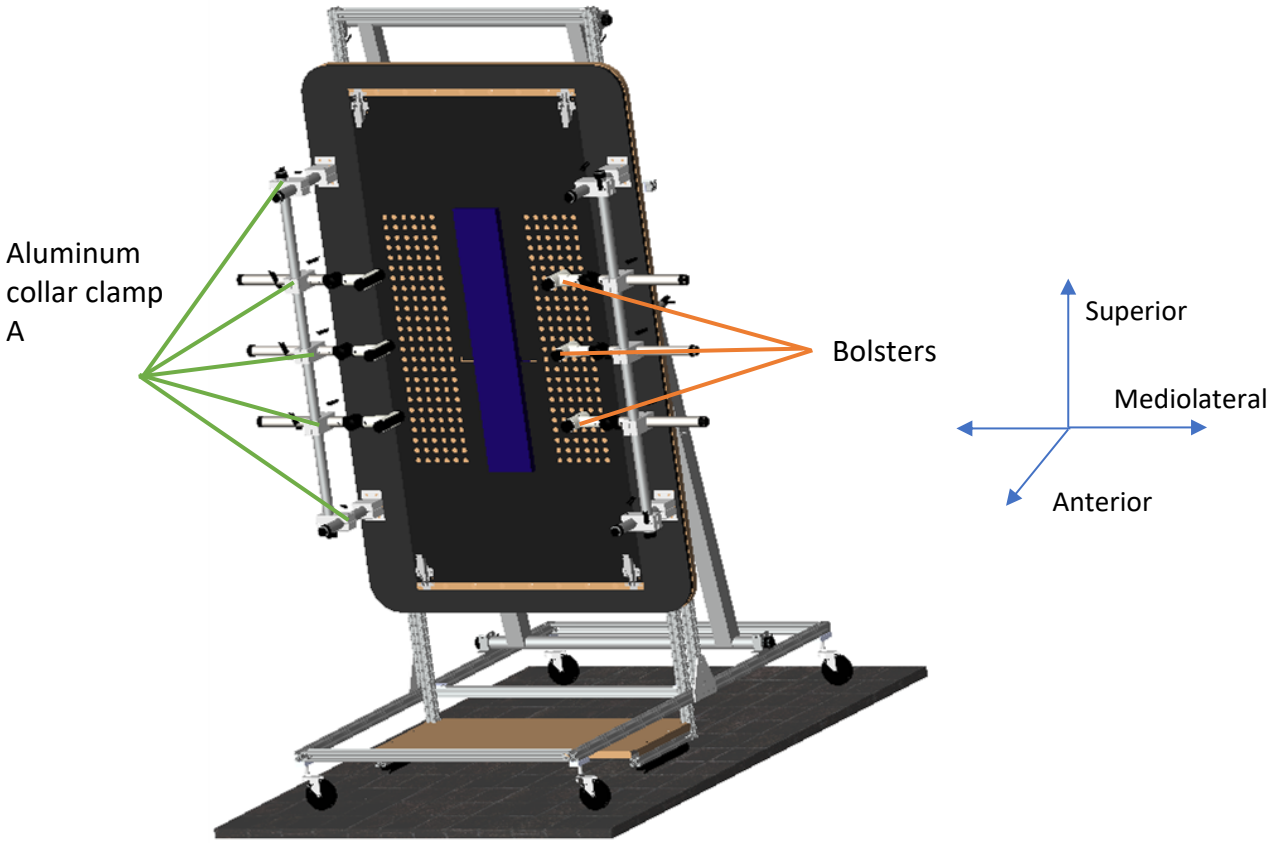

Figure 5-4. Aluminum Collar Clamp on Steel Frame

Figure 5-5. Back of old frame, demonstrating ultrasound access slot

Attached to the casting bar were six bolsters, supported by aluminum pieces that allow rotation (ACA), shown in Figure 5-6. These aluminum pieces allowed rotation as shown in Figure 5-7.

Figure 5-6. Aluminum collar clamp A

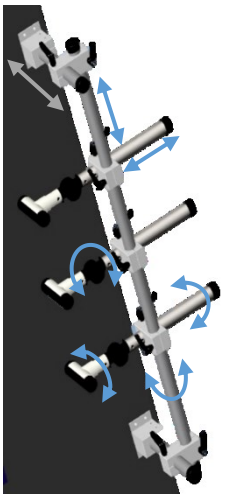

Figure 5-7. Rotations allowed on old frame

The bolsters were cylindrical. They were able to rotate at the very end of the bolster supports, but this only changes the bolster position and not the force vector, which is dictated by the rod supporting the terminal piece. The bolster supports could move in the mediolateral direction and vertically, and there was limited motion in the anterior-posterior direction, due to the bolsters on one side all being moved at once. Rotation around the superior-inferior axis was limited. They allow continuous rotational motion between rods at right angles. The handles can be adjusted by hand sufficiently to terminate movement. The frame was on wheels to allow movement within the clinic with a floor lock for stability once in position. The casting board could be tilted into a lying position to allow casting to occur in that position.

One advantage of the approach used is its strength and stability. The bolsters are very well supported in a way that was not recreated with later iterations. However, there is naturally a trade-off between rigidity and mobility; the bolsters in this design are not able to produce large angles in the transverse plane.

Ultimately this design was rejected because the orthotists preferred a Providence-style with four bolsters with an anatomically derived shape rather than the six cylinders found on this design. The bolsters were removed, and a Providence-style pegboard was put in place, but this left it as two-dimensional.

5.2.5 Design Process

To improve the existing old metal frame, a new design of a wooden frame with bolster supports was built. The following section described the functions of the wooden frame which allowed patients to

stand in the middle of the frame. Five iterations, labeled A through E, of the bolster supports used on the wooden frame are described in detail to reflect the challenges of the design.

5.2.6 Three-Dimensional Wooden Frame

The frame is depicted in Figure 5-8.

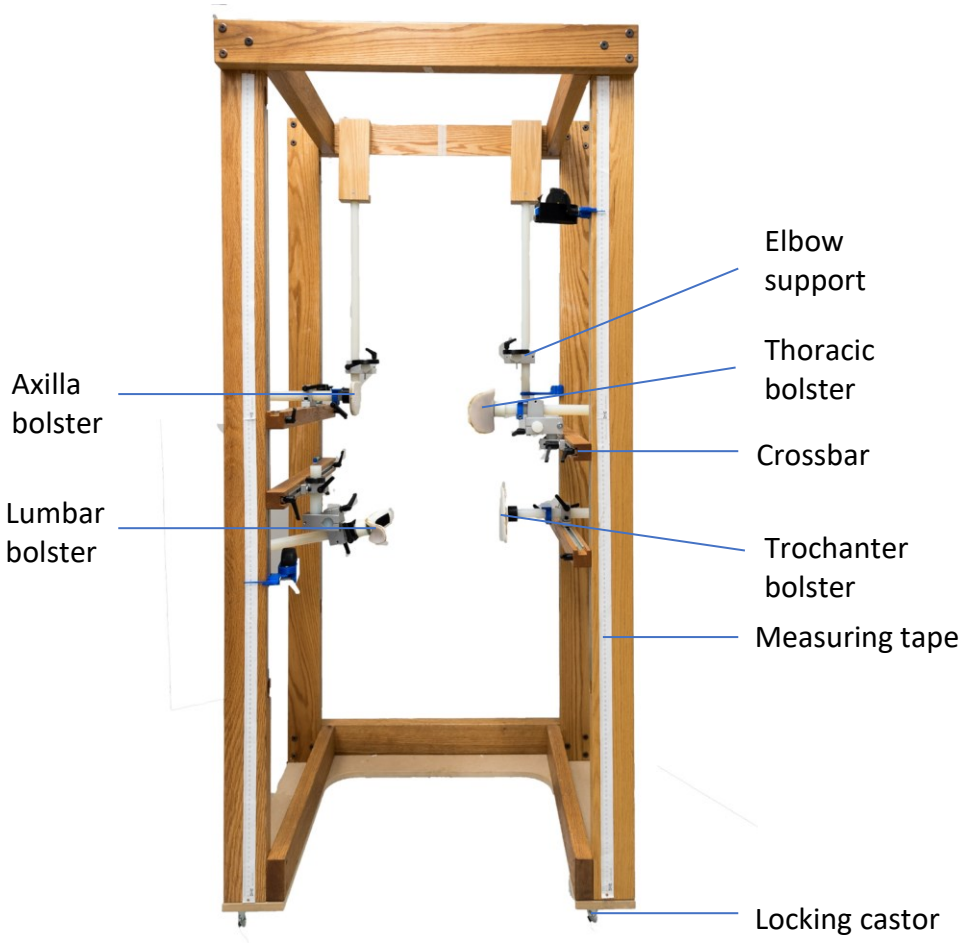

Figure 5-8. Completed frame configured for right thoracic, left lumbar curve

The frame was constructed primarily from wood, with a base, top and four vertical supports. The vertical supports had metal grooves for attaching the crossbars with a T-nut. There were elbow supports at the front of the frame to help hold the patient in place. Nylon rods held the elbow supports in place. Four crossbars were used to support four bolsters at the trochanter, lumbar, thoracic and axilla region, in line with the Providence system (Figure 5-1). A measuring tape was present on the front of the frame to determine the distance between bolsters. The frame base was on locking castors to allow it to be moved between rooms in the casting clinic.

5.2.7 Bolster Supports

3D printed parts and accessories were used in most of the iterations at the beginning. However, because of the strength and flexibility requirements, the iteration designs gradually used more metal in the bolster supports as it was discovered that it did not affect the ultrasound GPS system as much as was initially thought. The final design uses aluminum parts connected with Nylon rods. The Nylon rods were chosen because they were available and had suitable strength and friction properties, with a measured coefficient of static friction of 0.2 with aluminum.

5.2.7.1 Construction Tools for Bolster Holders

The original goal was to use 3D-printed plastic to create the bolster supports. Metal was thought to be undesirable because of interference with the ultrasound GPS unit, which was a technology used to determine locations and orientation of the ultrasound transducer. A 3D printer, a Replicator 2X (MakerBot Industries, LLC, Brooklyn, NY, USA), was available. It offered a fast turnaround time and the ability to print any shape that was desired in a variety of strength and density combinations, in addition to reducing costs.

This 3D printer supports both polylactic acid (PLA) and acrylonitrile butadiene styrene (ABS) filaments to print the design. ABS was used for the design because it has a higher elongation at breaking (up to 25% [113]) compared to PLA (up to 10% [114]). To print, the fused deposition modeling (FDM) method was used. In this, a 1.75 mm diameter ABS filament is melted and extruded through a nozzle onto the build plate. The head moves in the horizontal plane while the build plate moves down for successive layers. Layer height is between 0.1 and 0.3 mm (according to user needs), with smaller layer heights allowing finer features but lower strengths. The weak point of 3D-printed ABS is the connection between adjacent layers; more layers implies worse bonding. To construct a layer, a geometric pattern is laid out. By default, it is a hexagonal structure. The infill indicates how dense the pattern is in the direction perpendicular to the layer height. Excluding edge effects, a 10% infill indicates that on a given layer, only 10% of the area of the body will be filled with solid material. A 100% infill indicates that a solid layer of plastic has been laid down. 100% infill yields a part that is strong but inflexible, while 10% is quite flexible but weak.

Strength was also anisotropic due to the strength depending on layer interfaces. Strength also changes with horizontal orientation due to the anisotropy of the infill pattern.

5.2.8 Plastic Collar Clamp (CP) Bolster Holder

Following the metal frame, the next design aimed to largely recreate the aluminum bolster holder idea but with plastic instead. The design was titled Plastic Collar Clamp. The design is shown in Figure 5-9.

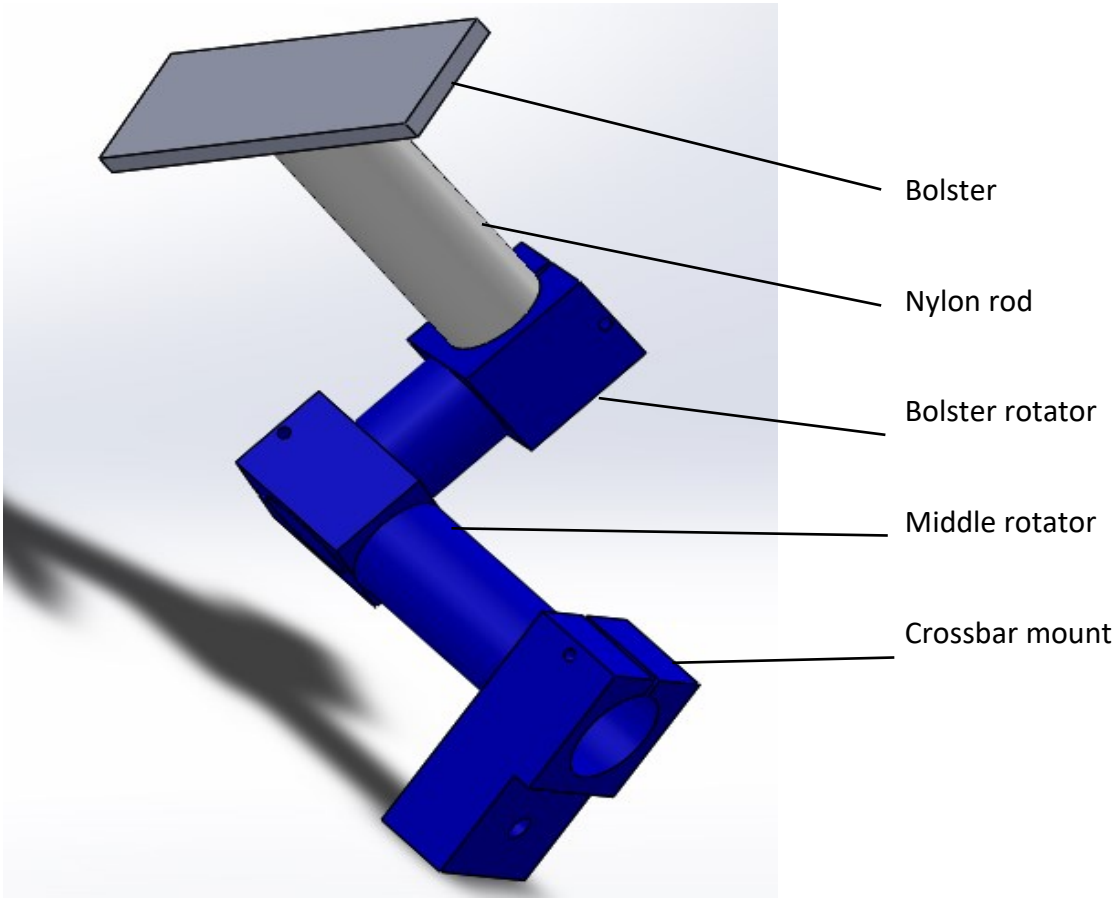

Figure 5-9. Plastic collar clamp set

The 3 DOF bolsters are attached to the crossbar via piece plastic collar clamp A (PCA) (Figure 5-10).

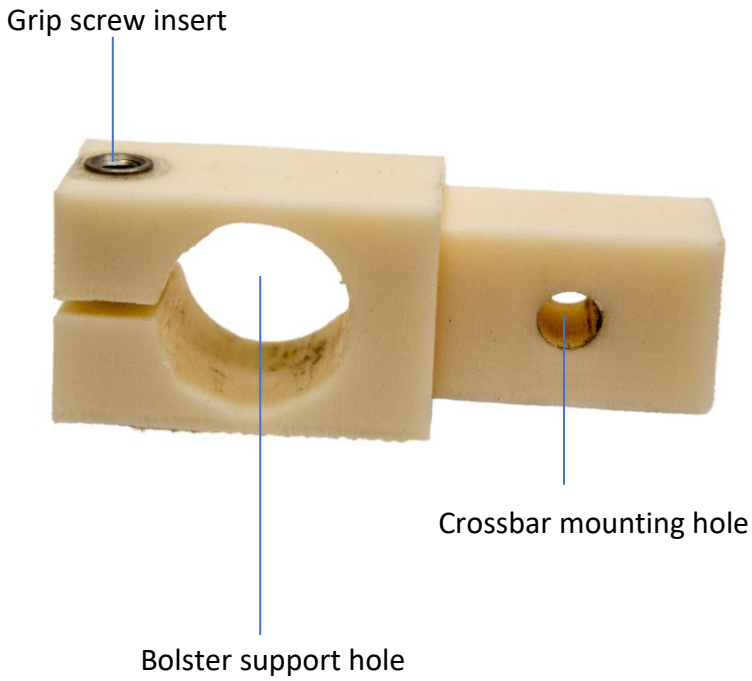

Figure 5-10. Plastic collar clamp A

The PCA has two functional parts: the mount and the grip. The mount has a flat face with a 6.4 mm crossbar mounting hole to allow a threaded handle to go through and attach to a T-nut in the rail in the crossbar, holding the part against the crossbar (Figure 5-11).

Figure 5-11. PCA mounted on crossbar

A lip was present where the piece meets the top of the crossbar to provide stability against rocking. The distance of this lip was required to be precise and this proved problematic a lot of the time.

The grip consisted of a bolster support hole about 25.4 mm in diameter to accommodate the rod with a slot at the top to allow it to bend and a hole perpendicular to the slot. A threaded insert was placed into one end of the hole to allow a threaded handle to close the grip tightly around the rod. When this was overtightened, the piece tended to crack; low infill percentage pieces (<25 %) could be tightened more without cracking due to having improved flexibility. Required strength for this piece was low, so low infill percentage was used.

For the 5 DOF set, the first piece was PCA. For the second and third pieces, plastic collar clamp B (PCB) was used (Figure 5-12).

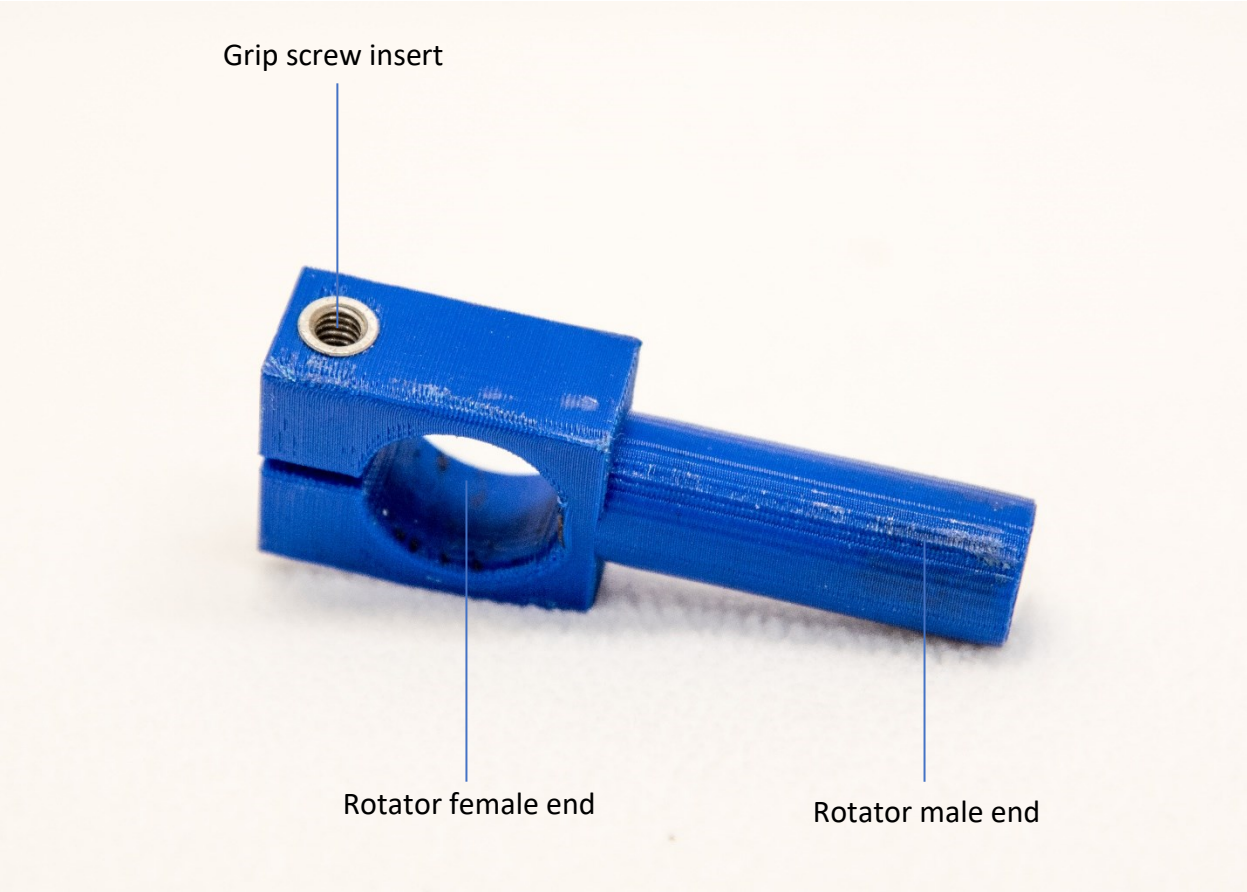

Figure 5-12. Plastic collar clamp B

The pieces had a male end and a female end. The male end was a protruding cylinder while the female end was similar to the grip end of the PCA. For the PCA and the first PCB, rotation alone was desired with no translation. For the final piece, translation was desired. Rotation around the postero-anterior and superior-inferior axes comprised the extra two DOF compared to the 3 DOF system. Rotation around the medio-lateral axis was possible but not desirable, as it only changed the orientation of the bolster pads.

PCB was required to allow easy motion when the grip handle is loosened but to lock firmly when it is tightened. This, especially for the 5 DOF pieces, did not prove feasible due to material limitations in strength and flexibility. To tighten to a firm grip, flexibility was required. To sustain the large moments characteristic of the 5 DOF system, strength was required. Strength and flexibility are inversely related in pieces made by the printer so suitable pieces were unable to be produced.

5.2.9 Plastic Collar Clamp with Rubber

The following attempt used the same design as the plastic collar clamp attempt but had rubber sleeves made to interface between the male and female ends (Figure 5-13).

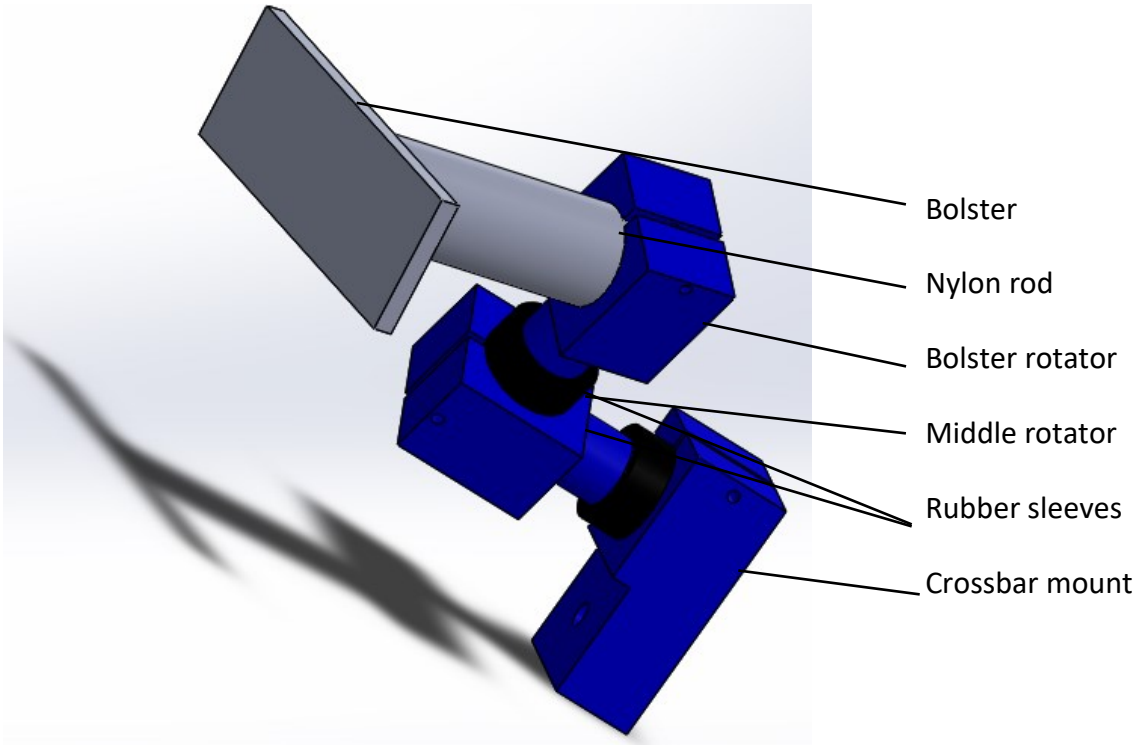

Figure 5-13. Plastic Collar Clamp with Rubber

The hypothesis was that the increased friction from the rubber contact would allow tightening with less bending, thus preventing breakage. Pieces were reprinted with a larger female end than male end and then a sleeve cut from a 3.2 mm rubber sheet was used to fill the gap. It was successful in allowing them to lock well but it did not allow smooth enough motion during readjustment, and thus was deemed unsuitable.

5.2.10 Screw System

After the failure of the plastic collar clamp with Rubber, the connectors were overhauled into the screw system (Figure 5-14).

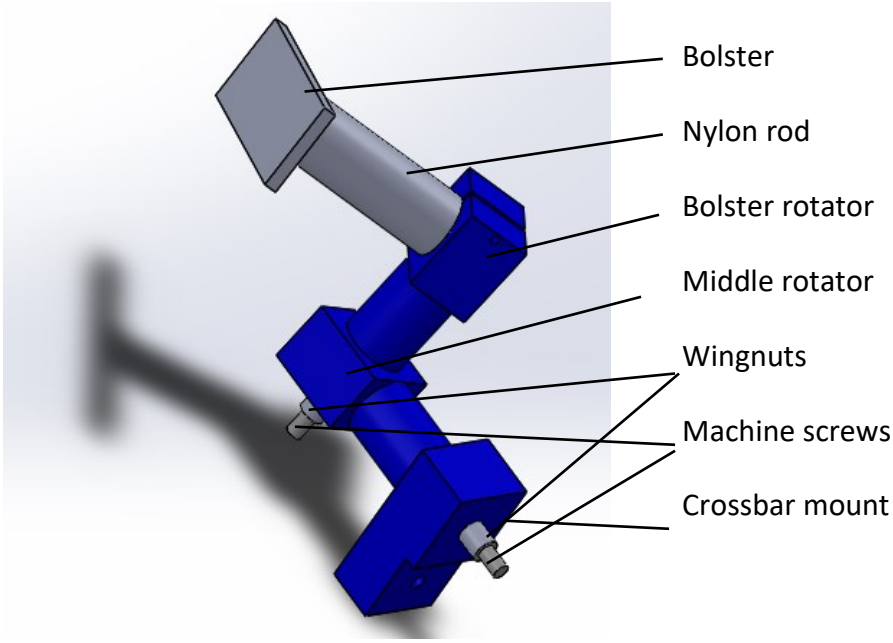

Figure 5-14. Complete Screw System

The male end consisted of a steel machine screw mounted within a round plastic housing (Figure 5-15).

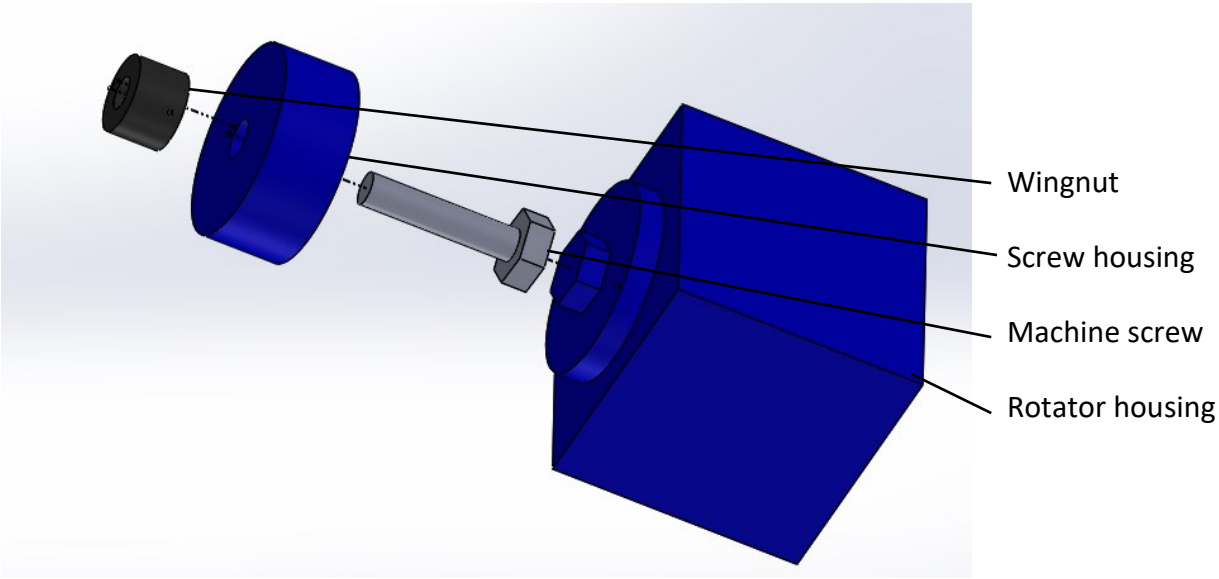

Figure 5-15. Screw System middle piece

The female end was modified to have a round hole slightly larger than the bolt housing and a smaller hole just bigger than the screw diameter. When mated, the screw extended through the smaller hole. To arrest motion, a wingnut was tightened, producing a high normal force between the male and female pieces. The force generated was not enough for a friction lock to occur. In a second revision, rubber was added. However, even with the added rubber, there was insufficient friction when fully tightened by hand, so this design was rejected.

5.2.11 Steel Collar Clamp

The next design attempted to use some steel, contrary to the design requirement of no metal. Steel collar clamps were mounted in 3D printed parts, using Nylon rods to connect the rotators. This led to little stress being on the actual plastic, with the clamping forces applying mostly to the steel collar clamps. Figure 5-16 shows the piece that straddles the crossbar (SCA). Figure 5-17 shows how SCA mounts on the crossbar.

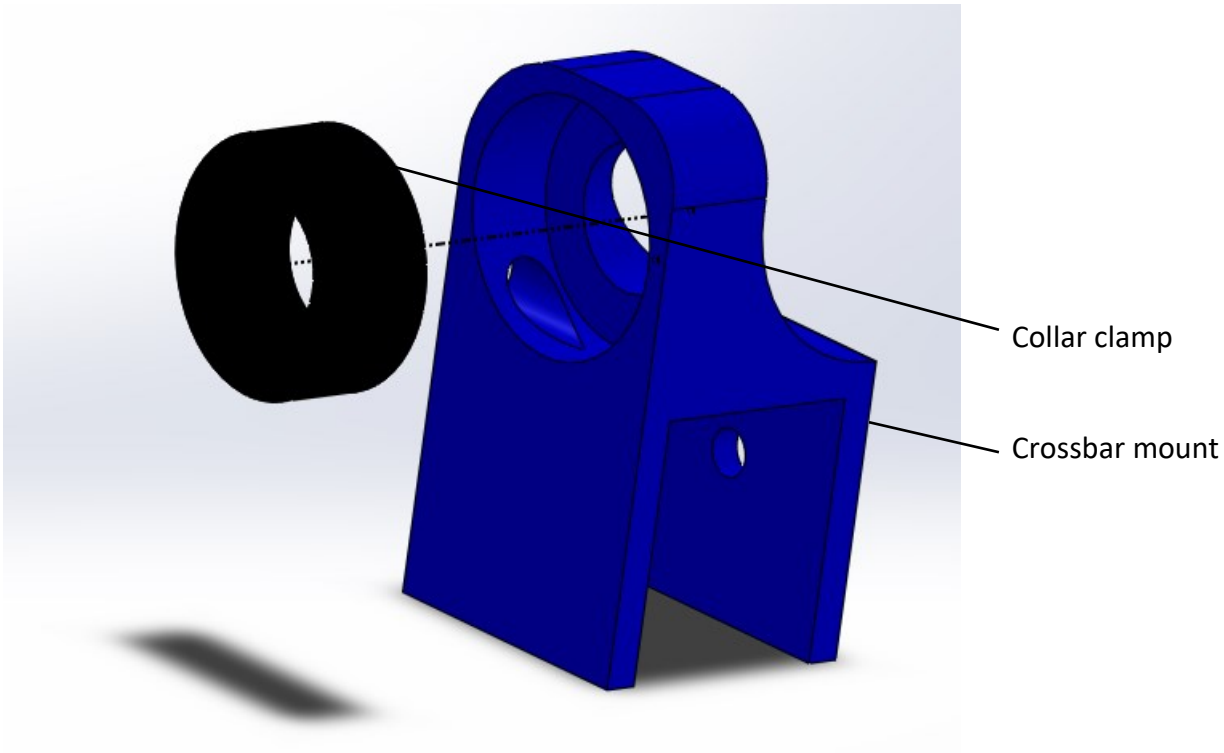

Figure 5-16. Steel collar clamp crossbar connector

Figure 5-17. Mounting of SCA

Figure 5-18 shows the middle rotator (SCB).

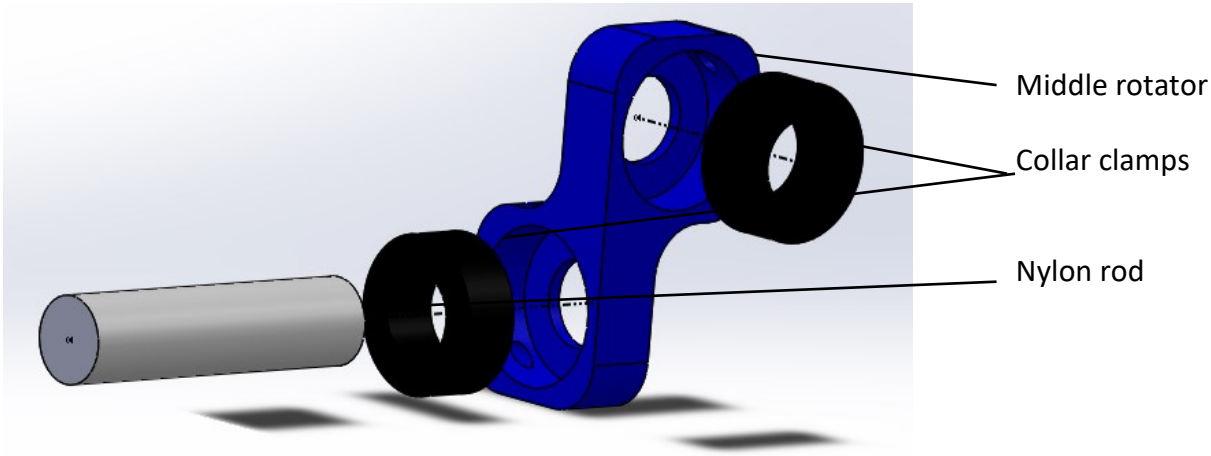

Figure 5-18. Steel Collar Clamp Middle Rotator

To tighten the collar clamp, a handle was designed using an all-thread shaft epoxied into a 3D printed base. For the 3 DOF bolsters, the PCA piece was used.

The GPS was tested again to see if the collars interfered, but they did not. After noticing this, the middle pieces were replaced with ACA. In a test with the clinicians, a PCA cracked from being overtightened. Knowing that aluminum was not an issue, off-the-shelf aluminum rod holders (ACB, (Figure 5-19)) were implemented. Poor grip at high loads also proved to be an issue with one of the SCA so that was also replaced with an ACB.

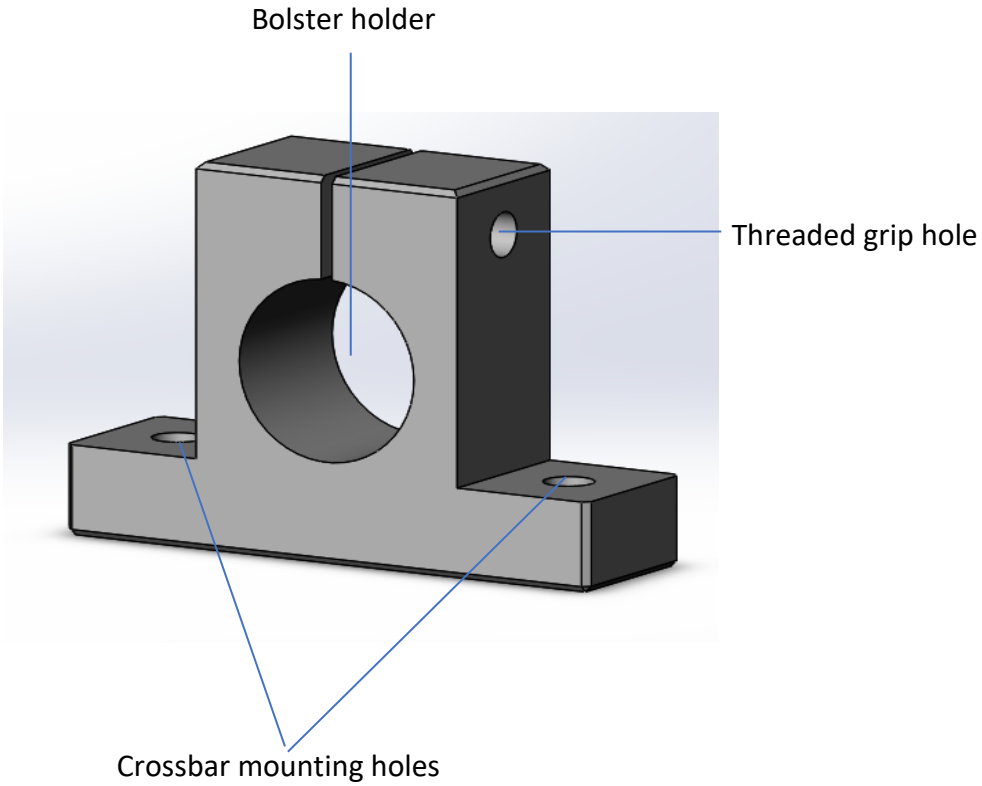

Figure 5-19. Aluminum rod holder

5.2.12 Final Bolster Support Design

The final design is shown in Figure 5-20.

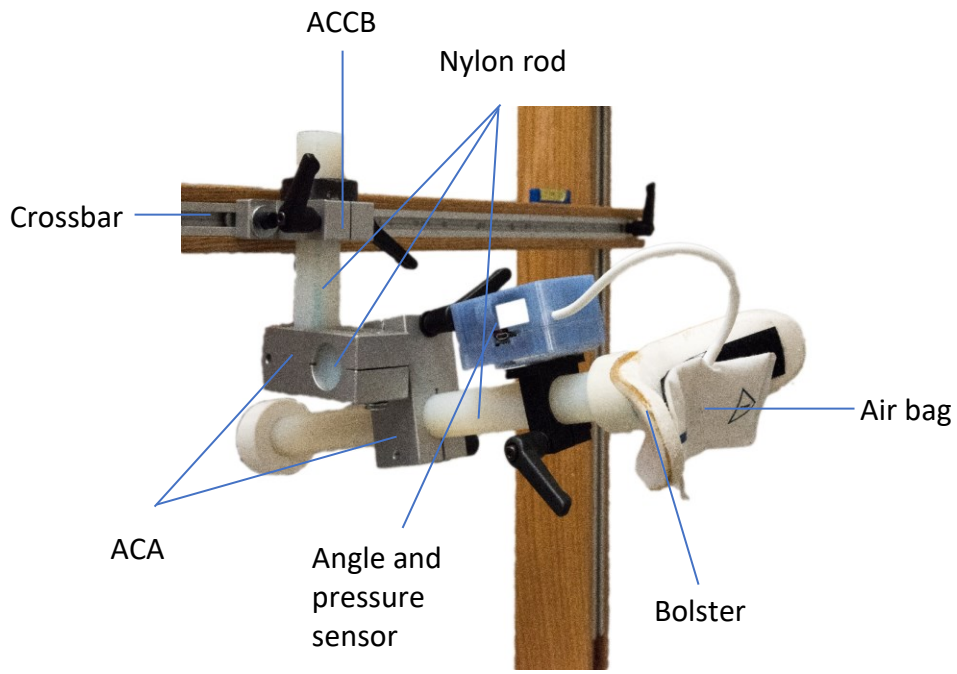

Figure 5-20. Final design for 5 DOF

The 3 DOF mounts were off-the-shelf ACB. These were tested by the orthotist and deemed to be satisfactory. They do not break with any amount of tightening and adequately arrest motion of the bolster supports. They are held in the track by two steel T-nuts; one side, closest to the handle to grip the rod, is a partially tightened hex-head screw, while the other uses a handle. The hex-head screw is tightened enough that it arrests motion perpendicular to the track while being loose enough to allow motion parallel to the track. The handle side is used to lock the component in place when it is in the correct position.

The 5 DOF starting mounts were the ACB mentioned above, and then two ACA were used for the other two pieces, connected by 25.4 mm diameter nylon rods.

The rotator following the ACB uses fully tightened hex-head screws to arrest motion as handles would be redundant and make it more difficult for the orthotists to learn the system fluently. Motion on the crossbar side is allowed by the ACB while motion on the bolster side is allowed by the third rotator. For the lumbar pad (shown in Figure 5-21), a steel collar clamp is used to keep the device from falling out when ACB is loosened.

On the bolster rod is a plastic collar clamp with a flat rectangular side with Velcro on it; this is to hold the angle/pressure sensor in place. It uses a low infill percentage because strength is not required. Additionally, there is a 5 cm diameter circular piece of 3D-printed plastic with rounded corners on the back end of the bolster rod for comfort while pushing the bolster in.

Petroleum jelly is used to lubricate the places where parts contact the crossbars, such as between the crossbar mounts for the bolster supports and the place where the crossbars contact the vertical columns.

5.3 Challenges in Constructing Frame

The plastic used tended to be either brittle and inflexible or flexible and weak, depending on infill pattern and density; both were problematic. Finding a compromise between these two extremes was a goal in all plastic designs and multiple pieces had to be tested for each iteration of design. Eventually the compromise was felt to be insufficient, so metal was used.

Aluminum was not thought to be useable due to issues with the ultrasound GPS reported by prior efforts. However, as more metal was incorporated into the design and tested, doubts were cast on these reports. Eventually, aluminum was deliberately placed around the GPS system and testing showed the accuracy of the GPS still worked within an acceptable error. This evolved to the final design as described in the above sections.

The 3D printer proved to be of generally poor reliability frequently failing in the middle of prints. It has no error monitoring (e.g. a way of determining that there is not enough filament) or correction (e.g. stopping the print until the filament is refilled), so even a slight failure can ruin the print. One frequent problem was that the filament would occasionally stop feeding. It was due to the feeding mechanism using a fixed diameter method, allowing slipping and therefore print failure if the filament diameter changed slightly. A replacement feed mechanism was installed which used a spring to hold the filament against the drive motor, mostly resolving this issue. If the part fails to stick to the platform, or if one layer fails to stick to the previously printed layer, failure occurs.

Poor dimensional accuracy was an issue as well. For a nominally 25 mm diameter hole, the error ranged from 0.5-1.0 mm. Since friction fits were commonly used in the design, this was one of the major sources of repeated difficulty. Also, since the printed material is anisotropic and non-homogeneous, and material data was largely unknown, simulations and calculations were difficult to perform.

5.4 Experiments and Validation

Several experiments and validation processes were carried out to demonstrate that the frame and associated parts were suitable for clinical use. These are outlined in the following section.

5.4.1 Pressure and Angle Sensor Measurements

A pressure/angle sensor was used as part of a method of determining pressures and orientations of the bolsters applied to the patient. The sensor units were mounted on the rods supporting the bolsters as shown in Figure 5-21.

5.4.1.1 Angle Measurements Accuracy and Reliability

To detect angle, accelerometers and gyroscopes were used. Figure 5-21 shows the axes of rotation for the angle sensor.

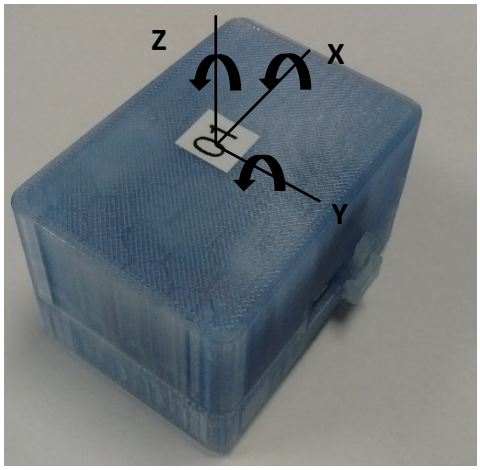

Figure 5-21. Axes of rotation of angle sensor

It is mounted with the X-axis pointed parallel to the bolster rod according to Figure 5-14. To test it, a device that allowed mounting of the sensors on a rotating protractor was used (Figure 5-22). It was oriented such that only a single axis of motion of the sensor unit was allowed for each test. The angle value was measured at interval of 20 degrees, in three repeated experiments from 0-360 degrees both clockwise and counterclockwise. Between these sets, the sensor was reset. This was repeated for each axis and then for all four sensor units. For the Z-axis, the protractor had to be tilted such that the gravitational force is not parallel to the axis, a requirement for the accelerometer to work. It was tilted to 22 degrees.

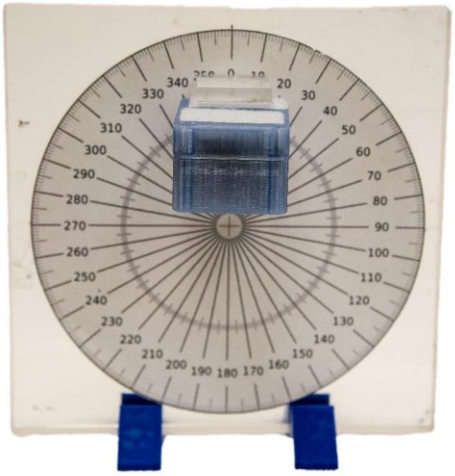

Figure 5-22. Rotating protractor with angle sensor attached

In the analysis, first the cyclic values were linearized by adding a multiple of 90 degrees to the measured reading. Then the sensor value was plotted against the calibration device measurement and linearity was checked, as shown for sensor 1 in Figure 5-23.

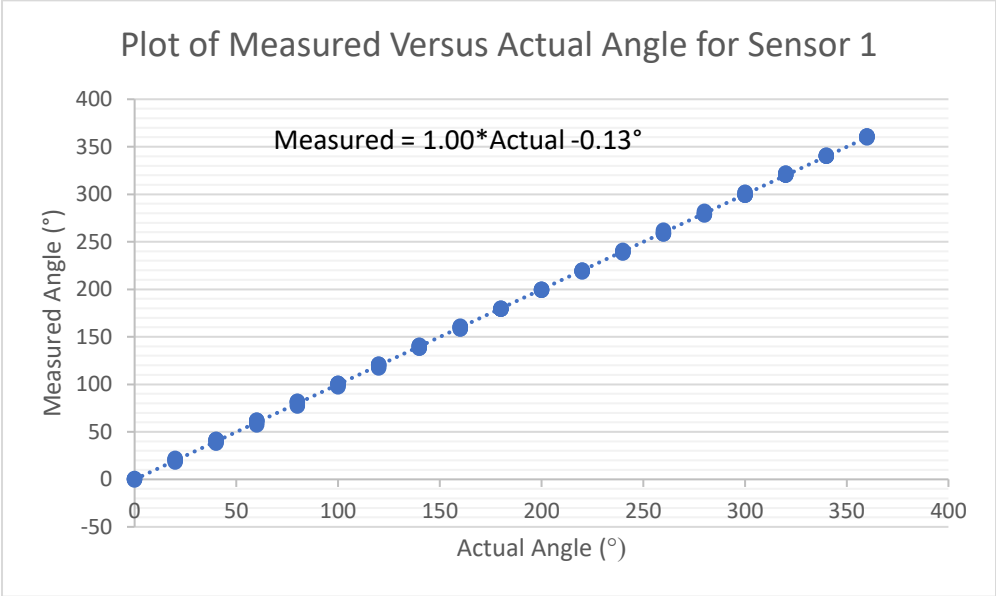

Figure 5-23. Plot of measured angle from sensor unit 1 versus actual angle from the protractor

A calibration offset was calculated for each axis of each sensor unit to minimize the maximum difference (Δ_{max}) between the sensor value minus the offset ("corrected difference") and the calibration protractor. Root mean square error (RMSE) was also calculated. The calibration figures are found in Table 5-1 for all four sensor units. R^2 ranges between 0.997 and 1.000, indicating excellent linearity for

all measures. For X and Y, offsets are between -1° and 1° with Δ_{max} only as high as 7°, while for Z, the offset has gone as large as -5.5° with Δ_{max} as high as 7°. RMSE was as high as 3.4°.

Table 5-1: Calibration results for angle sensors

Unit 1

R^2_{X1}	$Offset_{X1}$ (°)	$\Delta_{max\ X1}$ (°)	$RMSE_{X1}$ (°)
1.000	0	3	1.3
R^2_{Y1}	$Offset_{Y1}$ (°)	$\Delta_{max\ Y1}$ (°)	$RMSE_{Y1}$ (°)
1.000	0	5	1.8
R^2_{Z1}	$Offset_{Z1}$ (°)	$\Delta_{max\ Z1}$ (°)	$RMSE_{Z1}$ (°)
0.999	-3	7	2.7

Unit 2

R^2_{X2}	$Offset_{X2}$ (°)	$\Delta_{max\ X2}$ (°)	$RMSE_{X2}$ (°)
1.000	0	5	2.4
R^2_{Y2}	$Offset_{Y2}$ (°)	$\Delta_{max\ Y2}$ (°)	$RMSE_{Y2}$ (°)
0.999	1	7	3.3
R^2_{Z2}	$Offset_{Z2}$ (°)	$\Delta_{max\ Z2}$ (°)	$RMSE_{Z2}$ (°)
0.999	3.5	6.5	2.8

Unit 3

R^2_{X3}	$Offset_{X3}$ (°)	$\Delta_{max\ X3}$ (°)	$RMSE_{X3}$ (°)
1.000	0	2	1.4
R^2_{Y3}	$Offset_{Y3}$ (°)	$\Delta_{max\ Y3}$ (°)	$RMSE_{Y3}$ (°)
0.999	1	5	2.9
R^2_{Z3}	$Offset_{Z3}$ (°)	$\Delta_{max\ Z3}$ (°)	$RMSE_{Z3}$ (°)
0.999	-5.5	6.5	3.4

Unit 4

R^2_{X4}	$Offset_{X4}$ (°)	$\Delta_{max\ X4}$ (°)	$RMSE_{X4}$ (°)
1.000	-1	3	1.3
R^2_{Y4}	$Offset_{Y4}$ (°)	$\Delta_{max\ Y4}$ (°)	$RMSE_{Y4}$ (°)
1.000	1	3	1.2
R^2_{Z4}	$Offset_{Z4}$ (°)	$\Delta_{max\ Z4}$ (°)	$RMSE_{Z4}$ (°)
0.999	-2	7	2.8

5.4.1.2 Determination of the Accuracy and Reliability of Pressure Sensors

To test the pressure sensing system, an external pressure gauge was attached via a wye to the airbag. The pressure was inflated by 20 mmHg segments between 0 and 120 mmHg and then deflated by the same amount, and the pressure was recorded at each point according to the value on the gauge. The plot is shown in Figure 5-24.

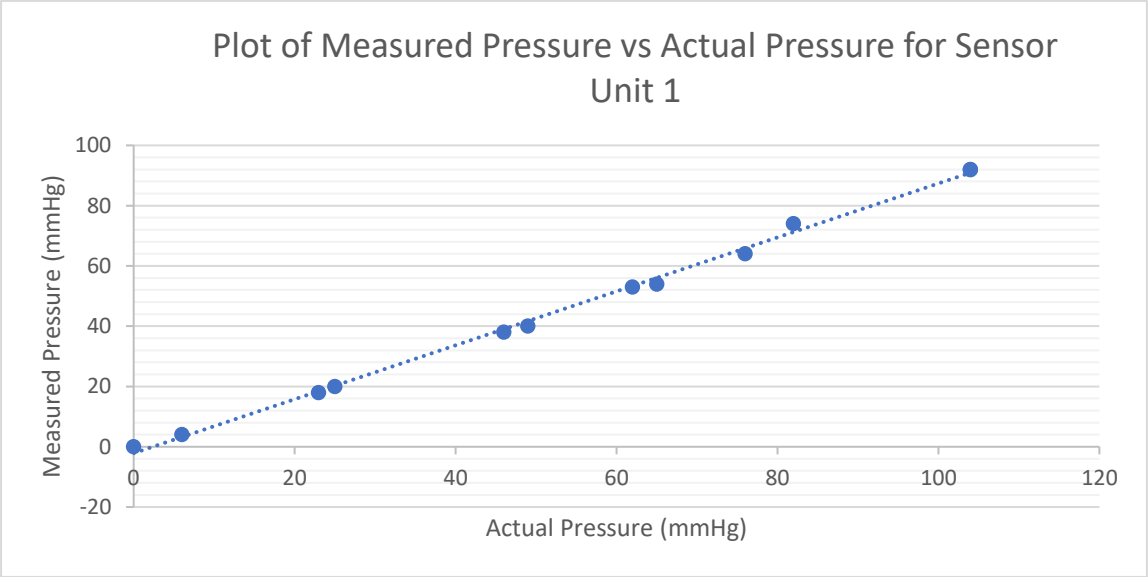

Figure 5-24. Plot of measured pressure versus actual pressure for sensor 1 to allow calibration.

A test offset was determined for each of the four units to minimize Δ_{max} between the sensor value minus the offset ("corrected difference") and the pressure gauge. RMSE was also calculated. The calibration figures are found in Table 5-2. R^2 ranges between 0.987 and 0.997, indicating excellent linearity for all measures. Offsets are between 4 mmHg and 6 mmHg with Δ_{max} ranging between 6 and 10 mmHg. RMSE ranged between 2.8 mmHg and 5.7 mmHg.

Table 5-2: Calibration results for airbags

R^2_1	$Offset_1$ (mmHg)	$\Delta_{max\ 1}$ (mmHg)	$RMSE_1$ (mmHg)
0.992	6	8	4.9
R^2_2	$Offset_2$ (mmHg)	$\Delta_{max\ 2}$ (mmHg)	$RMSE_2$ (mmHg)
0.987	4	10	4.8
R^2_3	$Offset_3$ (mmHg)	$\Delta_{max\ 3}$ (mmHg)	$RMSE_3$ (mmHg)
0.997	4	6	2.8
R^2_4	$Offset_4$ (mmHg)	$\Delta_{max\ 4}$ (mmHg)	$RMSE_4$ (mmHg)
0.990	5	10	5.7

5.4.1.3 Force Testing for Airbags

The objective of this experiment was to find a conversion factor between force and pressure, which is the contact area of the airbag. A simulation of in-brace correction at different pad forces and location during brace casting has been developed and described in chapter 6. This simulation provides a good tool for orthotists to predict the brace design results before actually doing the brace casting. Optimal pad force is the output of the simulation rather than the pressure. The pressure airbag system is practical for the orthotists because they tend to work in pressures instead of forces due to concerns about skin tolerance and comfort. Adding load cells to the system to measure the forces were prohibitively expensive. As the airbags used in the sensors are non-rigid and the contacts are not flat, the estimated contact area between the airbag and patient's surface is not straightforward to determine.

A load cell (Loadstar Sensors, Fremont, United States) was tested on each bolster one-by-one to determine the relationship between the applied force and contacted pressure. Figure 5-25 shows (a) the load cell mounted with the bolster and (b) a close-up of a load cell.

a b

Figure 5-25. a) mounting of load cell onto bolster support, and b) a load cell

The load cell uses 5 V power through a USB connection which connects to a data acquisition unit. The data acquisition unit then connects to a PC directly. The load cell housing is made of stainless steel and aluminum. It has a maximum load of 222 N and its accuracy is within 0.56 N [115]. It has a resolution of as low as 0.01 N, but this is adjustable in the manufacturer's software. For this experiment, the resolution was set to 1 N because of a more stable result. The forces measured from the load cell were plotted against the pressures obtained from the sensor unit at each setting. Based on equation 5-2, the resulting slope of the graph is equal to the contact area.

$$A = K\frac{F}{P} \tag{5-2}$$

where A is the contact area in mm^2, K is a constant relating Pa to mmHg (0.0075 mmHg/Pa), F is the force in N, and P is the pressure in mmHg.

The test was performed three times on different body models with different sizes to see how the contact area changes with body size. Two foam body-shaped torso models and one human volunteer was used, with frontal chest and waist measurements as shown in Table 5-3.

Table 5-3: Subject measurements for airbag calibration procedure

Subject	Chest Frontal Width (cm)	Waist Frontal Width (cm)
Volunteer	46	53
First foam torso	25	19
Second foam torso	19	19

As the trochanter and axilla bolsters are shaped the same, it was assumed that they would behave similarly. The lumbar and thoracic bolsters were tested at different angles around the postero-anterior axis to see the effect of the angle on contact area, at around 0°, 10° and 20°. This test also

served as a stress test, revealing whether the frame could support the required forces without failing. Pressures were tested at 40, 80 and 120 mmHg.

For the lumbar region, the effective average contact area was 2331 mm^2 and there was a strong correlation between chest circumference and effective area (R^2=0.82); for the axilla region, the average area was 2910 mm^2 and there was a moderate correlation (R^2=0.70); for the thoracic region, the average area was 2121 mm^2 there was a poor correlation (R^2=0.17). For the lumbar pad, valid for a waist frontal width between 19 and 53 cm, is Equation 5-3; for the thoracic pad with chest frontal width between 19 and 46 cm is Equation 5-4; and for the axilla pad with the chest frontal width between 19 and 30 cm is Equation 5-5.

Lumbar pad: Effective Contact Area = -38.0*Waist Width + 3481 (5-3)

Thoracic Pad: Effective Contact Area = -6.9*Chest Width + 2328 (5-4)

Axilla pad: Effective Contact Area = -46.6*Chest Width + 4307 (5-5)

In these equations, Effective Contact Area is the contact area between the pad and the body in mm^2, Waist Width is the frontal width of the waist in cm, and Chest Width is the frontal width of the chest in cm. The conversion factor has been built-into the equation to perform the unit conversion. Table 5-4 shows the calculated effective area and the average contact areas for the lumbar, axilla and thoracic bolsters.

Table 5-4: Effective Contact Area for Bolsters

Lumbar		Thoracic		Axilla	
Waist Frontal Width (cm)	Area (mm^2)	Chest Frontal Width (cm)	Area (mm^2)	Chest Frontal Width (cm)	Area (mm^2)
46	1471	53	1987	53	2130
19	2416	25	2261	25	3300
19	3105	19	2115	19	3300
	Average (mm^2)		Average (mm^2)		Average (mm^2)
	2331		2121		2910

Ultimately, the thoracic pad area can reasonably be represented using the average while Equations 5-3 and 5-5 can be used for the other two locations; in the thoracic equation the width coefficient is very small. For the dependence of area on angle, a linear regression was performed. For the lumbar section, R^2 was found to be 0.65 while for the thoracic section it was 0.94. To modify the

area to account for angle, Equation 5-6 (lumbar) and Equation 5-7 (thoracic) can be used, accurate for angles between 0 and 20 degrees:

$$\text{Lumbar Area} = (29.237*\text{Angle} + 1240.9)*(\text{Lumbar Area}_0/1471\ \text{mm}^2) \quad (5\text{-}6)$$

$$\text{Thoracic Area} = (-63.605*\text{Angle} + 2531.9)*(\text{Thoracic Area}_0/1987\ \text{mm}^2) \quad (5\text{-}7)$$

In these equations, Area is the contact area of the airbag in mm^2, Angle is the angle in degrees, and $Area_0$ is the angle calculated from Equations 5-31 and 5-5, in mm^2.

A method of determining pad contact area (and in turn, calculating force) was developed. Calculations can be performed by knowing the chest circumference, waist circumference, and pad angle to determine the effective contact area. This experiment also revealed that forces are much lower than originally expected, with the highest recorded force being only 67 N at a pressure of 120 mmHg compared to the estimated 128 N calculations suggested. This also served as a test of the frame's capabilities, showing that it could be adjusted appropriately and remain in place with force levels typical of casting.

5.4.2 Validity of the 3D frame Design in Laboratory Setting

To evaluate the durability of the 3D designed frame, laboratory tests were conducted to confirm that the frame could be strong enough to apply pressure to a healthy adult volunteer to induce a scoliotic curve in his spine and to determine the pressure distribution among the three pressure bolsters. It was assumed that if a spinal curve was able to be created with an uneven loading, scoliotic curves could be reduced. These tests used the steel collar clamp design (section 5.6). In the first test, the bolsters were positioned on T9 (thoracic pad) and T11 (lumbar pad) and L5 (trochanter pad). It was tested with all three bolsters at 30 mmHg, 60 mmHg and then 90 mmHg. In the second test, the importance of each pad was examined by testing each pad with different pressures. Only the lumbar and thoracic bolsters were applied in one test with both at 90 mmHg, and then the trochanter pad was added, again at 90 mmHg, and the effect of the trochanter pad was noted.

Figure 5-26 contains ultrasound measurements taken with all pad pressures at 30 mmHg (Figure 5-26 (a)), 60 mmHg (Figure 5-26 (b)) and 90 mmHg (Figure 5-26(c)). No visible curve developed until all 3 pressure bolsters applied 90 mmHg. The spinal curvature that induced was 12°.

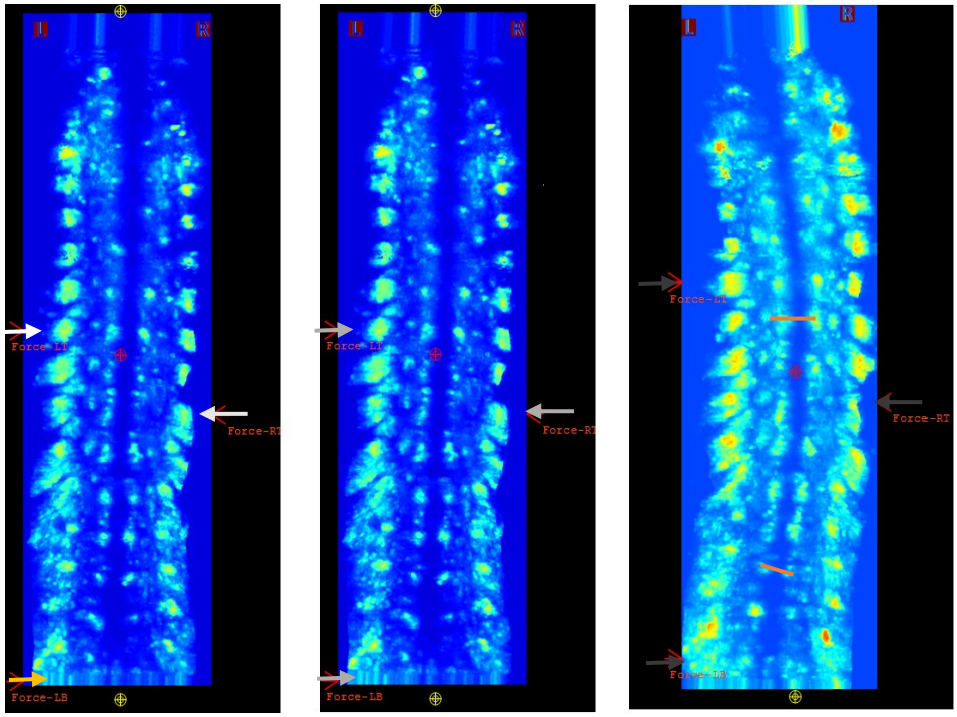

a) 30 mmHg b) 60 mmHg c) 90 mmHg

Figure 5-27. Ultrasound images of spine with all pad pressures set to a) 30 mmHg b) 60 mmHg and c) 90 mmHg

In the second test, it was found that having the lumbar and thoracic bolsters at 90 mmHg with no trochanter pad produced a 21° curve (Figure 5-28 (a)) while having all three bolsters at 90 mmHg yielded 15° (Figure 5-28 (b)), with the discrepancy in value being typical for separate readings. This was taken to suggest that the trochanter pad acts as a stabilizer instead of actively contributing to the curve modification.

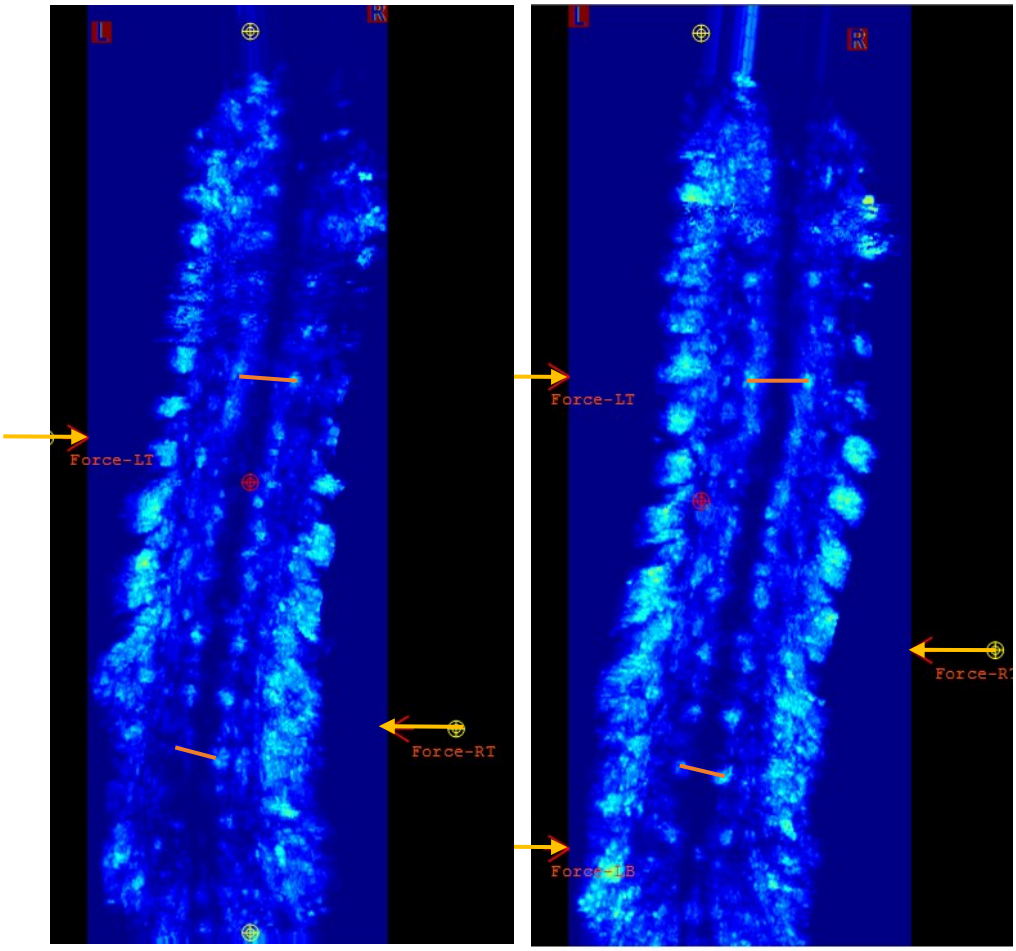

a b

Figure 5-28. a) test with thoracic and lumbar bolsters at 90 mmHg b) test with thoracic, lumbar and trochanter bolsters at 90 mmHg

The first test demonstrated that a scoliotic curve can be induced in a healthy adult male by the frame; this should indicate that the frame is suitable for reducing scoliosis curves in patients. The 90 mmHg pressure is on the high end which is to be expected as most of the patients are adolescent females.

The second test looked at which bolsters are important. It showed that the trochanter pad is essentially an anchor and the pressure at that point is not relevant; from a mechanical perspective, it's likely that any pressure on the trochanter is balanced by the positioning of the legs. In most simulations it is assumed that the pelvis is perfectly stable [116, 117, 118].

5.5 Preliminary Clinical Trial

5.5.1 Evaluation of the 3D Frame with Subject with AIS

The 3D brace frame was finally tested with a subject with adolescent idiopathic scoliosis. The subject did not consent to having their information published so clinical data is not presented here. After the subject donned a gown, she was instructed to stand in the middle of the frame. An ultrasound scan was taken. The simulated in-brace Cobb angle was reviewed by the orthotist; the correction was found to be inadequate. The orthotist made adjustments and a second ultrasound scan was then taken. The simulated in-brace correction was accepted by the orthotist. The subject was then instructed to step away from the frame. The subject was cast using the measurements taken on the frame, but not in the frame. Several functional issues were noted but most were readily solved. The lumbar and thoracic bolsters protruded too much into the frame's interior for the patient to comfortably enter; this was corrected by reversing the direction of the middle rotator. As this patient only verbally agreed to evaluate the frame, no written consent was signed. Her data measured in this experiment is not included. This experiment suggested that the design was complete and ready to be used by the orthotists for the entire casting process, not just for measurements.

After the orthotist was satisfied the durability and functionality of the frame, another subject with AIS was cast inside the frame. The patient's information is shown in Table 5-5. The subject's pre-brace radiograph is shown in Figure 5-28, with curve endpoints identified by black lines. It shows a single right thoracic curve with Cobb angle 29°. A prone side-bending flexibility bending test (Figure 5-29) was performed one month prior to the brace casting. The subject was instructed to bend to the right as much as possible, using the technique described in section 4.2.2. The curve hypercorrected from 29° to -19°, a correction of 183%, indicating that the spine was extremely flexible. The two black lines indicate the curve endpoints used to measure the corrected angle.

Table 5-5: Test subject information

Age (years)	12
Gender	Female
Curve Type	Right thoracic
Cobb Angle (°)	29
Upper end vertebra	T6
Lower end vertebra	L1
Risser sign	0
Thoracic apical AVR (°)	16.5
BMI (kg/m^2)	22.2
Bending Cobb angle (°)	-24
Flexibility (%)	183
Chest width (cm)	28
Waist width (cm)	27

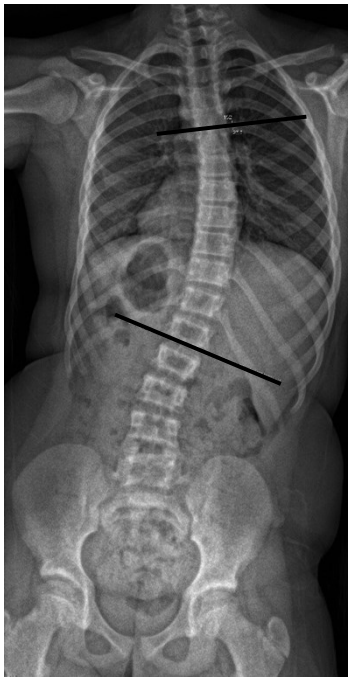

Figure 5-28. Radiograph taken at time of brace prescription for test subject

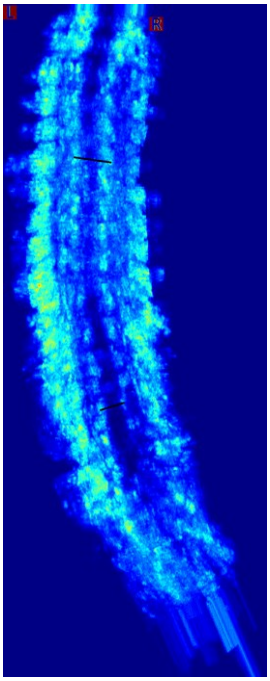

Figure 5-29. The right bending test ultrasound image. Black lines are centre-of-lamina measurements.

The patient stood in the frame and the bolsters were set in place for the first test, in a three-point pressure configuration because it is a single curve. It used an axilla bolster, a thoracic bolster, and a lumbar bolster. The bolsters were positioned with the axilla bolster pointing to the right at T6, the thoracic bolster pointing to the left at T10, and the inferior bolster pointing to the right at L2 (Figure 5-30).

Figure 5-30. Subject standing in frame

An ultrasound scan was taken to determine if the simulated in-brace correction was acceptable. The bolster pressures, locations and angles were recorded with sensor units, and the bolster forces were calculated using Equations 5-1 through 5-5. The results are found in Table 5-6. The ultrasound images are in Figure 5-31. The black lines in the ultrasound images are the centre-of-lamina measuring lines while the grey arrows indicate the location and direction of forces, with darker lines indicating higher forces. The test was performed three times with adjustments between the tests until acceptable results were found. The ultrasound image for Test 1 is in Figure 5-31 (a); the curve correction was 28%. The ultrasound image for Test 2 is shown in Figure 5-31 (b) with a correction of 38%. The ultrasound image for the third test Figure 5-31 (c) with 52% correction. Test 3 was deemed adequate. Test 3 had an axilla force of 24.5 N on T5, a thoracic force of 7.4 N on L1-L2 and a lumbar force of 5.5 N on L2.

Table 5-6: Test results for patient

	Test 1	Test 2	Test 3
Proxy Cobb angle (°)	21	18	14
Correction (%)	28	38	52
Axilla pad location	T6	T6	T5
Axilla pad area (mm^2)	2566	2566	2566
Axilla pad X angle (°)	-5	-5	-5
Axilla pad Y angle (°)	1	1	1
Axilla pad Z angle (°)	99	100	101
Axilla pad pressure (mmHg)	44.0	71.2	71.0
Axilla pad force (N)	15.1	24.4	24.3
Thoracic pad location	T10	T12	L1-L2
Thoracic pad area (mm^2)	2256	2256	2256
Thoracic pad X angle (°)	2	-15	-4
Thoracic pad Y angle (°)	6	6	6
Thoracic pad Z angle (°)	-98	-112	-128
Thoracic pad pressure (mmHg)	14.8	20.8	24.5
Thoracic pad force (N)	4.5	6.3	7.4
Lumbar pad location	L2	L3	L2
Lumbar pad area (mm2)	1151	1151	1112
Lumbar pad X angle (°)	2	2	7
Lumbar pad Y angle (°)	13	13	14
Lumbar pad Z angle (°)	-4	-21	-21
Lumbar pad pressure (mmHg)	13.4	27.3	37.4
Lumbar pad force (N)	2.1	4.2	5.5

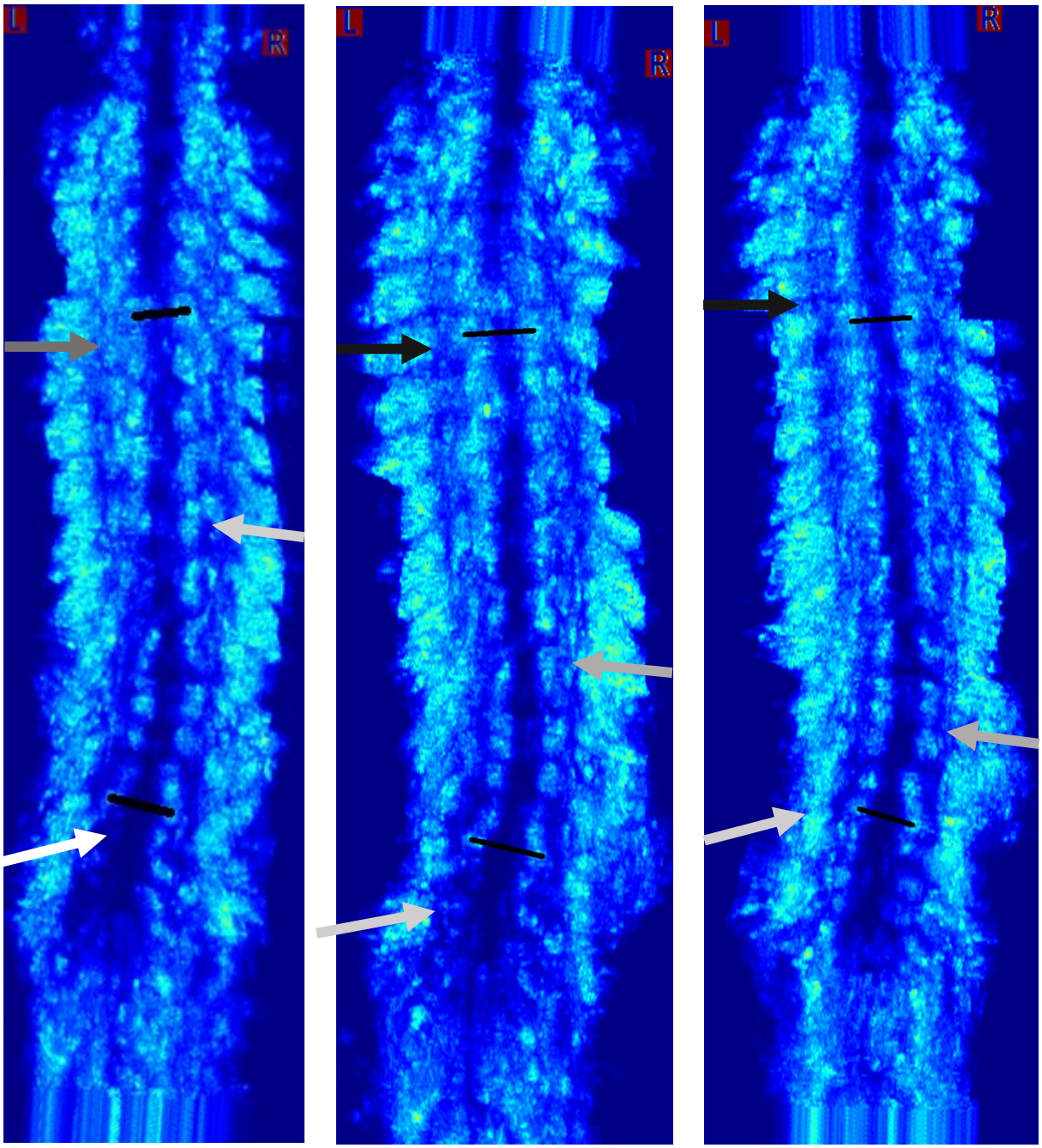

Figure 5-31. a) Test 1 ultrasound image b) Test 2 ultrasound image c) Test 3 ultrasound image

The bolsters were loosened and moved out to allow the patient to exit the frame for the wet plaster bandages to be applied. To cast the patient, the procedure in section 2.3.4.2 was followed. Plastic bags were placed over the bolsters to allow easier clean-up of the plaster. The patient re-entered the frame and the bolsters were returned to their Test 3 positions and approximate pressures, and the

plaster was allowed to harden. The patient exited the frame and the plaster was cut, and the plaster body mold was scanned by a handheld laser scanner.

The thoracic and lumbar forces appeared low but given the extreme 183% flexibility of the spine, it appears that the spine was flexible enough to correct sufficiently with low forces.

5.6 Conclusion

A new frame was designed and built to allow fully 3D casting of scoliosis. It was constructed of wood and, after several design revisions, off-shelf aluminum components to connect the frame and the bolsters. Attempts at using a 3D printer to produce the final product failed due to inadequate material properties. The final frame design was demonstrated to be able to initiate a scoliotic curve in a healthy subject and this was taken to imply that it could conversely correct a scoliotic curve in an AIS patient for casting. An angle and pressure measurement device was tested to show that it could accurately indicate the direction and pressure (and with a further experiment, force) of the bolster. Two volunteers were cast in the frame, thus demonstrating that it was suitable for clinical use. The measurement devices were important for allowing the 3D model implemented in chapter 6 to be applied to patients in the frame.

Chapter 6: Development of Simulation of Pad Placement for Use with Brace Casting Frame

6.0 Summary

In this chapter, a lumped body FEA simulation for brace casting is developed. The 3D casting frame has many degrees of freedom for the bolsters, both rotational and linear, which may lead to a slow casting process. The developed simulation is intended to streamline this process by giving a first guess for bolster placement. In section 6.1, a literature review of numerical simulation of scoliosis bracing is reported. The motivation for developing this simulation is described in section 6.2. In section 6.3, the methods for developing the simulation are outlined, explaining a method for using a PA radiograph and spinal flexibility information to output an optimized brace casting bolster location, using MATLAB. In section 6.4, a pilot study with 16 subjects was performed. Of those 16, 5 were removed so the simulation was applied to 11 subjects' records and comparing the predicted results with actual in-brace correction. This section also applied a clinical data set from a patient who was cast in the frame to investigate if the simulation replicates reality. The discussion is found in section 6.5 and the chapter is concluded in section 6.6.

6.1 Literature Review of Numerical Simulation of Scoliosis Bracing

In section 2.4, FEA and its application to scoliosis brace simulation was reported briefly. In FEA simulations of scoliosis, the spine and ribcage and, recently, the entire torso including soft tissue are modeled. The soft tissue, bony tissue and brace are constructed separately using small deformable elements (finite elements) with material properties selected to match their types. The use of small deformable elements simplifies the math from partial differential equations to algebraic equations which are close approximations. The algebraic equations involve stiffness, force and displacement values, and can be assembled into a large system of equations which can be solved to determine displacements.

There have been several FEA studies of scoliosis bracing, many of them led by Aubin et al. [6, 119, 120, 121]. Typically, muscle forces and gravity are ignored, but in a study by Clin et al., 2010, in Aubin's group, gravity is included in the simulation [121]. These studies attempt to determine optimal

brace characteristics. These studies usually indicate less correction than that found in actual clinical practice, but the paper by Clin et al. incorporating gravity claimed an in accuracy of only one degree compared to clinical results [121].

In addition, there have been lumped body simulations which treat the vertebrae as rigid bodies and spinal joints as torsional springs, including that by Petit et al., 2004, again in Aubin's group [122]. This study attempted to use side-bending flexibility measurements to improve estimations of joint stiffness, starting with values taken from cadaver tests. These joints included the intervertebral disc, the facet joints, the soft tissue connecting the vertebrae, and for the thoracic region, the proximal part of the ribs. The simulated spine had a coronal force applied to displace T1 relative to L5 to the same displacement found in the bending test. Then the stiffness of the joints was modified using a multiplier until the curve magnitudes in the simulation matched the curve magnitudes in the bending test. This study was somewhat weakened by the need for lateral radiographs and registration, and it did not attempt to produce a clinically useful result but yielded an improved method for analysis.

6.2 Motivation

The 3D brace casting frame described in chapter 5 has 16 continuous DOF for movement over four bolsters. For comparison, the Providence Casting System has, over four brace bolsters, four continuous DOF in the medio-lateral direction as well as four discrete DOF in the inferior-superior direction (in the form of a 1" grid), for a total of 8 DOF. They both have continuous force allowances. Between these motion DOF and force allowances, adjusting the Providence Casting System to yield an optimal position and force combination for each of the four bolsters is difficult. The goal of the simulation reported in this chapter is to procedurally produce an initial guess of bolsters' positioning and applied force at each bolster starting on the coronal plane with linear degrees of freedom. After the orthotist tries the initial setting, the bolsters' positions and forces can be adjusted based on the orthotist's experience and the information obtains from the 3D ultrasound system.

6.3 Simulation Model and Method

A FEA-type program was developed in MATLAB. MATLAB was chosen because it is versatile and well-suited to solving matrix problems. The flowchart for this simulation is shown in Figure 6-1.

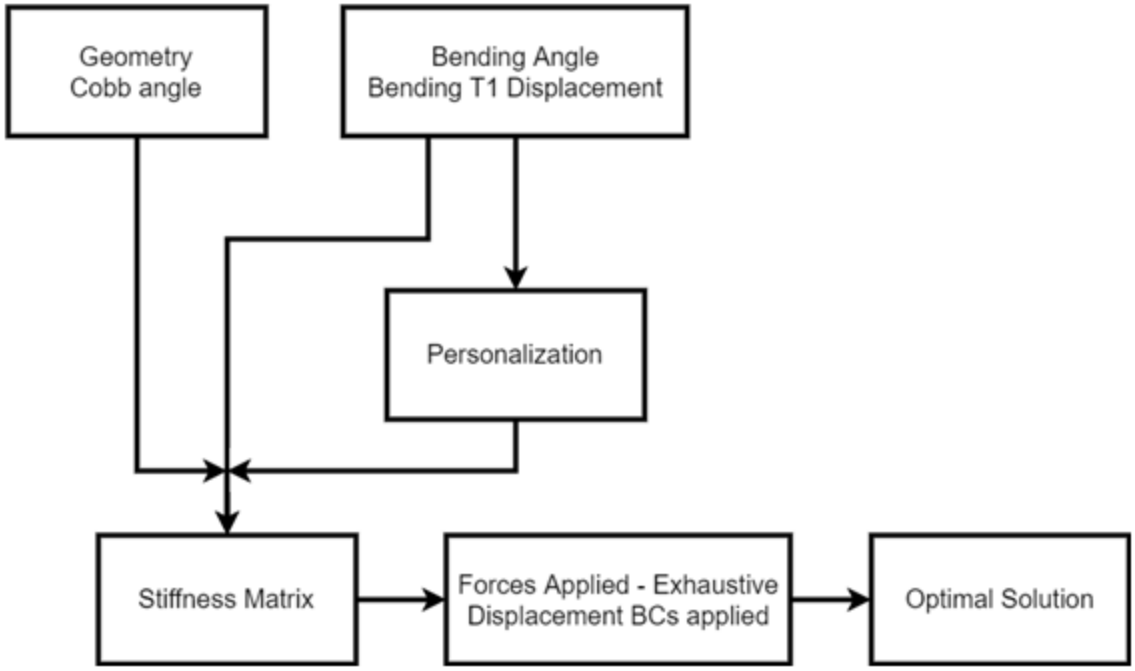

Figure 6-1. Simulation Flowchart

6.3.1 Subjects for Model Development and Validation

Sixteen subjects who met the following requirements were extracted from the Edmonton Scoliosis Medical Record. The inclusion criteria were subjects who a) were diagnosed with adolescent idiopathic scoliosis, b) were prescribed a full time TLSO, c) had PA pre-brace radiographs, d) had at least one bending test performed with an ultrasound scan, and e) had an in-brace PA radiograph. Of 16 patients considered, four were eliminated because there was no measurement scale on the in-brace correction radiograph and one was eliminated because the patient's in-brace correction radiograph was in the supine position. Two bending tests were required to calculate the spinal stiffness and three only had one bending ultrasound.

Among the eleven remaining subjects (10F, 1M), the average age was 13.7±1.5 years old. Eight subjects had double curves and 3 had single curves. The average initial thoracic Cobb angle was 23.4±14.3° while the average thoracolumbar-lumbar (TLL) Cobb angle was 30.5±11.7°. Table 6-1 shows the demographic and curve information for the eleven subjects. The curves were classified into two types based on apex of the curve, corresponding roughly to thoracic and thoracolumbar/lumbar curves.

Thoracic curves were all to the right while TLL curves were all to the left. Regardless of whether the curves are structural or not, they were all considered equivalently in this simulation.

Table 6-1: Demographic and curve information for the eleven included subjects

Subject	Age	Pre-Brace Thoracic Curve Cobb Angle (°)	Pre-Brace TLL Curve Cobb Angle (°)	Sex
1	12	13	12	F
1	12	13	25	F
2	16	44	42	F
3	13	24	38	F
4	13	0	43	F
5	13	21	27	F
6	13	0	33	F
7	14	29	37	F
8	16	34	30	M
9	14	39	33	F
10	13	24	28	F
11	12	29	0	F

6.3.1 Geometry of the Spine

As shown on Figure 6-1, the first step of the simulation is to obtain the geometry of the spine. The coordinate directions used to describe the geometry are shown in Figure 6-2 [123].

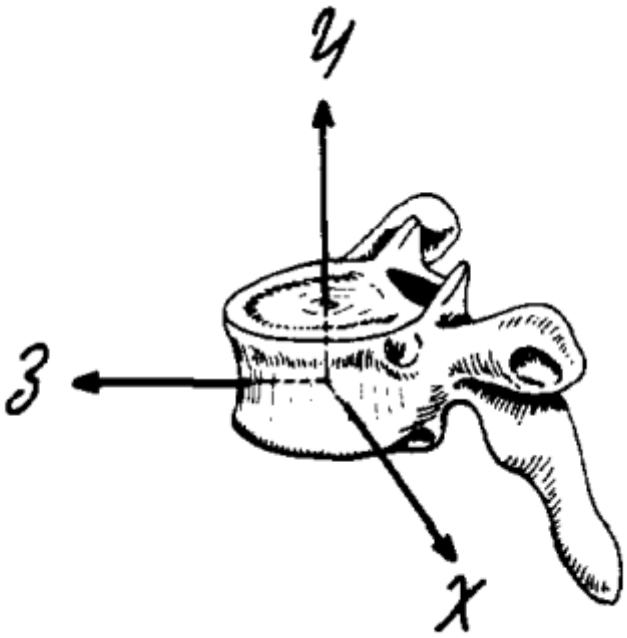

Figure 6-2. Coordinate system used [123]

To extract the geometry, a standing PA radiograph was used. A measurement scale was required on the radiograph to determine the positions of geometric data. ImageJ (NIH, USA), an image analysis program, was used to measure the geometry using the multi-point tool. To perform the geometry extraction (Figure 6-3), 73 points were marked. The first two points were placed on the measurement scale two centimetres apart to provide a scale. The third point was put in the bottom right corner of the PA radiograph to allow the vertical coordinate to be flipped so the coordinate increases superiorly. One point was placed on the top of each iliac crest. Four points were placed on each corner of individual IVD, starting with the IVD between L4 and L5, in a clockwise manner starting from the bottom right of each IVD. The last four points are placed on the IVD between T1 and T2. The geometric measurements were taken and then exported into a comma separated value (.CSV) format and imported into a MATLAB program. Using these coordinates, the program determines the center positions of all vertebral body. It also determines the position of the IVD centres and the height of the joints, used in determining displacements from rotations. The geometry extraction is shown in Figure 6-3.

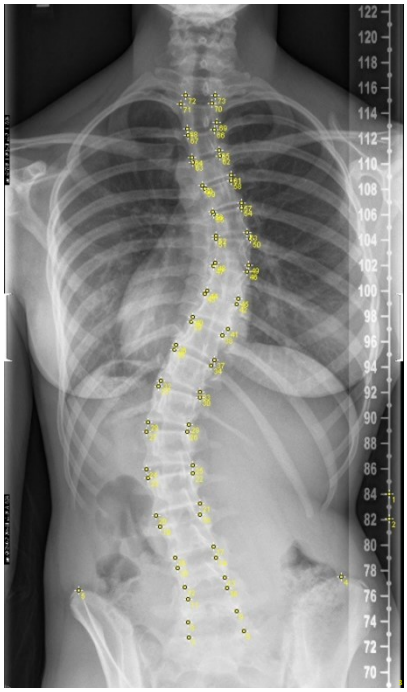

Figure 6-3. The AP radiograph shows the 73 points for the geometry extraction

In-brace radiographs were used to determine the spinal correction from a brace for comparison. The in-brace spinal geometry was generated in the same way.

Only the coronal view was considered in this version of the design. AVR should be included in the future because there is coupling between the transverse and coronal planes [123].

6.3.2 Mechanical Properties of the Spine

The vertebrae were assumed to be perfectly rigid while the intervertebral joints (IVJ) were expected to account for almost all of the movement. The elastic modulus of the intervertebral disc under compression is about 17 MPa [124] while ligaments have an elastic modulus between 3.5 and 28.2 MPa [125], and the elastic modulus of vertebral bone is about 17 GPa [126]. The displacement of the soft tissue IVJ was expected to be several hundred times greater than that of the vertebrae, therefore rendering the vertebral body deformation negligible. The IVJs were assumed to have small displacements so they were treated as linearly elastic. This assumption means that gravity is implicitly accounted for in the simulation as the patients were standing in both the radiograph used for extracting geometry and within the brace casting frame.

The IVJ were modeled as hinge joints with torsional springs as it was assumed that rotational effects would be dominant over shear effects. The stiffness around the X-axis before the personalization procedure is found in Table 6-2 [122]. It assumes a linear stress-strain relationship.

Table 6-2: Pre-personalization stiffnesses [122]

K (N-cm/rad)	Level
640	T1-T2
970	T2-T3
950	T3-T4
1,140	T4-T5
990	T5-T6
1,100	T6-T7
1,970	T7-T8
1,220	T8-T9
1,430	T9-T10
2,390	T10-T11
1,220	T11-T12
1,580	T12-L1
1,870	L1-L2
1,910	L2-L3
1,350	L3-L4
2,100	L4-L5

6.3.2.1 Personalization of Simulation to Specific Patients

The stiffnesses were personalized using the method outlined in Petit et al. [122], generating a stiffness matrix as is partially shown in Table 6-3 with stiffness values in N-cm/rad. It was constructed using FEA methods, modeling each vertebral body as a rigid body with a rotational spring on each side. Two stiffness coefficients were calculated, one for the lumbar section (α_L) and one for the thoracic section (α_T). To retrieve the final stiffness, the values found in Table 6-1 are multiplied by the applicable α; T12-L1 used α_L. Left and right side-bending ultrasound images were taken using the method found in Zheng et al, 2017 [7]. To perform this calculation, the lateral displacement of T1 relative to L5 was

measured for both the right and left bending tests. The angles of the left curve, in the left bending test, and the right curve, in the right bending test, were measured. Assuming α_L and α_T were both 1.00, a force was applied to T1 until the displacement of T1 matched the bending test. α_L and α_T were then modified until the curve angles matched the bending test.

Table 6-3. First three segments of stiffness matrix **K** (N-cm/rad)

K	L4-L5	L3-L4	L2-L3
L4-L5	α_L*640+α_L*970	-α_L*970	0
L3-L4	-α_L*970	α_L*970+α_L*950	-α_L*950
L2-L3	0	-α_L*950	α_L*950+α_L*1140

6.3.2.2 Beam Bending Model

Braces produce forces largely normal to the spine while this simulation only incorporates bending moments. To generate bending moments from horizontal forces, the spine was modeled as a beam, fixed in all directions at L5 with a reaction force and moment at T1 to produce an equilibrium system. A general free body diagram is shown in Figure 6-4. This process assumes that the spine is long and narrow and that the spine is significantly more important to the structure of the torso than the soft, non-spinal tissue (soft tissue making up the vertebral column is included) and distal ribs (the proximal ribs are included in the model).

The trochanter bolster is not explicitly modeled, as in section 5.4.2 it was demonstrated that the magnitude of its force is not important. The trochanter bolster simply acts as a stabilizing reaction force and its function is essentially included by fixing L5.

Three horizontal forces, in addition to the reaction force, were used, representing the bolsters. The forces were applied as point forces at a single vertebral body for simplicity, but the forces at the spine would be more spread out.

Positive force values are those pointing to the left and positive moment values are counterclockwise.

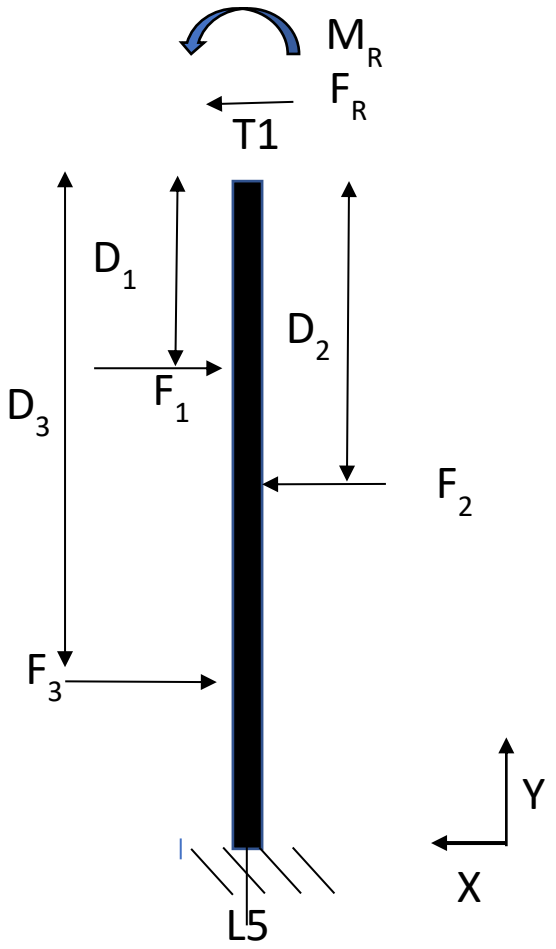

Figure 6-4. Model schematic

In Figure 6-4, M_R is the boundary condition moment at T1, F_R is the boundary condition shear force at T1, F_1 is the superior shear force, D_1 is the distance from T1 to the superior shear force, F_2 is the middle shear force, D_2 is the distance from T1 to the middle shear force, F_3 is the inferior shear force and D_3 is the distance from T1 to the inferior shear force.

Using this diagram, the reaction moment is found by Equation 6-1:

$$M_R=F_3*D_3-F_2*D_2+F_1*D_1 \quad (6\text{-}1)$$

The reaction shear is determined by Equation 6-2:

$$F_R=F_1-F_2+F_3 \quad (6\text{-}2)$$

A general bending moment diagram is shown in Figure 6-5.

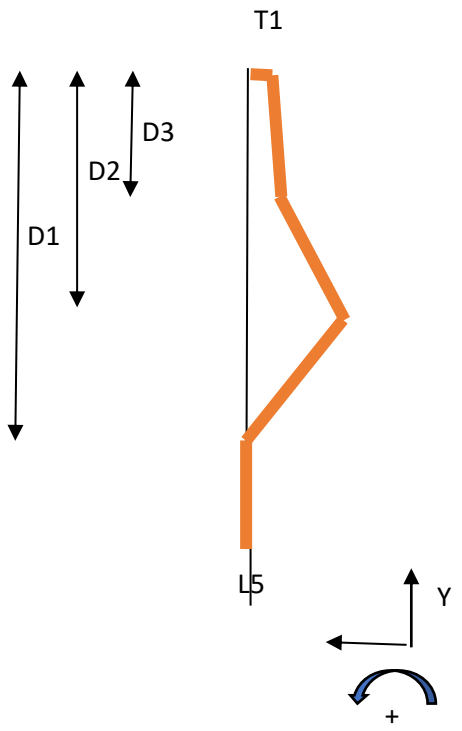

Figure 6-5. Bending moment diagram for beam model of spine

The slope between each set of points is the shear force present at each section. Integrating between points yields the moment.

The Cobb angles were not calculated directly as the orientation of the vertebral body end plates is relatively difficult to calculate. The Ferguson angle is the angle between the vertebral body centres of the superior bound, apex and inferior bound. The Cobb angle was calculated by multiplying the Ferguson angle by 1.35 [127], Equation 6-3:

$$Cobb = 1.35 \times Ferguson \quad (6\text{-}3)$$

This correlates with Cobb angle at R^2=0.98.

6.3.3 Analysis Method

To produce the correction, the vertebral bodies were rotated in the coronal plane due to the applied forces. The rotational displacement that was found was used to translate the centroids by rotating the vector from the centre of the vertebra below the disc to the vertebra above the disc using a rotation matrix. This process started at L4 and proceeded upwards until all vertebrae up to T1 were translated. The rotations were found using the system of simultaneous equations, Equation 6-4:

$$R = inverse(K) \times M \quad (6\text{-}4)$$

In equation 6-4, **R** is the 16x1 column vector of the IVJ rotations (rad), **M** is the 16x1 column vector holding bending moment acting at each joint (N-cm) and **K** is the 16x16 stiffness matrix (N-cm/rad).

The moment vector **M** was found by determining the moment at each IVJ using the bending moment calculation in section 6.3.2.

After the personalization and generation of the stiffness matrix, the optimization process for the bolsters began. It was iterated in five steps with progressively smaller force variations. The simulation used an exhaustive approach for determining bolster locations and force magnitudes. All combinations of allowable position and force level were combined into a matrix of moments with 16 rows and 15,625,000 columns. This corresponds to three positions each with ten possible values and three forces with 25 possible values each. The 16 rows contain the calculated moment at each IVJ. The bolsters were limited to the vertebral body centroids. Two of the pad positions ranged between L4 and T6 and one could range between L3 and T5. T5 was chosen as the upper limit because that is approximately the level of an axilla pad.

Five iterations were performed using successively tighter force intervals in order to produce a more accurate result. In the first iteration, the forces ranged between -70 N and +70 N with 28 N steps. Following iterations are centred on the optimal value found in the previous iteration with a smaller range than the previous one. Each iteration reduces the range by 14 N on each side. Forces were limited to be between [-70, 70] N. For example, if the first iteration suggested 35 N as the optimal value, the second iteration will be between -21 N and 70 N (35 N – 4 * 14 N = -21 N) and 70 N (35 N + 4 * 14 N = 91 N, which is reduced to 70 N due to that being the highest allowable value).

The naïve method for determining the quality of the simulation is simply minimizing the Ferguson angle. When trying to minimize Ferguson angle, the simulation tended to produce curves that were straight between the end points chosen from the pre-brace radiograph, but not vertical, as seen in Figure 6-6(b). The “deviation criterion” was also tried: it is the sum of the absolute value of the lateral deviation of the vertebral body centres from the line in the postero-anterior radiograph between T1 to L5. It was noted that the braces used in this research did not align T1 vertically with L5 but rather have T1 in approximately the same horizontal position as in the unbraced postero-anterior radiograph, so that position was decided on as the goal. Figure 6-6 shows three curves for patient 1: a) is the unmodified starting curve; b) is the Ferguson-corrected curve; and c) is the deviation-corrected curve. The endpoints used were vertebrae L4 and T11 for the lumbar, and T11 and T7 for the thoracic curve.

The Ferguson corrected curve is straight in the thoracic region but highly bent in the lumbar region, yielding a poor result for practical uses but a low value as far as the simulation can tell. The deviation-corrected curve is an improvement over the uncorrected and Ferguson-corrected approaches.

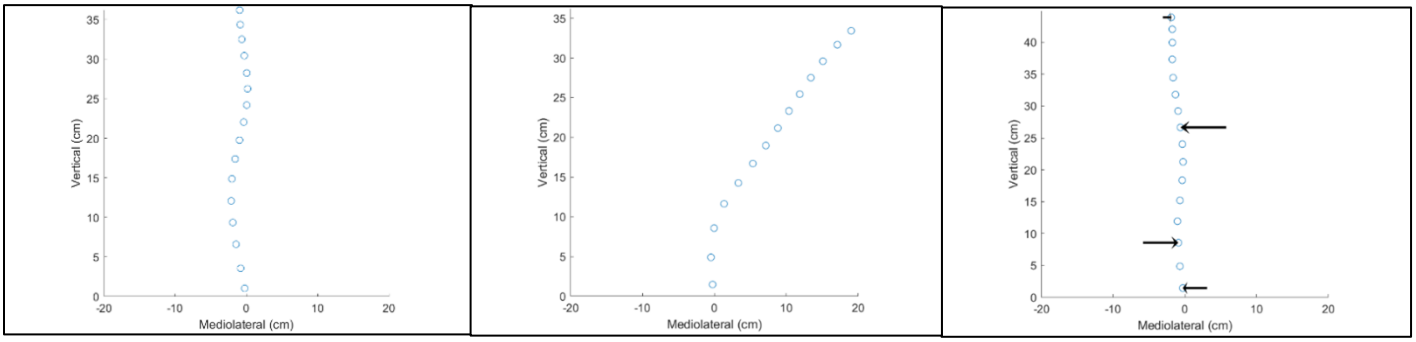

a b c

Figure 6-6. a) initial curve; b) Ferguson-corrected curve; c) deviation-corrected curve

As a result, the deviation criterion was decided upon. After using this deviation to minimize the curve, the Ferguson angle was determined, and the Cobb angle was calculated.

6.4 Results of Simulation and Comparison to In-Brace Results

The simulation took approximately 5 minutes on a personal computer using a dual core i5-6200 with 8 GB of RAM. The simulation results for the eleven patients with thoracic curves are shown in Tables 6-4 and those with thoracolumbar-lumbar curves are shown in table 6-5.

Table 6-4: Overall results for the simulation process in the thoracic region

Patient	Initial Thoracic Curve Cobb (°)	Simulation Thoracic Cobb (°)	Simulation Thoracic Curve Correction (%)	In-Brace Thoracic Curve Cobb (°)	In-Brace Thoracic Curve Correction (%)
1	13	9	33	8	38
2	44	38	14	26	41
3	24	22	9	8	67
4	No curve	N/A	N/A	N/A	N/A
5	44	24	45	26	41
6	No curve	N/A	N/A	N/A	N/A
7	29	16	44	16	45
8	34	39	-15	36	-6
9	39	28	29	31	21
10	24	18	23	13	46
11	29	4	87	15	48
Average±SD	31.1±10.3	22.0±11.9	30.0±28.4	19.9±10.2	38.0±20.3

Table 6-5. Overall results for the simulation process in the thoracolumbar and lumbar regions

Patient	Initial TLL Curve Cobb (°)	Simulation TLL Cobb (°)	Simulated TLL Curve Correction (%)	TLL Curve In-Brace Cobb (°)	TLL Curve In-Brace Correction (%)
1	25	12	51	5	80
2	42	27	37	21	50
3	38	34	11	23	39
4	43	35	18	16	63
5	27	25	8	21	22
6	33	29	12	7	79
7	37	17	53	17	54
8	30	19	36	26	13
9	33	19	43	16	52
10	28	13	55	13	89
11	No curve	N/A	N/A	N/A	N/A
Average±SD	30.5±11.7	20.9±10.5	29.4±20.3	15.0±8.1	46.0±25.4

The actual in-brace correction in terms of Cobb angle exceeded simulated corrections by an average factor of 1.46, combining thoracic and TLL curves.

Table 6-6 shows the results using the summation of lateral deviation correction criteria.

Table 6-6. Deviation correction

Patient	Initial Deviation Condition (cm)	Simulated Deviation Condition (cm)	Simulated Change (cm)	In-Brace Deviation Condition (cm)	In-Brace Change (cm)
1	11	5	6	8	3
2	25	14	10	11	14
3	16	13	3	13	3
4	38	30	8	10	28
5	14	9	5	10	4
6	33	18	15	8	25
7	20	11	9	11	10
8	26	11	15	15	12
9	20	10	10	12	8
10	13	7	5	4	8
11	38	12	26	35	3
Average±SD	23±10	13±7	10±6	12±8	11±9

Using the deviation correction criterion, they were much closer: on average, the in-brace value is only 1 cm better than the simulated value, a ratio of 1.1.

Table 6-7 contains the stiffness coefficients that were found.

Table 6-7. Stiffness coefficients associated with each patient

Patient	Lumbar Alpha	Thoracic Alpha
1	0.10	4.38
2	0.10	1.10
3	0.10	1.10
4	1.09	1.00
5	0.15	1.10
6	1.09	1.00
7	0.10	1.11
8	10.00	1.09
9	0.10	1.10
10	0.20	1.10
11	1.00	1.09
	1.28±2.92	1.38±1

Table 6-8 contains the pad locations corresponding to the optimal value, determined using the deviation criterion method as explained in section 6.3.3. A lumbar pad at L4 resulted in all cases. Three- and four-point bending systems tended to result. In some cases, two forces are close to each other (patients 4 and 11) or coincident (patient 8), making essentially one point for a bending system with a higher-than-allowed force.

Table 6-8. Pad locations and forces

Patient	Reaction Force (N)	Bottom Force (N)	Bottom Force Location	Middle Force (N)	Middle Force Location	Top Force (N)	Top Force Location
1	-26	28	L4	-58	L2	56	T9
2	-44	44	L4	-70	L2	70	T7
3	6	13	L4	-11	L2	-8	T6
4	13	13	L4	-12	T11	-11	T12
5	-26	38	L4	-66	L2	54	T8
6	-4	32	L4	-70	T12	42	T6
7	-31	41	L4	-70	L2	60	T8
8	-47	-58	L4	64	T12	42	T12
9	-48	46	L4	-68	L3	70	T8
10	-43	36	L4	-61	L2	68	T7
11	-66	-70	L4	67	T12	69	T11
Average±SD	-29±25	15±41		-32±53		46±30	

Figure 6-7 through Figure 6-9 contains the curves for subjects 1-3. The remaining 8 subjects are found in Appendix A. These are PA views of the spine in a) initial radiograph; b) actual initial position; c) simulated corrected position; and d) actual in-brace position. The circular dots correspond to the centre of the vertebral body. The lowest circle corresponds to L4. The black arrows indicate the position and magnitude of the forces.

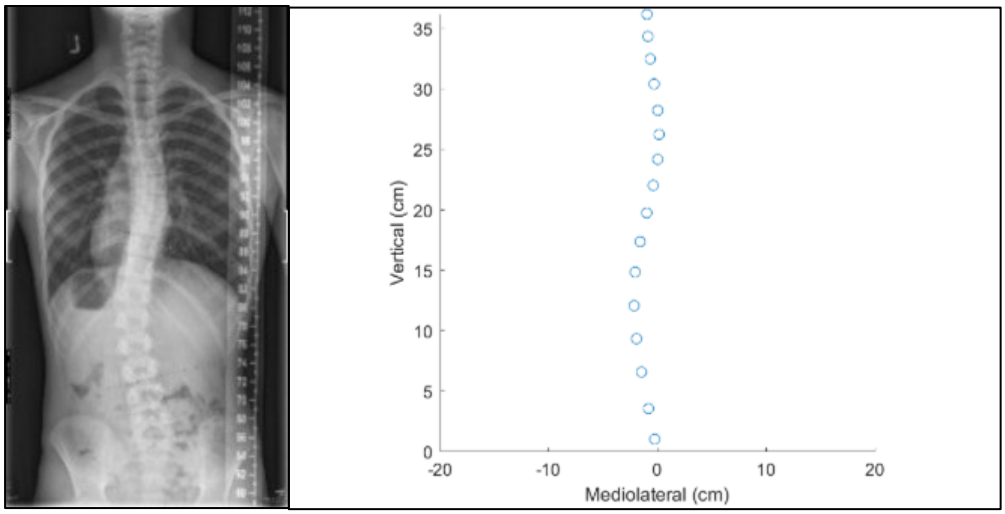

a b

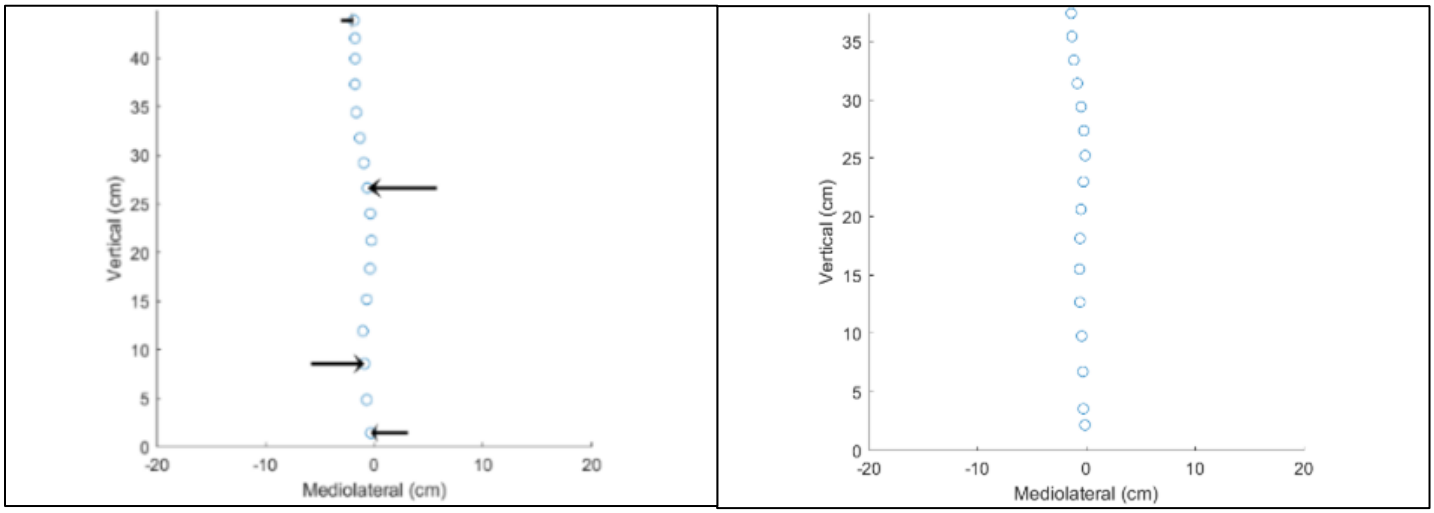

c d

Figure 6-7. Subject 1. a) postero-anterior radiograph a 13° right thoracic curve and 25° left thoracolumbar-lumbar curve, b) the extracted geometry plot with a thoracic Cobb angle of 25° and a thoracolumbar-lumbar Cobb angle of 35°, c) the simulated results of the optimized plot with a thoracic Cobb angle of 9° and a thoracolumbar-lumbar Cobb angle of 12° and d) the actual in-brace radiograph with a thoracic Cobb angle of 8° and a thoracolumbar-lumbar Cobb angle of 5. The patient's deviation criterion improved by 55%.

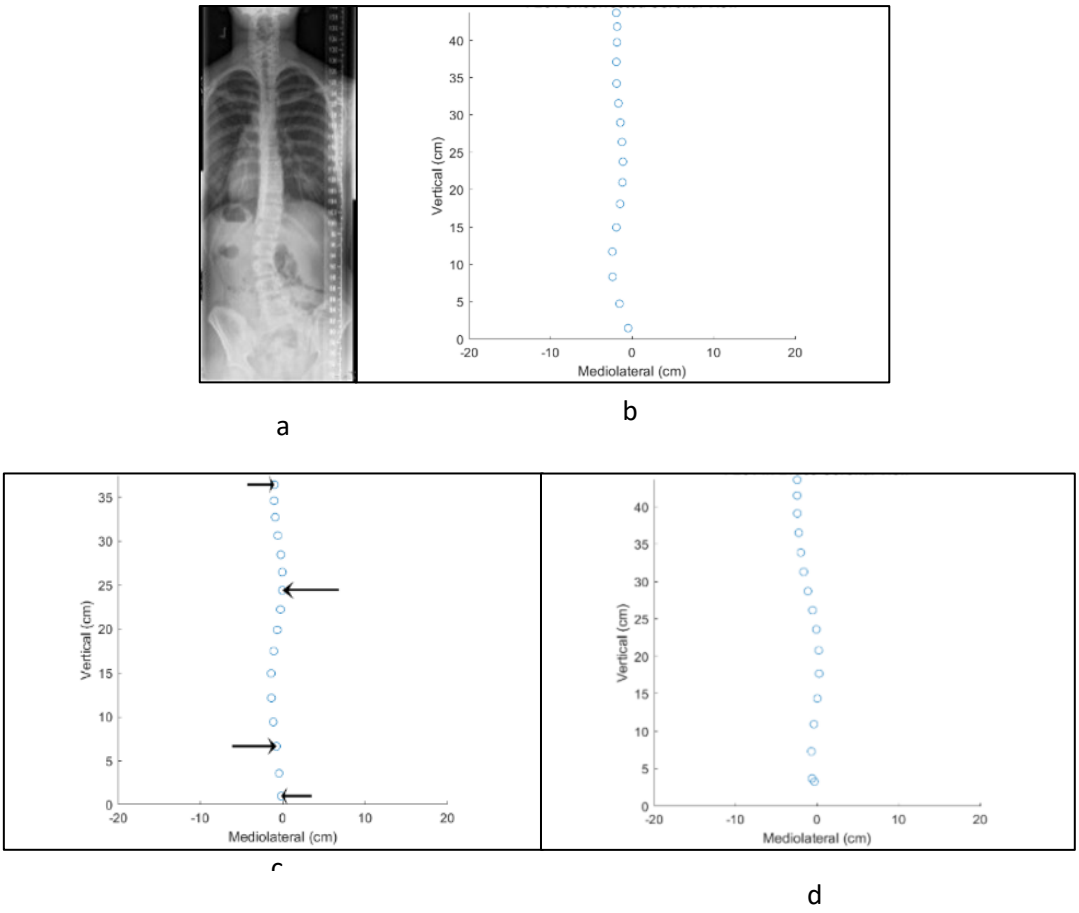

Figure 6-8. Subject 2. a) postero-anterior radiograph a 44° right thoracic curve and 42° left thoracolumbar-lumbar curve, b) the extracted geometry plot with a thoracic Cobb angle of 23° and a thoracolumbar-lumbar Cobb angle of 35°, c) the simulated results of the optimized plot with a thoracic Cobb angle of 38° and a thoracolumbar-lumbar Cobb angle of 27° and d) the actual in-brace radiograph with a thoracic Cobb angle of 26° and a thoracolumbar-lumbar Cobb angle of 21°. The patient's deviation criterion improved by 40%.

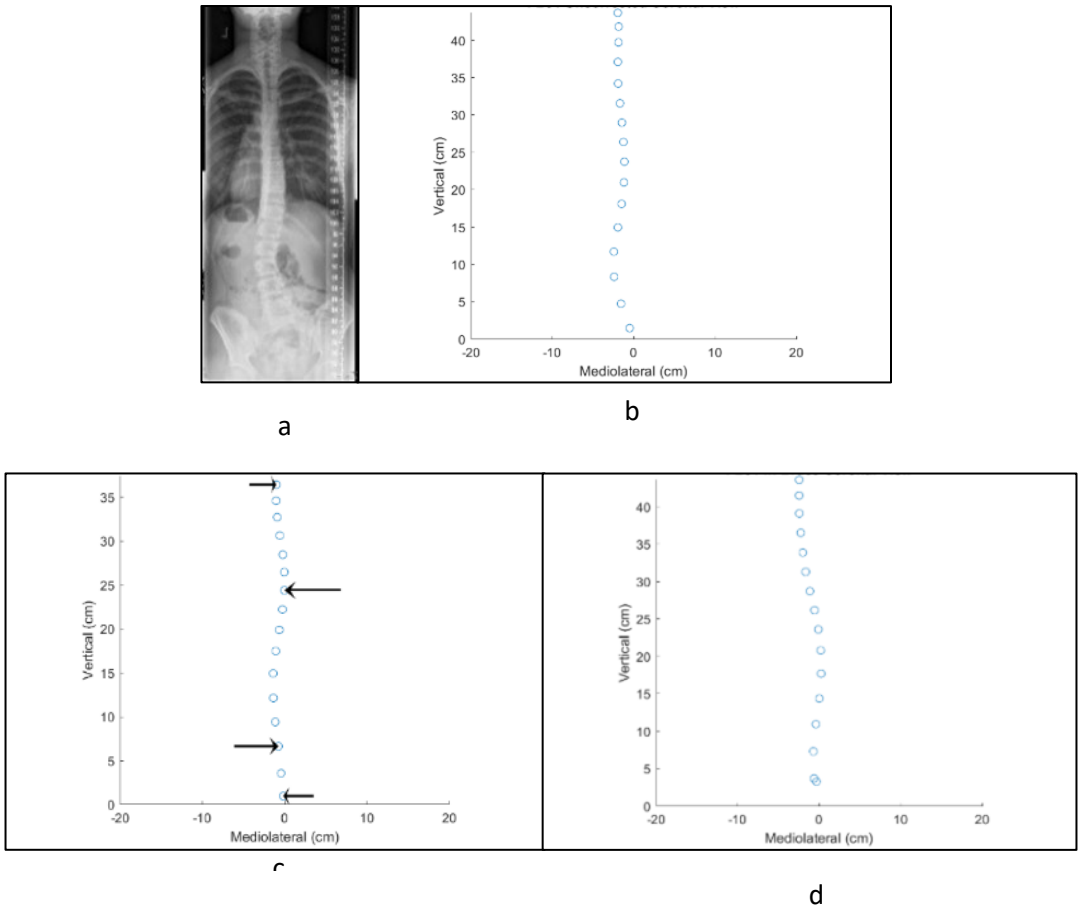

Figure 6-9. Subject 3. a) postero-anterior radiograph a 24° right thoracic curve and 38° left thoracolumbar-lumbar curve, b) the extracted geometry plot with a thoracic Cobb angle of 31° and a thoracolumbar-lumbar Cobb angle of 45°, c) the simulated results of the optimized plot with a thoracic Cobb angle of 22° and a thoracolumbar-lumbar Cobb angle of 34° and d) the actual in-brace radiograph with a thoracic Cobb angle of 8° and a thoracolumbar-lumbar Cobb angle of 23°. The patient's deviation criterion improved by 40%.

6.4.2 Accuracy of Geometry Acquisition

The extracted geometry was compared to the radiographic measurements. The Cobb angle was used as the comparison value. Table 6-9 contains the Cobb values calculated from the program versus those measured from radiographs. Figure 6-10 contains the plot comparing calculated and radiographic values. A coefficient of determination of 0.50 was found. The average difference between the radiographic thoracic Cobb and the extracted geometry's thoracic Cobb was 1°. The average difference between the radiographic lumbar Cobb and the extracted geometry's lumbar Cobb was 5°. Both of these are in line with published Cobb uncertainties.

Table 6-9: Radiographic and input geometry comparisons.

Patient	Radiograph Thoracic Curve Cobb Angle (°)	Radiograph TLL Curve Cobb Angle (°)	Geometry Measured Thoracic Cobb (°)	Geometry Measured TLL Cobb (°)
1	13	25	25	35
2	44	42	23	35
3	24	38	31	45
4	0	43	0	32
5	21	27	25	21
6	0	33	0	28
7	29	37	45	42
8	34	30	26	26
9	39	33	37	11
10	24	28	31	11
11	29	0	18	0
Average±SD	23±14.3	31±11.7	24±13.8	26±14.1

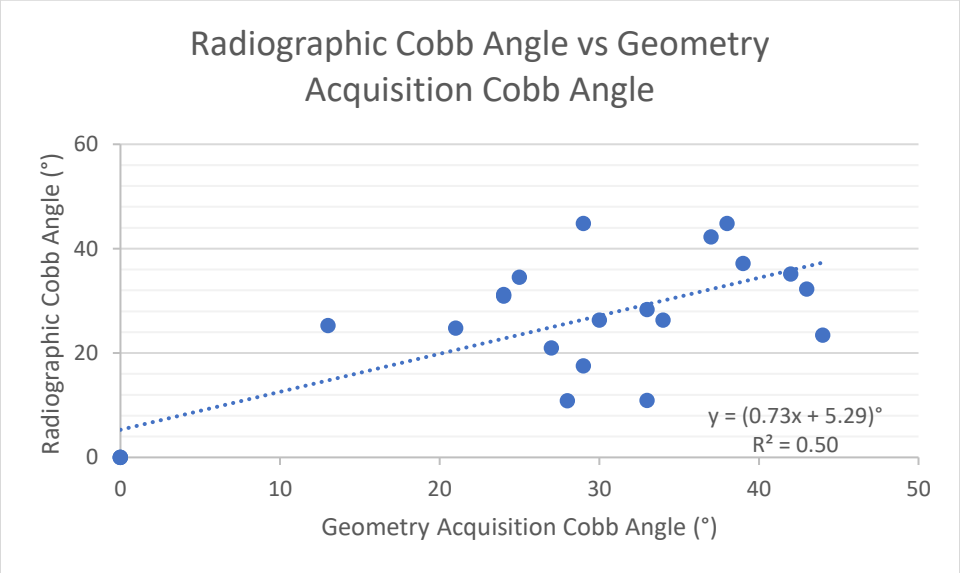

Figure 6-10. Plot of radiographic Cobb against geometry acquisition Cobb

6.4.3 Simulation Evaluation on Subject 11

The patient who was tested the casting frame and described in section 5.5.1 was used to evaluate the simulation model. As there was no ruler in the PA radiograph, the T12 vertebral body height was assumed to be about 2 cm and used for the scale based on measurements taken on other subjects' radiographs. Because it is a right thoracic curve with no lumbar component, no right-bending ultrasound was available. Due to this, the lumbar stiffness coefficient was set to 1.00. Table 6-10 looks at the in-frame results found in section 5.5.1 for subject 11, the simulated results with the forces measured (see section 5.5.1), and the optimal result using the developed simulator.

Table 6-10. Force magnitudes, force locations and results from test on subject 11.

Measure	In-Frame	Simulated	Optimal
Reaction Force Magnitude (N)	-23.1	-23.1	66
Top Force Magnitude (N)	25	25	-69
Top Force Location	T7	T7	T11
Middle Force Magnitude (N)	-7.4	-7.4	-67
Middle Force Location	T12	T12	T12
Bottom Force Magnitude (N)	5.5	5.5	70
Bottom Force Location	L1	L1	L4
Cobb Angle (°)	15	13	4
Correction (%)	48	55	86

Figure 6-11 contains, for subject 11, a) the postero-anterior radiograph, b) right-bending ultrasound, c) the extracted geometry plot, d) the in-frame ultrasound with applied forces shown, e) the simulation-optimized plot, and f) the in-frame plot (red) and the simulated plot with in-frame forces (blue).

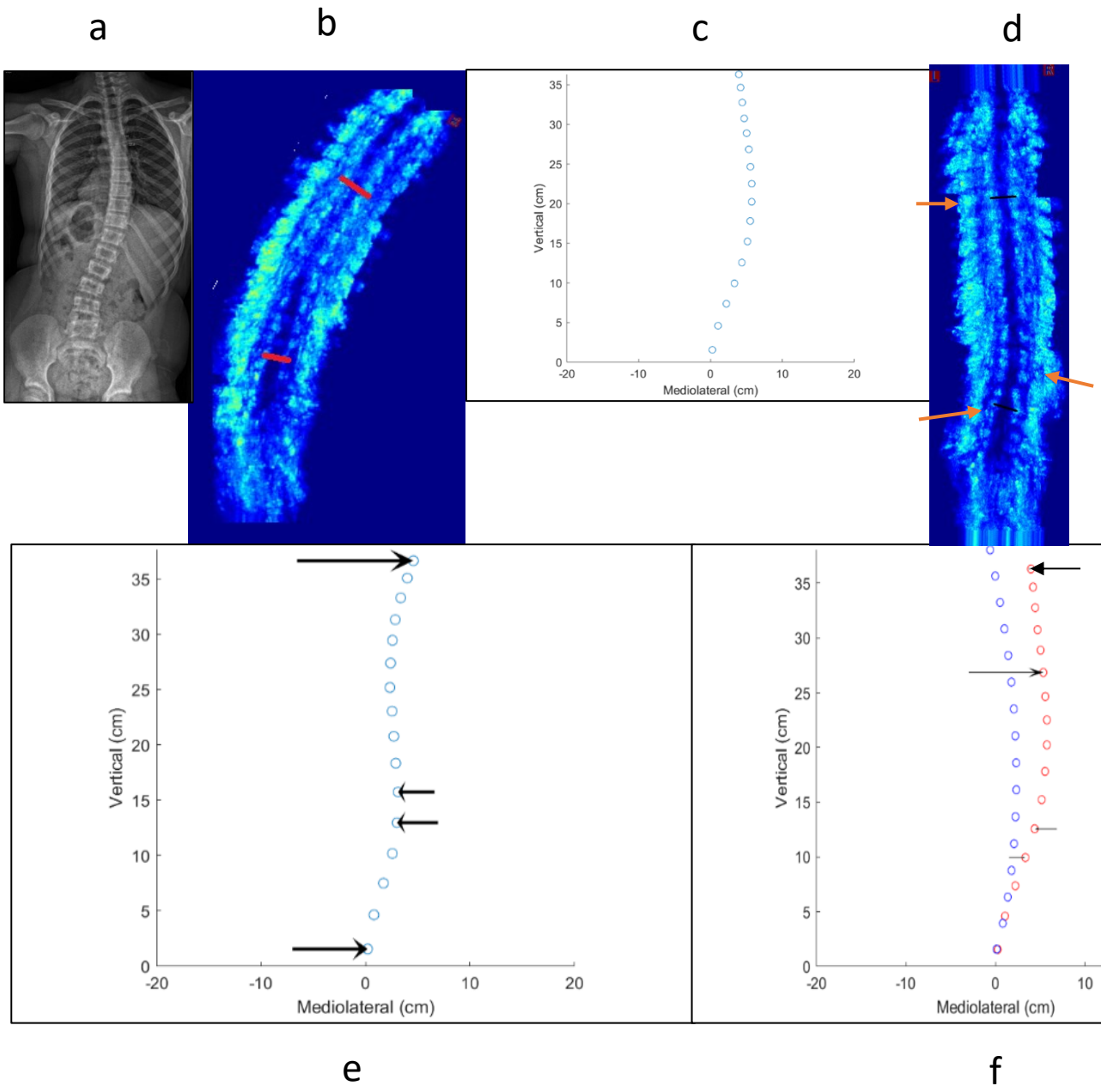

Figure 6-11. Subject 11. a) postero-anterior radiograph a 29° right thoracic curve, b) the right-bending ultrasound, c) the extracted geometry plot with a thoracic Cobb angle of 18°, d) the in-frame ultrasound with bolster forces indicated, e) the simulated results of the optimized plot with a thoracic Cobb angle of 4° and f) the actual in-brace radiograph in red with a thoracic Cobb angle of 15° and the simulated plot under in-frame forces in blue with a Cobb angle of 13°. The patient's deviation criterion improved by 68%.

The in-brace Cobb values and values determined by simulating the casting forces are very similar (15° vs 13°) and produce plots that look similar. The optimized correction seems good from its numerical value, which was a Cobb angle of 4°, but the plot shows a secondary curve resulting.

6.4.4 Linearity

The highest rotation of any intervertebral joint in the corrected test set was 0.57 radians (33 degrees). The source used for the paper that gave the spinal stiffnesses [123] shows that the response of the intervertebral joint in the Z-direction is linear up to at least 1.5 radians, where the graph is truncated. Figure 6-12 shows the plot of applied moment (N-mm) (Y-axis) versus rotation (rad) (X-axis) for thoracic vertebrae rotating in the Z-direction (ϕ_z) [123]. The linearity assumption is therefore concluded to hold.

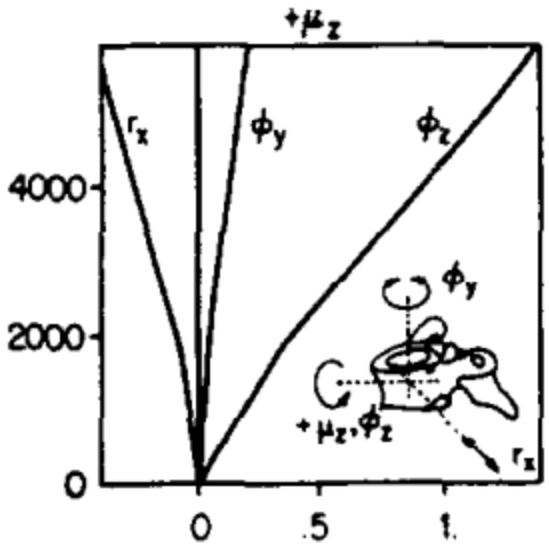

Figure 6-12. Plot of moment response of thoracic vertebrae. ϕ_z is the rotation used in this simulation [123]

6.5 Discussion

Overall, the simulation provided reasonable results at the first iteration. However, it is still not ready for clinical use yet because of relatively poor predictive value. The simulated corrections calculated averaged about 2/3 of the clinical value, the results comparable to one early FEA paper. In

Périé et al., 2003 study, their FEA in-brace simulation model produced a correction of 9° which was 56% of the actual 16° in-brace correction [56].

Although the proposed geometry extraction method is simplistic when compared to other methods, it captured the coronal characteristics of the curve without requiring special tests or equipment. There was moderate correlation, R^2=0.50, and good average matching of Cobb angle (<5°) for the geometry acquisition process. To improve the simulation, it could be extended to sagittal if those radiographs were available. Furthermore, since axial vertebral rotation can be estimated from the radiograph based on Stokes' method, it should also be implemented in the future, especially as there is coupling between the coronal and transverse planes. However, adding 3D characteristics requires a great deal of processing resources so the exhaustive approach might need to change.

By lumping the IVJ into a single spherical joint, more simplification resulted, but again likely without loss of important information as the specifics of which part of the joint moves is not of much interest for brace correction, and the cadaver stiffness values included the entire joint except for active muscle contributions. Using adult joint stiffness values, which were available in the literature, was not problematic due to the personalization process to match them to patients.

The personalization process implemented here produced somewhat unexpected values. Especially, subject 11 had the most flexible spine with a flexibility value of 183%, but the stiffness coefficient was on the lower-middle range. This may be due to the long length of the curve, which consisted of nine vertebrae. In this study, the average lumbar stiffness coefficient was 1.28 and the average thoracic stiffness was 1.38. This is substantially lower than the values found in Petit et al., 2004, which had an average lumbar stiffness of 3.46 and an average thoracic stiffness coefficient of 5.46. The difference may be because that study used surgical patients who likely had stiffer spines.

The deviation criterion approach was successful in this research. It is easy and fast to calculate and corrects the curve in the desired manner. However, subject 11 had unexpected result where the deviation criterion produced a secondary curve.

One of the limitations of the proposed method was the maximum forces which allowed for simulation were ±70 N. These force values were the maximum value found in the developed 3D brace casting frame. Although this restriction affects the optimized simulation process, it meets the real situation as too much forces apply to skin may make patient uncomfortable.

6.6 Conclusion

A simulation model for calculating brace bolsters' positions for AIS was designed. It was tested on eleven subjects, including one subject who was cast in the developed 3D brace casting frame. The simulation used lumped FEA to determine the optimal forces to apply in a brace to correct a scoliotic curve. To apply the simulation, geometry acquisition, personalization procedure and intervertebral joint modeling were required and the estimated acquisition methods were simple enough and deemed to be appropriate.

Chapter 7: Conclusion, Limitations and Future Recommendations

7.0 Summary

Adolescent idiopathic scoliosis (AIS) is a three-dimensional spinal curvature with vertebral rotation. The Heuter-Volkmann theory can be used to explain the progressive case of scoliosis. Treatments include observation, physical therapy, bracing or surgery. In term of brace treatment, there are several main types of braces including CTLSO, TLSO and nighttime braces, and they are divided into multiple subtypes with different theories of operation and construction. AIS braces can be designed using plaster, CAD/CAM, surface topography, or combinations of these. Among many different types of braces, the Boston brace, Chêneau brace, Lyon ARTbrace, Providence brace and Charleston brace are the most common types. In Edmonton a custom type brace has been used at the Glenrose Rehabilitation Hospital. All of these braces are rigid. Braces usually use pads to produce correction but can also have the brace shell shaped to directly provide forces. Both active and passive correction theories can be used to explain how brace works. Today, the outcomes of brace treatment are still difficult to predict when the brace is just prescribed to a patient. One of the predictors from the literature is the spinal flexibility. Unfortunately, there is no standard way to estimate the spinal flexibility for brace patients without using x-ray radiography. The ultrasound imaging method is only available in few centers in the world. Therefore, one of my studies was to develop a method to estimate the spinal flexibility based on standard clinical data. In my study, 14 subjects were recruited. The curve characteristics (Cobb angle, number of vertebrae involved with the curve, axial vertebral rotation), Risser sign and body mass index were used to develop the model. Single linear regression was used due to the small sample size. The sample was broken into subcategories with several predictive factors applied independently. The coefficient of determination reached up to 0.43 in thoracic curves being predicted by the length of the curve, while the median absolute residual was at a minimum of 5.6% for curves with large rotations being predicted by the axial vertebral rotation. This estimator can be used in other scoliosis centers in which ultrasound is not available for scoliosis clinic.

After the spinal flexibility was estimated, a 3D brace casting frame was designed. Originally, metal was avoided in the design because it was thought that it might influence the accuracy of the electromagnetic guidance positioning system within the ultrasound machine. Therefore, wood and plastic were used for the frame during the iterative designs. As more experiments were performed,

aluminum was found to have little-to-no interference with the electromagnetic system. The final frame was then constructed primarily using wood and aluminum to provide sufficient durability. A volunteer and two scoliotic subjects were used to validate the designed frame. The results confirmed that the frame provided enough strength to hold the spinal curves in place while orthotists was able to apply significant amount of forces at brace bolsters. The frame bolsters could be moved freely and applied at a variety of locations and directions. These bolsters were also instrumented to allow determination of pad location, direction, force magnitude and contact interface pressure. The collected information was used for testing the simulation model in chapter 6 of this thesis.

In chapter 6, a numerical lumped body analysis was performed to determine the effects of brace pad placement and also to predict optimal results. It was developed using matrix methods in MATLAB. The spine's stiffness was determined using published values determined from adult cadavers. As the stiffness values derived from adult cadaver are not comparable with values from adolescents, the stiffness was customized to each patient based on the results which was derived from the ultrasound bending test. The spinal geometry information was extracted from the PA radiographs using a custom MATLAB program. A total of 11 AIS brace cases were included in this study to validate the simulation model. The numerical model produced a smaller curve correction than actual in-brace correction, indicating corrections about 30% smaller than the actual in-brace corrections.

7.1 Contributions and Achievement

Flexibility is an objective measure of a scoliotic curve, useful for both bracing and surgery. To determine the flexibility, the traditional method using patient's postero-anterior radiograph and the bending radiographs. An ultrasound imaging method was recently introduced and based on similar procedure. However, the extra radiographs for the bending test is undesirable because of radiation exposure concerns. Ultrasound is not widely available in scoliosis clinics. A mathematical model to predict spinal flexibility was developed using single linear regression during this research by using regular standing radiograph to avoid extra ionizing radiation exposure from the extra bending radiographs. This model only requires standard clinical data to estimate the spinal flexibility.

Brace casting is mainly focused on two-dimensional because of the standard 2D radiograph. Some braces do offer 3D correction, but this is usually added after the casting process in CAD/CAM software. The applied forces or pressures and direction of brace pads are generally unknown during the

casting process. Therefore, a 3D casting frame was designed and constructed for patients to stand inside, which additionally allows measurement of bolster pressures and forces, and permits real-time ultrasound to be used to verify whether the pad placement is optimal. The collected information combined with the estimate flexibility can be used to predict in-brace outcomes.

Furthermore, literature reported finite element analysis simulations were difficult to use. Experts were required to operate them, full 3D imaging using surface topography, extra radiographs, or both, was required for the geometry, and the computing requirements were prohibitive. As a result, simulations were rarely used in the clinic. A lumped element analysis simulation was developed for use with the developed casting frame. Using a lumped element analysis and an estimated spinal geometry from PA radiograph, estimated optimal force magnitudes and locations of bolsters can be determined. This simulator can be operated by an inexperienced user with few instructions. The whole process only takes several minutes to acquire the spinal geometry and execute the program, which is a significant improvement over previous models.

7.2 Future Recommendations

1. The flexibility model should be further improved to provide a more accurate model. More clinical data is required to develop a complete model, which should use multiple linear regression. Flexibility prediction does not constitute the final limits of the model. It should also be made to produce all inputs for the spinal stiffness personalization process in the simulation presented in chapter 6, with bending test T1 lateral displacement being the most important additional output.
2. The frame has been used in the clinic and is basically acceptable, but still needs improvement. The crossbars should be connected to the vertical columns with slider parts rather than a single T-nut to allow easier movement of the crossbars. This should further remove the need for lubricant, which is inconvenient due to the mess and increased time spent on maintenance. If possible, force-sensing load cells should be introduced in-line with the pressure-sensing air bags to allow improved accuracy in determining forces during the casting process, which allows further analysis and allows the simulation to be used.
3. The simulation currently only analyzes the coronal deformity. Ideally, all three planes (coronal, sagittal and axial) should be considered to allow improved results. Axial vertebral rotation (AVR) is available from the standard radiograph and could be implemented without additional

radiographs. AVR is an important feature to be added because there is coupling between transverse plane and coronal plane deformities. If a sagittal radiograph or 3D image is available, hyper- and hypokyphosis can be considered.

References

[1] M. R. Konieczny, H. Senyurt, and R. Krauspe, “Epidemiology of adolescent idiopathic scoliosis,” *J. Child. Orthop.*, vol. 7, no. 1, pp. 3–9, Feb. 2013, doi: 10.1007/s11832-012-0457-4.

[2] S. L. Weinstein, L. A. Dolan, J. G. Wright, and M. B. Dobbs, “Effects of bracing in adolescents with idiopathic scoliosis,” *N. Engl. J. Med.*, vol. 369, no. 16, pp. 1512–1521, Oct. 2013, doi: 10.1056/NEJMoa1307337.

[3] E. Lou, J. V. Raso, D. L. Hill, J. K. Mahood, and M. J. Moreau, “Correlation between quantity and quality of orthosis wear and treatment outcomes in adolescent idiopathic scoliosis,” *Prosthet. Orthot. Int.*, vol. 28, no. 1, pp. 49–54, Apr. 2004, doi: 10.3109/03093640409167925.

[4] G. Cheh, L. G. Lenke, R. A. Lehman, Y. J. Kim, R. Nunley, and K. H. Bridwell, “The Reliability of Preoperative Supine Radiographs to Predict the Amount of Curve Flexibility in Adolescent Idiopathic Scoliosis,” *Spine*, vol. 32, no. 24, pp. 2668–2672, Nov. 2007, doi: 10.1097/brs.0b013e31815a5269.

[5] W. Chen, L. H. Le, and E. H. M. Lou, “Ultrasound Imaging of Spinal Vertebrae to Study Scoliosis,” vol. 2012, Sep. 2012, doi: 10.4236/oja.2012.23011.

[6] J. Clin, C.-E. Aubin, S. Parent, A. Sangole, and H. Labelle, “Comparison of the biomechanical 3D efficiency of different brace designs for the treatment of scoliosis using a finite element model,” *Eur. Spine J.*, vol. 19, no. 7, pp. 1169–1178, Jan. 2010, doi: 10.1007/s00586-009-1268-2.

[7] R. Zheng *et al.*, “Assessment of Curve Flexibility on Scoliotic Surgical Candidates Using Ultrasound Imaging Method,” *Ultrasound Med. Biol.*, vol. 43, no. 5, pp. 934–942, May 2017, doi: 10.1016/j.ultrasmedbio.2017.01.017.

[8] J. A. Gosling, P. F. Harris, J. R. Humpherson, I. Whitmore, and P. L. T. Willan, “Human Anatomy,” pp. 25–69, 2008, doi: 10.1016/b978-0-7234-3451-1.50006-7.

[9] F. Netter, *Atlas of Human Anatomy*, 6th ed. .

[10] I. A. F. Stokes, “Three-Dimensional Terminology of Spinal Deformity,” *Spine*, vol. 19, no. Supplement, pp. 236–248, Jan. 1994, doi: 10.1097/00007632-199401001-00020.

[11] C. R. Weatherley, “THE RIB DEFORMITY IN ADOLESCENT IDIOPATHIC SCOLIOSIS,” *J Bone Jt. Surg Br*, vol. 69, no. 2, pp. 179–182.

[12] J. Cobb, “Outline for the study of scoliosis,” *Instr Course Lect 5*, pp. 261–275.

[13] J. Van Goethem, A. Van Campenhout, L. van den Hauwe, and P. M. Parizel, “Scoliosis,” *Neuroimaging Clin. N. Am.*, vol. 17, no. 1, pp. 105–115, Feb. 2007, doi: 10.1016/j.nic.2006.12.001.

[14] K. Pehrsson, S. Larsson, A. Oden, and A. Nachemson, “Long-Term Follow-Up of Patients with Untreated Scoliosis A Study of Mortality, Causes of Death, and Symptoms,” *Spine*, vol. 17, no. 9, pp. 1091–1096, Sep. 1992, doi: 10.1097/00007632-199209000-00014.

[15] E. Riseborough and R. Wynne-Davies, “A Genetic Survey of Idiopathic Scoliosis in Boston, Massachusetts,” *J. Bone Jt. Surg.*, vol. 55, no. 5, pp. 974–982, Jul. 1973, doi: 10.2106/00004623-197355050-00006.

[16] M. A. Asher and D. C. Burton, “Adolescent idiopathic scoliosis: natural history and long term treatment effects,” *Scoliosis*, vol. 1, no. 1, Mar. 2006, doi: 10.1186/1748-7161-1-2.

[17] J. E. Lonstein and J. M. Carlson, “The prediction of curve progression in untreated idiopathic scoliosis during growth.,” *J. Bone Jt. Surg.*, vol. 66, no. 7, pp. 1061–1071, Sep. 1984, doi: 10.2106/00004623-198466070-00013.

[18] M. B. Dobbs and S. L. Weinstein, “Infantile and juvenile scoliosis,” *Orthop. Clin. North Am.*, vol. 30, no. 3, pp. 331–341, Jul. 1999, doi: 10.1016/s0030-5898(05)70090-0.

[19] S. L. Weinstein, L. A. Dolan, K. F. Spratt, K. K. Peterson, M. J. Spoonamore, and I. V. Ponseti, "Health and Function of Patients With Untreated Idiopathic Scoliosis," *JAMA*, vol. 289, no. 5, p. 559, Feb. 2003, doi: 10.1001/jama.289.5.559.

[20] S. Swank, R. Winter, and J. Moe, "Scoliosis and Cor Pulmonale," *Spine*, vol. 7, no. 4, pp. 343–354, Jul. 1982, doi: 10.1097/00007632-198207000-00004.

[21] R. E. Will, I. A. Stokes, X. Qiu, M. R. Walker, and J. O. Sanders, "Cobb Angle Progression in Adolescent Scoliosis Begins at the Intervertebral Disc," *Spine*, vol. 34, no. 25, pp. 2782–2786, Dec. 2009, doi: 10.1097/BRS.0b013e3181c11853.

[22] T. B. Grivas, G. I. Rodopoulos, and N. V. Bardakos, "Night-time braces for treatment of Adolescent Idiopathic Scoliosis," *Disabil. Rehabil. Assist. Technol.*, vol. 3, no. 3, pp. 120–129, Jan. 2008, doi: 10.1080/17483100801903954.

[23] S. C. W. Chan, S. J. Ferguson, and B. Gantenbein-Ritter, "The effects of dynamic loading on the intervertebral disc," *Eur. Spine J.*, vol. 20, no. 11, pp. 1796–1812, May 2011, doi: 10.1007/s00586-011-1827-1.

[24] F. P. Castro, "Adolescent idiopathic scoliosis, bracing, and the Hueter-Volkmann principle," *Spine J.*, vol. 3, no. 3, pp. 180–185, May 2003, doi: 10.1016/s1529-9430(02)00557-0.

[25] I. A. Stokes, R. G. Burwell, and P. H. Dangerfield, "Biomechanical spinal growth modulation and progressive adolescent scoliosis – a test of the 'vicious cycle' pathogenetic hypothesis: Summary of an electronic focus group debate of the IBSE," *Scoliosis*, vol. 1, no. 1, Oct. 2006, doi: 10.1186/1748-7161-1-16.

[26] F. Canavese and A. Kaelin, "Adolescent idiopathic scoliosis: Indications and efficacy of nonoperative treatment," *Indian J. Orthop.*, vol. 45, no. 1, pp. 7–14, 2011, doi: 10.4103/0019-5413.73655.

[27] C. Fusco, F. Zaina, S. Atanasio, M. Romano, A. Negrini, and S. Negrini, "Physical exercises in the treatment of adolescent idiopathic scoliosis: An updated systematic review," *Physiother. Theory Pract.*, vol. 27, no. 1, pp. 80–114, Jan. 2011, doi: 10.3109/09593985.2010.533342.

[28] Y. J. Kim *et al.*, "Comparative Analysis of Pedicle Screw Versus Hybrid Instrumentation in Posterior Spinal Fusion of Adolescent Idiopathic Scoliosis," *Spine*, vol. 31, no. 3, pp. 291–298, Feb. 2006, doi: 10.1097/01.brs.0000197865.20803.d4.

[29] J. E. Lonstein and R. B. Winter, "The Milwaukee brace for the treatment of adolescent idiopathic scoliosis. A review of one thousand and twenty patients," *J. Bone Joint Surg. Am.*, vol. 76, no. 8, pp. 1207–1221, Aug. 1994.

[30] K. J. Ng, K. Duke, and E. Lou, "Investigation of future 3D printed brace design parameters: evaluation of mechanical properties and prototype outcomes," *J. 3D Print. Med.*, vol. 3, no. 4, pp. 171–184, Nov. 2019, doi: 10.2217/3dp-2019-0012.

[31] J. W. Wiley, J. D. Thomson, T. M. Mitchell, B. G. Smith, and J. V. Banta, "Effectiveness of The Boston Brace in Treatment of Large Curves in Adolescent Idiopathic Scoliosis," *Spine*, vol. 25, no. 18, pp. 2326–2332, Sep. 2000.

[32] K. Zaborowska-Sapeta, I. M. Kowalski, T. Kotwicki, H. Protasiewicz-Fałdowska, and W. Kiebzak, "Effectiveness of Chêneau brace treatment for idiopathic scoliosis: prospective study in 79 patients followed to skeletal maturity," *Scoliosis*, vol. 6, p. 2, 2011, doi: 10.1186/1748-7161-6-2.

[33] J. C. de Mauroy, A. Journe, F. Gagaliano, C. Lecante, F. Barral, and S. Pourret, "The new Lyon ARTbrace versus the historical Lyon brace: a prospective case series of 148 consecutive scoliosis with short time results after 1 year compared with a historical retrospective case series of 100 consecutive scoliosis; SOSORT award 2015 winner," *Scoliosis*, vol. 10, no. 1, Aug. 2015, doi: 10.1186/s13013-015-0047-6.

[34] J. M. Trivedi and J. D. Thomson, "Results of Charleston bracing in skeletally immature patients with idiopathic scoliosis," *J. Pediatr. Orthop.*, vol. 21, no. 3, pp. 277–280, Jun. 2001.

[35] C. Roland d'Amato, S. Griggs, and B. McCoy, "Nighttime Bracing With the Providence Brace in Adolescent Girls With Idiopathic Scoliosis," *Spine*, vol. 26, no. 18, pp. 2006–2012, Sep. 2001, doi: 10.1097/00007632-200109150-00014.
[36] T. Kotwicki and J. Cheneau, "Biomechanical action of a corrective brace on thoracic idiopathic scoliosis: Cheneau 2000 orthosis," *Disabil. Rehabil. Assist. Technol.*, vol. 3, no. 3, pp. 146–153, Jan. 2008, doi: 10.1080/17483100801905744.
[37] M. S. Wong, J. C. Y. Cheng, and K. H. Lo, "A comparison of treatment effectiveness between the CAD/CAM method and the manual method for managing adolescent idiopathic scoliosis," *Prosthet. Orthot. Int.*, vol. 29, no. 1, pp. 105–111, Apr. 2005, doi: 10.1080/17461550500069547.
[38] C. T. Price, D. S. Scott, F. E. Reed, and M. Riddick, "Nighttime Bracing for Adolescent Idiopathic Scoliosis with the Charleston Bending Brace," *Spine*, vol. 15, no. 12, pp. 1294–1299, Dec. 1990, doi: 10.1097/00007632-199012000-00011.
[39] J. Clin, C.-É. Aubin, N. Lalonde, S. Parent, and H. Labelle, "A new method to include the gravitational forces in a finite element model of the scoliotic spine," *Med. Biol. Eng. Comput.*, vol. 49, no. 8, pp. 967–977, Aug. 2011, doi: 10.1007/s11517-011-0793-4.
[40] A. Rohlmann, L. Bauer, T. Zander, G. Bergmann, and H.-J. Wilke, "Determination of trunk muscle forces for flexion and extension by using a validated finite element model of the lumbar spine and measured in vivo data," *J. Biomech.*, vol. 39, no. 6, pp. 981–989, Jan. 2006, doi: 10.1016/j.jbiomech.2005.02.019.
[41] "A biomechanical analog of curve progression and orthotic stabilization in idiopathic scoliosis," *Clin. Biomech.*, vol. 1, no. 3, p. 169, Aug. 1986, doi: 10.1016/0268-0033(86)90014-8.
[42] "Boston Brace," *BracingScoliosis.com - The Scoliosis Patient and Pratitioner Bracing Information Network*. http://www.bracingscoliosis.com/boston-brace.html (accessed Mar. 15, 2017).
[43] M. Rigo and M. Jelačić, "Brace technology thematic series: the 3D Rigo Chêneau-type brace," *Scoliosis Spinal Disord.*, vol. 12, no. 1, p. 10, Dec. 2017, doi: 10.1186/s13013-017-0114-2.
[44] "Un nouveau corset lyonnais de correction des scolioses : l'ARTbrace - Clinique du Parc à Lyon (69)." http://www.cliniqueduparclyon.com/fr/content/nouveau-corset-lyonnais-correction-scolioses-artbrace (accessed Apr. 28, 2020).
[45] "Scoliosis," *Florida Orthotics and Prosthetics Westcoast Brace & Limb*. http://www.wcbl.com/orthotics-2/scoliosis-treatment/scoliosis/ (accessed Mar. 15, 2017).
[46] "Back Brace, Scoliosis Brace,Charleston Bending Brace," *De La Torre Orthotics & Prosthetics*. https://www.delatorreop.com/product/charleston-bending-brace-scoliosis-brace/ (accessed Mar. 15, 2017).
[47] C.-É. Aubin, J. Dansereau, J. A. de Guise, and H. Labelle, "Rib Cage-Spine Coupling Patterns Involved in Brace Treatment of Adolescent Idiopathic Scoliosis," *Spine*, vol. 22, no. 6, pp. 629–635, Mar. 1997, doi: 10.1097/00007632-199703150-00010.
[48] I. Boston Brace, "REFERENCE MANUAL FOR THE BOSTON SCOLIOSIS BRACE," 2003.
[49] J. B. Emans, A. KAELIN, P. BANCEL, J. E. HALL, and M. E. MILLER, "The Boston Bracing System for Idiopathic Scoliosis," *Spine*, vol. 11, no. 8, pp. 792–801, Oct. 1986, doi: 10.1097/00007632-198610000-00009.
[50] M. Rigo, S. Negrini, H. Weiss, T. Grivas, T. Maruyama, and T. Kotwicki, "'SOSORT consensus paper on brace action: TLSO biomechanics of correction (investigating the rationale for force vector selection),'" *Scoliosis*, vol. 1, p. 11, 2006, doi: 10.1186/1748-7161-1-11.
[51] T. Kotwicki, S. Pietrzak, and A. Szulc, "Three-dimensional action of Chêneau brace on thoracolumbar scoliosis," *Stud. Health Technol. Inform.*, vol. 88, pp. 226–229, 2002.
[52] B. M. Charles d'Amato, "The Providence Scoliosis System Manual," 2003.
[53] J. B. Reuler, "The Pressure Sore: Pathophysiology and Principles of Management," *Ann. Intern. Med.*, vol. 94, no. 5, p. 661, May 1981, doi: 10.7326/0003-4819-94-5-661.

[54] J. Clin, C.-É. Aubin, S. Parent, and H. Labelle, “A Biomechanical Study of the Charleston Brace for the Treatment of Scoliosis,” *Spine*, vol. 35, no. 19, pp. E940–E947, Sep. 2010, doi: 10.1097/brs.0b013e3181c5b5fa.
[55] J. Clin, C.-É. Aubin, S. Parent, and H. Labelle, “Biomechanical modeling of brace treatment of scoliosis: effects of gravitational loads,” *Med. Biol. Eng. Comput.*, vol. 49, no. 7, pp. 743–753, Feb. 2011, doi: 10.1007/s11517-011-0737-z.
[56] D. Périé, C.-E. Aubin, Y. Petit, M. Beauséjour, J. Dansereau, and H. Labelle, “Boston Brace Correction in Idiopathic Scoliosis: A Biomechanical Study,” *Spine*, vol. 28, no. 15, pp. 1672–1677, Aug. 2003, doi: 10.1097/01.brs.0000083165.93936.6d.
[57] P. J. M. van Loon, B. A. G. Kühbauch, and F. B. Thunnissen, “Forced Lordosis on the Thoracolumbar Junction Can Correct Coronal Plane Deformity in Adolescents With Double Major Curve Pattern Idiopathic Scoliosis,” *Spine*, vol. 33, no. 7, pp. 797–801, Apr. 2008, doi: 10.1097/brs.0b013e3181694ff5.
[58] C. Hooper, F. Reed, and C. Price, “Charleston Bending Brace.”
[59] D. Odermatt, P. A. Mathieu, M. Beauséjour, H. Labelle, and C.-É. Aubin, “Electromyography of scoliotic patients treated with a brace,” *J. Orthop. Res.*, vol. 21, no. 5, pp. 931–936, Sep. 2003, doi: 10.1016/s0736-0266(03)00038-x.
[60] G. T. Wynarsky and A. B. Schultz, “Optimization of skeletal configuration: Studies of scoliosis correction biomechanics,” *J. Biomech.*, vol. 24, no. 8, pp. 721–732, Jan. 1991, doi: 10.1016/0021-9290(91)90336-l.
[61] J. P. G. Urban and A. Maroudas, “Swelling of the Intervertebral Disc in Vitro,” *Connect. Tissue Res.*, vol. 9, no. 1, pp. 1–10, Jan. 1981, doi: 10.3109/03008208109160234.
[62] I. A. F. Stokes, L. C. Bigalow, and M. S. Moreland, “Measurement of Axial Rotation of Vertebrae in Scoliosis,” *Spine*, vol. 11, no. 3, pp. 213–218, Apr. 1986, doi: 10.1097/00007632-198604000-00006.
[63] S. Suzuki, T. Yamamuro, J. Shikata, K. Shimizu, and H. Iida, “Ultrasound measurement of vertebral rotation in idiopathic scoliosis,” *Bone Jt. J.*, vol. 71-B, no. 2, pp. 252–255, Mar. 1989.
[64] Q. N. Vo, E. H. Lou, and L. H. Le, “Measurement of axial vertebral rotation using three-dimensional ultrasound images,” *Scoliosis*, vol. 10, no. 2, p. S7, 2015, doi: 10.1186/1748-7161-10-S2-S7.
[65] V. Pomero *et al.*, “Fast semiautomatic stereoradiographic reconstruction of scoliotic spines using multi-scale image processing and statistical geometric models,” *Int. Congr. Ser.*, vol. 1256, pp. 207–213, Jun. 2003, doi: 10.1016/S0531-5131(03)00395-9.
[66] Glaser DA, Doan J, and Newton PO, “Comparison of 3-Dimensional Spinal Reconstruction Accuracy: Biplanar Radiographs With EOS Versus Computed Tomography,” *Spine 03622436*, vol. 37, no. 16, pp. 1391–1397, Jul. 2012, doi: 10.1097/BRS.0b013e3182518a15.
[67] S. Deschênes *et al.*, “Diagnostic Imaging of Spinal Deformities: Reducing Patients Radiation Dose With a New Slot-Scanning X-ray Imager,” *Spine*, vol. 35, no. 9, pp. 989–994, Apr. 2010, doi: 10.1097/BRS.0b013e3181bdcaa4.
[68] B. S. Richards, R. M. Bernstein, C. R. D’Amato, and G. H. Thompson, “Standardization of Criteria for Adolescent Idiopathic Scoliosis Brace Studies: SRS Committee on Bracing and Nonoperative Management,” *Spine*, vol. 30, no. 18, pp. 2068–2075, Sep. 2005, doi: 10.1097/01.brs.0000178819.90239.d0.
[69] D. E. Katz and A. A. Durrani, “Factors That Influence Outcome in Bracing Large Curves in Patients With Adolescent Idiopathic Scoliosis,” *Spine*, vol. 26, no. 21, pp. 2354–2361, Nov. 2001, doi: 10.1097/00007632-200111010-00012.

[70] E. Jb, K. A, B. P, H. Je, and M. Me, “The Boston bracing system for idiopathic scoliosis. Follow-up results in 295 patients.,” *Spine*, vol. 11, no. 8, pp. 792–801, Oct. 1986, doi: 10.1097/00007632-198610000-00009.

[71] A. P. Chase, D. L. Bader, and G. R. Houghton, “The Biomechanical Effectiveness of the Boston Brace in the Management of Adolescent Idiopathic Scoliosis,” *Spine*, vol. 14, no. 6, pp. 636–642, Jun. 1989, doi: 10.1097/00007632-198906000-00018.

[72] T. Yrjönen, M. Ylikoski, D. Schlenzka, and M. Poussa, “Results of brace treatment of adolescent idiopathic scoliosis in boys compared with girls: a retrospective study of 102 patients treated with the Boston brace,” *Eur. Spine J.*, vol. 16, no. 3, pp. 393–397, Mar. 2007, doi: 10.1007/s00586-006-0167-z.

[73] W. K. I. Payne, J. W. Ogilvie, M. D. Resnick, R. L. Kane, E. E. Transfeldt, and R. W. Blum, “Does Scoliosis Have a Psychological Impact and Does Gender Make a Difference?,” *Spine*, vol. 22, no. 12, pp. 1380–1384, Jun. 1997.

[74] D. G. M. B. B. S. Little and M. D. M. D. Sussman, “The Risser Sign: A Critical Analysis,” *J. Pediatr. Orthop.*, vol. 14, no. 5, pp. 569–575, Oct. 1994.

[75] Little DG *et al.*, “Relationship of peak height velocity to other maturity indicators in idiopathic scoliosis in girls,” *J. Bone Joint Surg. Am.*, vol. 82, no. 5, pp. 685–693, May 2000.

[76] W. A. Marshall and Y. D. Limongi, “Skeletal maturity and the prediction of age at menarche,” *Ann. Hum. Biol.*, vol. 3, no. 3, pp. 235–243, Jan. 1976, doi: 10.1080/03014467600001401.

[77] F. Landauer, C. Wimmer, and H. Behensky, “Estimating the final outcome of brace treatment for idiopathic thoracic scoliosis at 6-month follow-up,” *Pediatr. Rehabil.*, vol. 6, no. 3–4, pp. 201–207, Jul. 2003, doi: 10.1080/13638490310001636817.

[78] M. Takemitsu, J. R. Bowen, T. Rahman, J. J. Glutting, and C. B. Scott, “Compliance Monitoring of Brace Treatment for Patients with Idiopathic Scoliosis,” *Spine*, vol. 29, no. 18, pp. 2070–2074, Sep. 2004, doi: 10.1097/01.brs.0000138280.43663.7b.

[79] D. E. Katz, J. A. Herring, R. H. Browne, D. M. Kelly, and J. G. Birch, “Brace Wear Control of Curve Progression in Adolescent Idiopathic Scoliosis,” *J. Bone Jt. Surg.-Am. Vol.*, vol. 92, no. 6, pp. 1343–1352, Jun. 2010, doi: 10.2106/jbjs.i.01142.

[80] S. Kahana, D. Drotar, and T. Frazier, “Meta-Analysis of Psychological Interventions to Promote Adherence to Treatment in Pediatric Chronic Health Conditions,” *J. Pediatr. Psychol.*, vol. 33, no. 6, pp. 590–611, Oct. 2007, doi: 10.1093/jpepsy/jsm128.

[81] A. Morton, R. Riddle, R. Buchanan, D. Katz, and J. Birch, “Accuracy in the Prediction and Estimation of Adherence to Bracewear Before and During Treatment of Adolescent Idiopathic Scoliosis,” *J. Pediatr. Orthop.*, vol. 28, no. 3, pp. 336–341, Apr. 2008, doi: 10.1097/bpo.0b013e318168d154.

[82] K. Kuklane, S. Heidmets, and T. Johansson, “Improving thermal comfort in an orthopaedic aid: better Boston brace for scoliosis patients,” *6th Int. Therm. Manikin Model. Meet. 6I3M*, pp. 343–351, 2006.

[83] Aubin C *et al.*, “Variability of strap tension in brace treatment for adolescent idiopathic scoliosis,” *Spine 03622436*, vol. 24, no. 4, pp. 349–354, Feb. 1999.

[84] F.-H. Cheng, S.-L. Shih, W.-K. Chou, C.-L. Liu, W.-H. Sung, and C.-S. Chen, “Finite element analysis of the scoliotic spine under different loading conditions,” *Biomed. Mater. Eng.*, vol. 20, no. 5, pp. 251–259, 2010, doi: 10.3233/BME-2010-0639.

[85] K. M. C. Cheung and K. D. K. Luk, “Prediction of Correction of Scoliosis with Use of the Fulcrum Bending Radiograph*,” *J Bone Jt. Surg Am*, vol. 79, no. 8, pp. 1144–50, Aug. 1997.

[86] S. J. Klepps, L. G. Lenke, K. H. Bridwell, G. S. Bassett, and J. Whorton, “Prospective Comparison of Flexibility Radiographs in Adolescent Idiopathic Scoliosis,” *Spine*, vol. 26, no. 5, pp. E74–E79, Mar. 2001, doi: 10.1097/00007632-200103010-00002.

[87] R. G. Kleinman, J. J. Csongradi, L. A. Rinksy, and E. E. Bleck, “The Radiographic Assessment of Spinal Flexibility in Scoliosis,” *Clin. Orthop.*, vol. NA;, no. 162, p. 47???53, Jan. 1982, doi: 10.1097/00003086-198201000-00009.
[88] A. Hamzaoglu, U. Talu, M. Tezer, C. Mirzanli, U. Domanic, and S. B. Goksan, “Assessment of curve flexibility in adolescent idiopathic scoliosis,” *Spine*, vol. 30, no. 14, pp. 1637–1642, Jul. 2005.
[89] D. W. Polly Jr and P. F. Sturm, “Traction versus supine side bending. Which technique best determines curve flexibility?,” *Spine*, vol. 23, no. 7, pp. 804–808, Apr. 1998.
[90] O. Delialioglu *et al.*, “Which Technique Is Best? Traction Before General Anesthesia or Under General Anesthesia,” *Orthop. Proc.*, vol. 92-B, no. SUPP IV, pp. 563–563, Oct. 2010.
[91] M.-E. Lamarre *et al.*, “Assessment of Spinal Flexibility in Adolescent Idiopathic Scoliosis: Suspension Versus Side-Bending Radiography,” *Spine*, vol. 34, no. 6, pp. 591–597, Mar. 2009, doi: 10.1097/BRS.0b013e318193a23d.
[92] R. W. Liu, A. L. Teng, D. G. Armstrong, C. Poe-Kochert, J. P. Son-Hing, and G. H. Thompson, “Comparison of Supine Bending, Push-Prone, and Traction Under General Anesthesia Radiographs in Predicting Curve Flexibility and Postoperative Correction in Adolescent Idiopathic Scoliosis,” *Spine*, vol. 35, no. 4, pp. 416–422, Feb. 2010, doi: 10.1097/brs.0b013e3181b3564a.
[93] L. M *et al.*, “Application of 3-D ultrasound in assisting the fitting procedure of spinal orthosis to patients with adolescent idiopathic scoliosis.,” *Stud. Health Technol. Inform.*, vol. 158, pp. 34–37, 2010.
[94] W. Chen, “Application of ultrasound to measure coronal curvature and vertebral rotation in adolescent idiopathic scoliosis,” *ERA*, Fall 2014. https://era.library.ualberta.ca/items/c665c7a9-0137-48a6-a3d5-84ca4f85b2e3 (accessed Apr. 28, 2020).
[95] Q. Wang, M. Li, E. H. M. Lou, and M. S. Wong, “Reliability and Validity Study of Clinical Ultrasound Imaging on Lateral Curvature of Adolescent Idiopathic Scoliosis.,” *PLoS ONE*, vol. 10, no. 8, p. e0135264, Aug. 2015.
[96] R. Zheng *et al.*, “Improvement on the Accuracy and Reliability of Ultrasound Coronal Curvature Measurement on Adolescent Idiopathic Scoliosis With the Aid of Previous Radiographs:,” *SPINE*, vol. 41, no. 5, pp. 404–411, Mar. 2016, doi: 10.1097/BRS.0000000000001244.
[97] Z.-Q. Chen *et al.*, “Factors affecting curve flexibility in skeletally immature and mature idiopathic scoliosis,” *J. Orthop. Sci.*, vol. 16, no. 2, pp. 133–138, Mar. 2011, doi: 10.1007/s00776-011-0034-6.
[98] K. M. Flegal, M. D. Carroll, B. K. Kit, and C. L. Ogden, “Prevalence of Obesity and Trends in the Distribution of Body Mass Index Among US Adults, 1999-2010,” *JAMA*, vol. 307, no. 5, pp. 491–497, Feb. 2012, doi: 10.1001/jama.2012.39.
[99] M. R. Wiles, “Elements of Research in Physical Therapy,” *J. Can. Chiropr. Assoc.*, vol. 24, no. 2, p. 77, Jun. 1980.
[100] J. P. Weir, “Quantifying Test-Retest Reliability Using the Intraclass Correlation Coefficient and the SEM,” *J. Strength Cond. Res.*, vol. 19, no. 1, p. 231, 2005, doi: 10.1519/15184.1.
[101] M. Yagi, R. Patel, T. W. Lawhorne, M. E. Cunningham, and O. Boachie-Adjei, “Adult thoracolumbar and lumbar scoliosis treated with long vertebral fusion to the sacropelvis: a comparison between new hybrid selective spinal fusion versus anterior-posterior spinal instrumentation,” *Spine J.*, vol. 14, no. 4, pp. 637–645, Apr. 2014, doi: 10.1016/j.spinee.2013.06.090.
[102] R. T. Morrissy, G. S. Goldsmith, E. C. Hall, D. Kehl, and G. H. Cowie, “Measurement of the Cobb angle on radiographs of patients who have scoliosis. Evaluation of intrinsic error,” *J. Bone Jt. Surg.*, vol. 72, no. 3, pp. 320–327, Mar. 1990, doi: 10.2106/00004623-199072030-00002.
[103] G. G. Russell, V. J. Raso, D. Hill, and J. McIVOR, “A Comparison of Four Computerized Methods for Measuring Vertebral Rotation:,” *Spine*, vol. 15, no. 1, pp. 24–27, Jan. 1990, doi: 10.1097/00007632-199001000-00007.

[104] W. Chen, E. H. M. Lou, P. Q. Zhang, L. H. Le, and D. Hill, “Reliability of assessing the coronal curvature of children with scoliosis by using ultrasound images,” *J. Child. Orthop.*, vol. 7, no. 6, pp. 521–529, Dec. 2013, doi: 10.1007/s11832-013-0539-y.
[105] V. Deviren, S. Berven, F. Kleinstueck, J. Antinnes, J. A. Smith, and S. S. Hu, “Predictors of Flexibility and Pain Patterns in Thoracolumbar and Lumbar Idiopathic Scoliosis,” *Spine*, vol. 27, no. 21, pp. 2346–2349, Nov. 2002, doi: 10.1097/00007632-200211010-00007.
[106] E. H. Lou, A. C. Chan, A. Donauer, M. Tilburn, and D. L. Hill, “Ultrasound-assisted brace casting for adolescent idiopathic scoliosis, IRSSD Best research paper 2014,” *Scoliosis*, vol. 10, p. 13, 2015, doi: 10.1186/s13013-015-0037-8.
[107] M. Young, D. L. Hill, R. Zheng, and E. Lou, “Reliability and accuracy of ultrasound measurements with and without the aid of previous radiographs in adolescent idiopathic scoliosis (AIS),” *Eur. Spine J.*, vol. 24, no. 7, pp. 1427–1433, Jul. 2015, doi: 10.1007/s00586-015-3855-8.
[108] R. Zheng *et al.*, “Intra- and Inter-rater Reliability of Coronal Curvature Measurement for Adolescent Idiopathic Scoliosis Using Ultrasonic Imaging Method—A Pilot Study,” *Spine Deform.*, vol. 3, no. 2, pp. 151–158, Mar. 2015, doi: 10.1016/j.jspd.2014.08.008.
[109] E. H. Lou, D. L. Hill, A. Donauer, M. Tilburn, D. Hedden, and M. Moreau, “Results of ultrasound-assisted brace casting for adolescent idiopathic scoliosis,” *Scoliosis Spinal Disord.*, vol. 12, no. 1, p. 23, Aug. 2017, doi: 10.1186/s13013-017-0130-2.
[110] M. Li *et al.*, “Could clinical ultrasound improve the fitting of spinal orthosis for the patients with AIS?,” *Eur. Spine J.*, vol. 21, no. 10, pp. 1926–1935, Oct. 2012, doi: 10.1007/s00586-012-2273-4.
[111] E. Chalmers, E. Lou, D. Hill, V. H. Zhao, and M.-S. Wong, “Development of a Pressure Control System for Brace Treatment of Scoliosis,” *IEEE Trans. Neural Syst. Rehabil. Eng.*, vol. 20, no. 4, pp. 557–563, Jul. 2012, doi: 10.1109/TNSRE.2012.2192483.
[112] H. Jiang, J. Raso, D. Hill, N. Durdle, and M. Moreau, “Interface pressures in the Boston brace treatment for scoliosis,” *Proc. Intl Symp. 3- Scoliotic Deform.*, pp. 395–399.
[113] “what is ABS Material properties|Acylonitrile Butadiene Styrene.” https://vexmatech.com/abs-material.html (accessed Apr. 28, 2020).
[114] “Polylactic Acid (PLA) Typical Properties | UL Prospector.” https://plastics.ulprospector.com/generics/34/c/t/polylactic-acid-pla-properties-processing (accessed Apr. 28, 2020).
[115] “Loadstar Sensors: iLoad TR Series Tilt Resistant USB Load Cell.” http://www.loadstarsensors.com/capacitive-load-cells/iload-tr-series-tilt-resistant-usb-load-cell.html (accessed Feb. 10, 2017).
[116] J. P. Little and C. J. Adam, “The Effect of Soft Tissue Properties on Spinal Flexibility in Scoliosis: Biomechanical Simulation of Fulcrum Bending,” *Spine*, vol. 34, no. 2, pp. E76–E82, Jan. 2009, doi: 10.1097/BRS.0b013e31818ad584.
[117] J. Clin, C.-É. Aubin, and H. Labelle, “Virtual prototyping of a brace design for the correction of scoliotic deformities,” *Med. Biol. Eng. Comput.*, vol. 45, no. 5, pp. 467–473, May 2007, doi: 10.1007/s11517-007-0171-4.
[118] I. Villemure, C. E. Aubin, J. Dansereau, and H. Labelle, “Biomechanical simulations of the spine deformation process in adolescent idiopathic scoliosis from different pathogenesis hypotheses,” *Eur. Spine J.*, vol. 13, no. 1, pp. 83–90, Feb. 2004, doi: 10.1007/s00586-003-0565-4.
[119] D. Gignac, C.-É. Aubin, J. Dansereau, and H. Labelle, “Optimization method for 3D bracing correction of scoliosis using a finite element model,” *Eur. Spine J.*, vol. 9, no. 3, pp. 185–190, Jun. 2000, doi: 10.1007/s005860000135.
[120] C. Aubin, “Scoliosis study using finite element models,” *Stud. Health Technol. Inform.*, vol. 91, pp. 309–313, 2001.

[121] J. Clin, C.-É. Aubin, A. Sangole, H. Labelle, and S. Parent, “Correlation Between Immediate In-Brace Correction and Biomechanical Effectiveness of Brace Treatment in Adolescent Idiopathic Scoliosis:,” *Spine*, vol. 35, no. 18, pp. 1706–1713, Aug. 2010, doi: 10.1097/BRS.0b013e3181cb46f6.
[122] Y. Petit, C. É. Aubin, and H. Labelle, “Patient-specific mechanical properties of a flexible multi-body model of the scoliotic spine,” *Med. Biol. Eng. Comput.*, vol. 42, no. 1, pp. 55–60, Jan. 2004, doi: 10.1007/BF02351011.
[123] M. M. Panjabi, R. A. Brand Jr, and A. A. White 3rd, “Three-dimensional flexibility and stiffness properties of the human thoracic spine,” *J. Biomech.*, vol. 9, no. 4, pp. 185–192, 1976.
[124] B. D. Stemper, D. Board, N. Yoganandan, and C. E. Wolfla, “Biomechanical properties of human thoracic spine disc segments,” *J. Craniovertebral Junction Spine*, vol. 1, no. 1, pp. 18–22, Jan. 2010, doi: 10.4103/0974-8237.65477.
[125] N. Yoganandan, S. Kumaresan, and F. A. Pintar, “Geometric and Mechanical Properties of Human Cervical Spine Ligaments,” *J. Biomech. Eng.*, vol. 122, no. 6, pp. 623–629, Dec. 2000, doi: 10.1115/1.1322034.
[126] D. T. Reilly, A. H. Burstein, and V. H. Frankel, “The elastic modulus for bone,” *J. Biomech.*, vol. 7, no. 3, pp. 271–275, May 1974, doi: 10.1016/0021-9290(74)90018-9.
[127] I. A. F. Stokes, D. D. Aronson, P. J. Ronchetti, H. Labelle, and J. Dansereau, “Reexamination of the Cobb and Ferguson Angles: Bigger Is Not Always Better,” *J. Spinal Disord.*, vol. 6, no. 4, pp. 333–338, Aug. 1993, doi: 10.1097/00002517-199306040-00007.

Appendix A. Results of Brace Simulation

This appendix includes the results from the simulation in chapter 6 for another seven subjects.

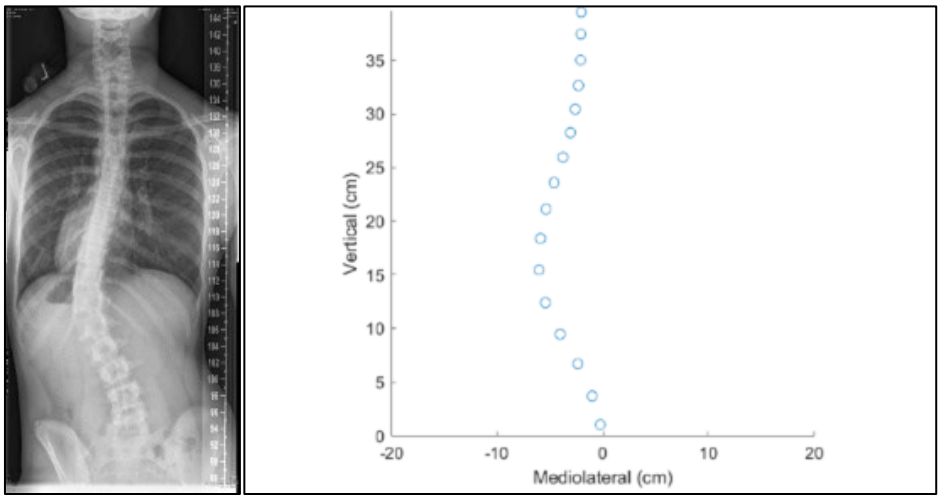

a b

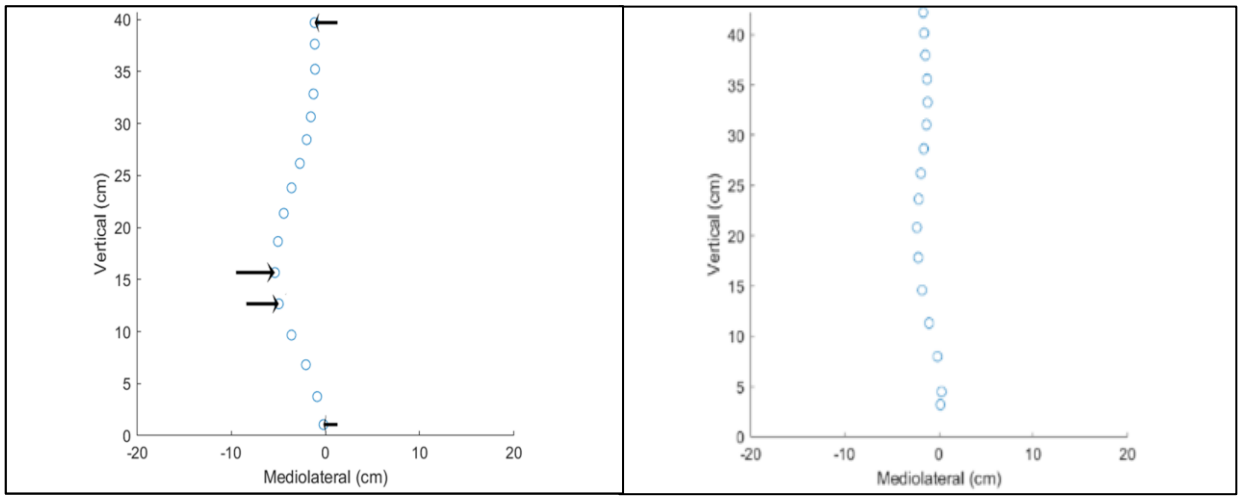

c d

Figure A-1. Subject 4. a) postero-anterior radiograph with a 43° left thoracolumbar-lumbar curve, b) the extracted geometry plot with a thoracolumbar-lumbar Cobb angle of 32°, c) the simulated results of the optimized plot with a thoracolumbar-lumbar Cobb angle of 35° and d) the actual in-brace radiograph with a thoracolumbar-lumbar Cobb angle of 16°. The patient's deviation criterion improved by 21%.

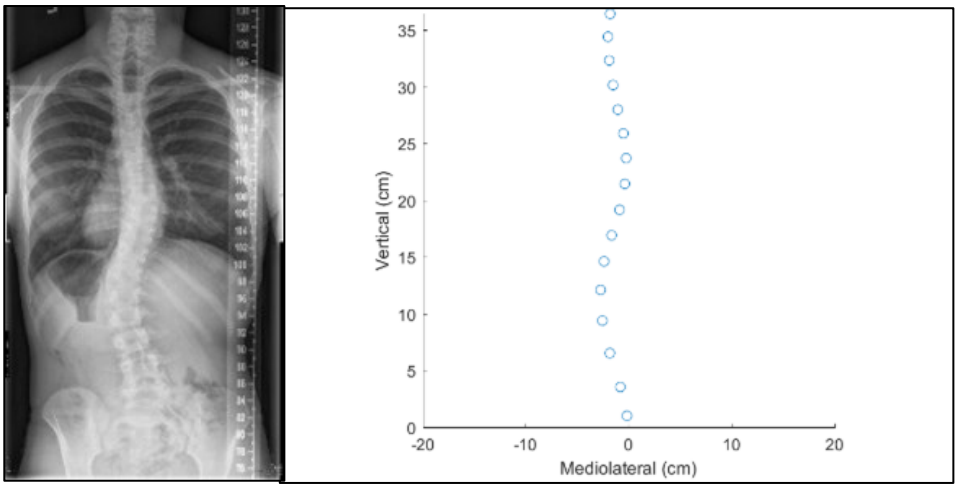

a b

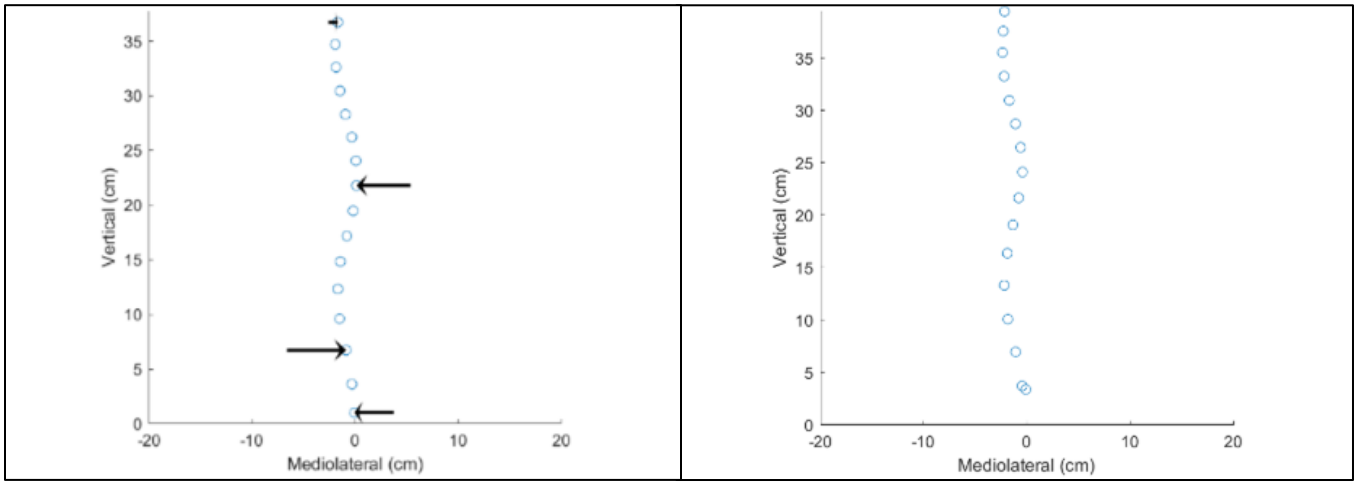

c d

F

Figure A-2. Subject 5. a) postero-anterior radiograph with a 44° right thoracic curve and 27° left thoracolumbar-lumbar curve, b) the extracted geometry plot with a thoracic Cobb angle of 25° and a thoracolumbar-lumbar Cobb angle of 21°, c) the simulated results of the optimized plot with a thoracic Cobb angle of 24° and a thoracolumbar-lumbar Cobb angle of 25° and d) the actual in-brace radiograph with a thoracic Cobb angle of 26° and a thoracolumbar-lumbar Cobb angle of 21°. The patient's deviation criterion improved by 40%.

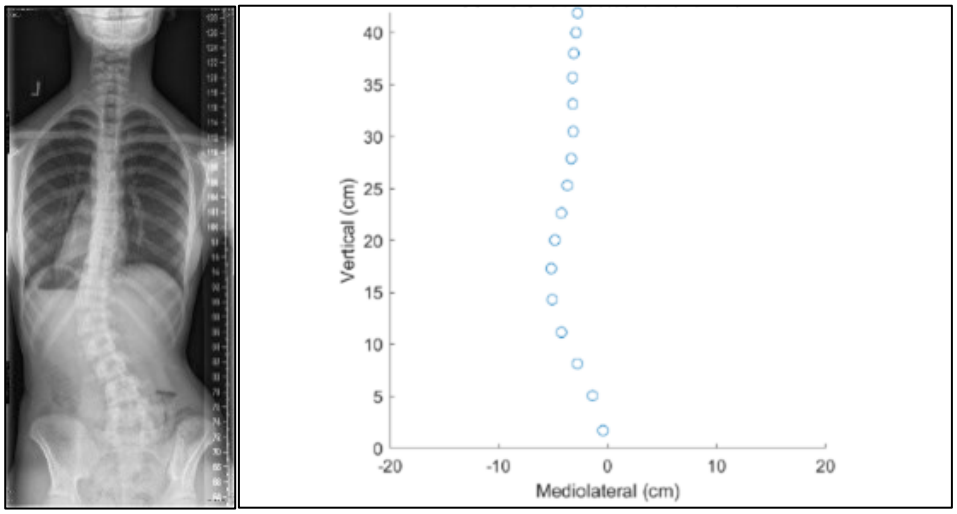

a b

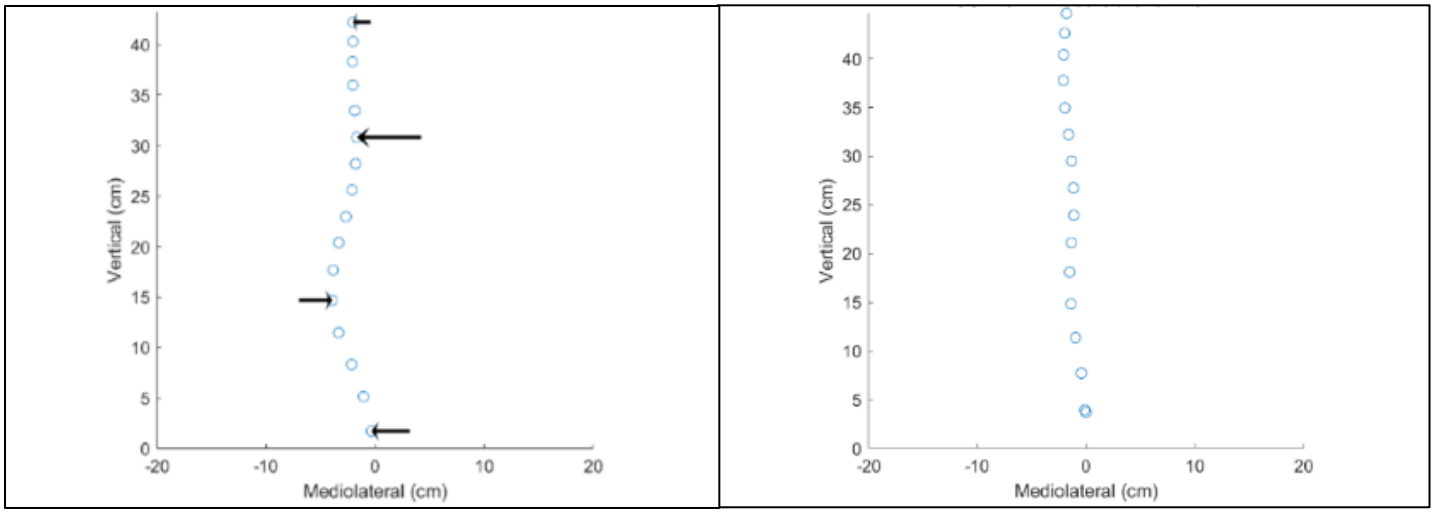

c d

Figure A-3. Subject 6. a) postero-anterior radiograph with a 33° left thoracolumbar-lumbar curve, b) the extracted geometry plot with a thoracolumbar-lumbar Cobb angle of 28°, c) the simulated results of the optimized plot with a thoracolumbar-lumbar Cobb angle of 29° and d) the actual in-brace radiograph with a thoracolumbar-lumbar Cobb angle of 27°. The patient's deviation criterion improved by 45%.

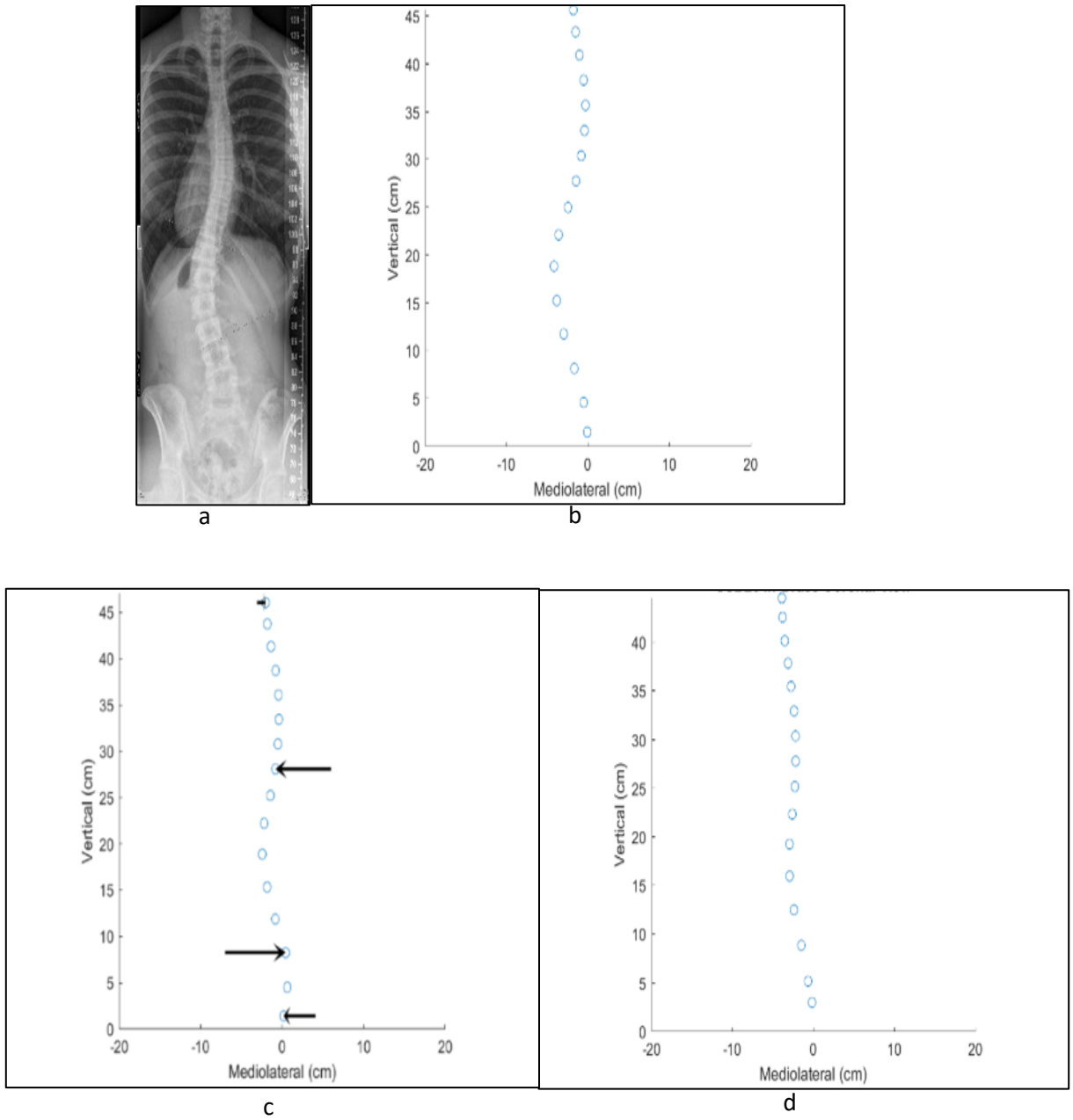

Figure A-4. Subject 7. a) postero-anterior radiograph with a 29° right thoracic curve and 37° left thoracolumbar-lumbar curve, b) the extracted geometry plot with a thoracic Cobb angle of 45° and a thoracolumbar-lumbar Cobb angle of 42°, c) the simulated results of the optimized plot with a thoracic Cobb angle of 16° and a thoracolumbar-lumbar Cobb angle of 17° and d) the actual in-brace radiograph with a thoracic Cobb angle of 16° and a thoracolumbar-lumbar Cobb angle of 17°. The patient's deviation criterion improved by 45%.

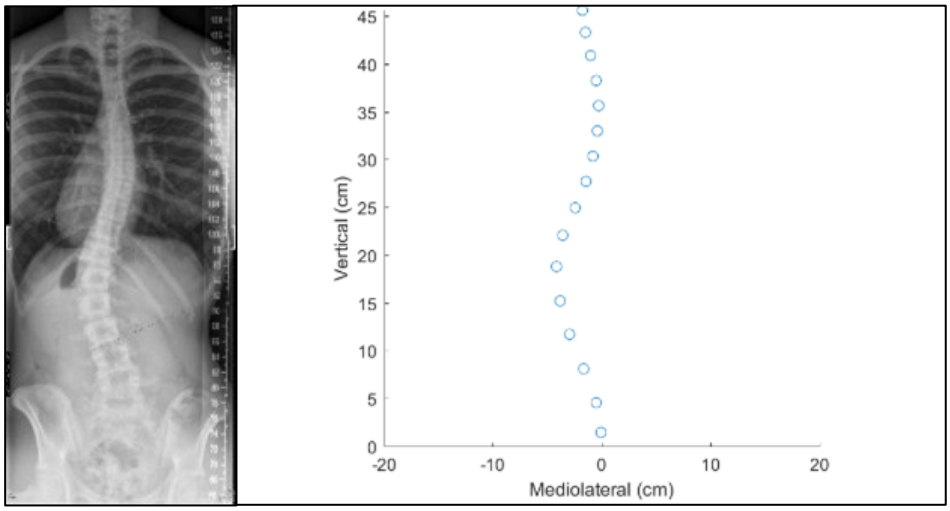

a b

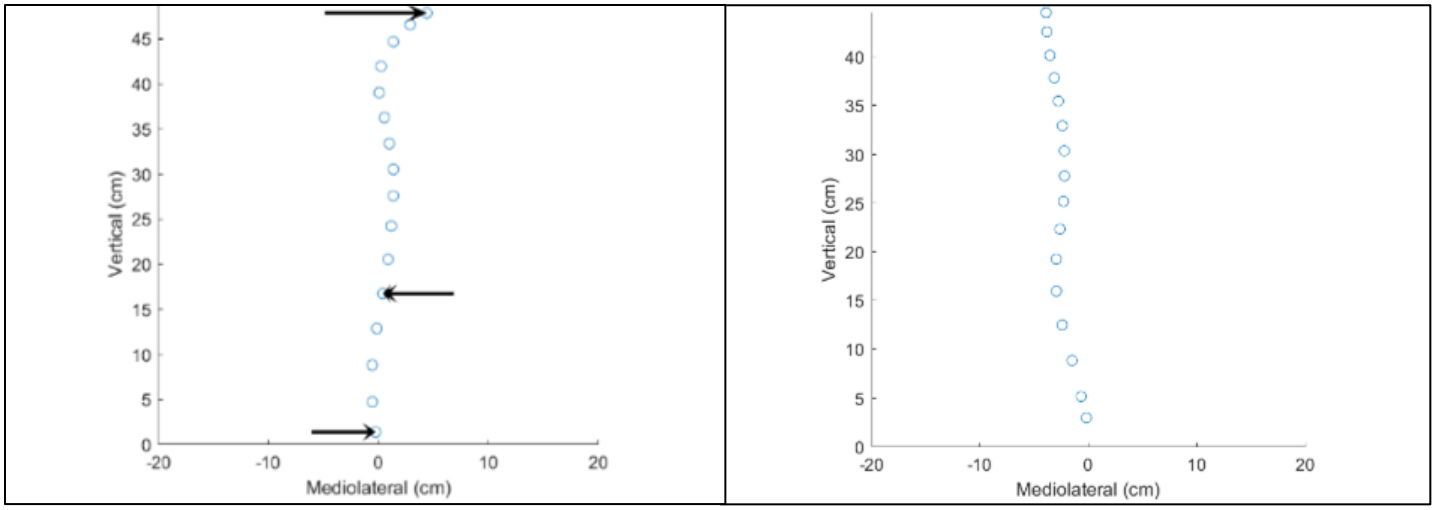

c d

Figure A-5. Subject 8. a) postero-anterior radiograph with a3° right thoracic curve and 30° left thoracolumbar-lumbar curve, b) the extracted geometry plot with a thoracic Cobb angle of 26° and a thoracolumbar-lumbar Cobb angle of 26°, c) the simulated results of the optimized plot with a thoracic Cobb angle of 39° and a thoracolumbar-lumbar Cobb angle of 19° and d) the actual in-brace radiograph with a thoracic Cobb angle of 36° and a thoracolumbar-lumbar Cobb angle of 26°. The patient's deviation criterion improved by 58%.

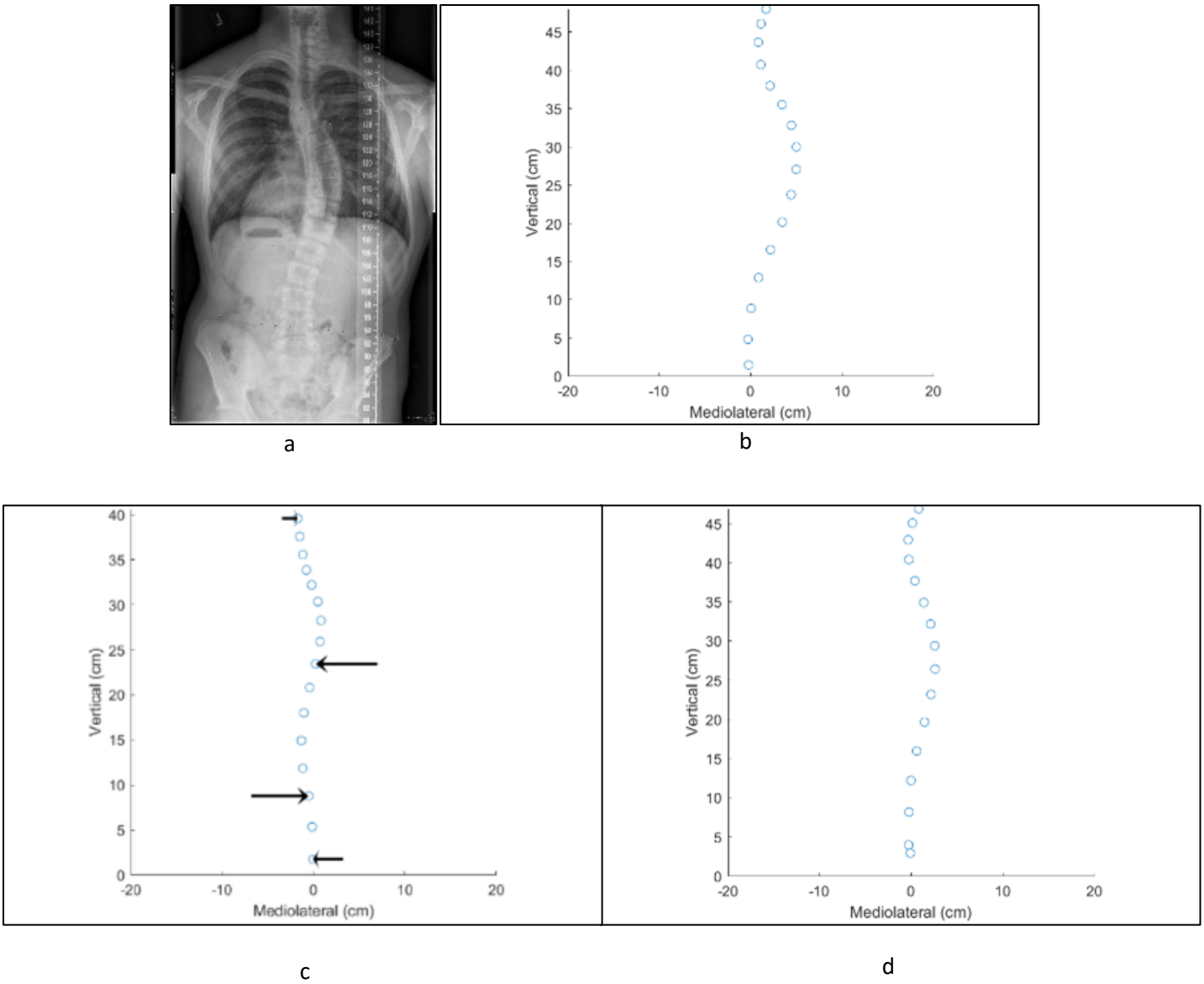

Figure A-6. Subject 9. a) postero-anterior radiograph with a 44° right thoracic curve and 27° left thoracolumbar-lumbar curve, b) the extracted geometry plot with a thoracic Cobb angle of 37° and a thoracolumbar-lumbar Cobb angle of 11°, c) the simulated results of the optimized plot with a thoracic Cobb angle of 24° and a thoracolumbar-lumbar Cobb angle of 25° and d) the actual in-brace radiograph with a thoracic Cobb angle of 26° and a thoracolumbar-lumbar Cobb angle of 21°. The patient's deviation criterion improved by 40%.

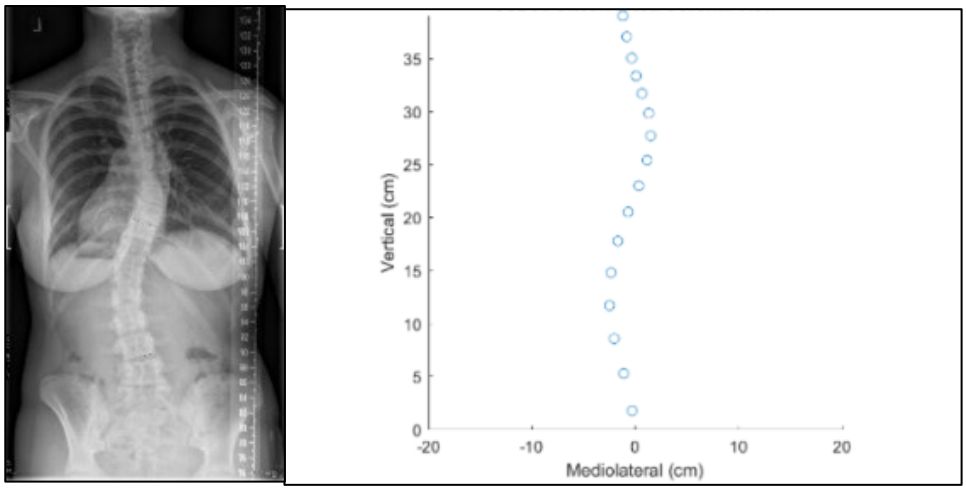

a b

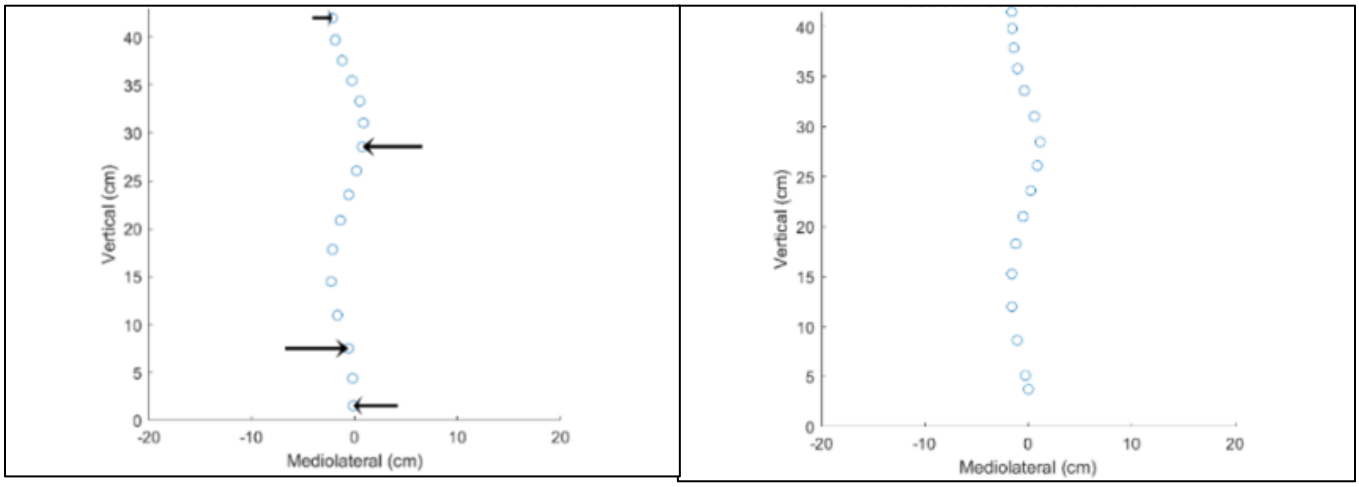

c d

Figure A-7. Subject 10. a) postero-anterior radiograph with a 24° right thoracic curve and 28° left thoracolumbar-lumbar curve, b) the extracted geometry plot with a thoracic Cobb angle of 31° and a thoracolumbar-lumbar Cobb angle of 11°, c) the simulated results of the optimized plot with a thoracic Cobb angle of 18° and a thoracolumbar-lumbar Cobb angle of 13° and d) the actual in-brace radiograph with a thoracic Cobb angle of 13° and a thoracolumbar-lumbar Cobb angle of 3°. The patient's deviation criterion improved by 38%.

Appendix B: MATLAB Code for Simulation

Section 1: Iterator.

This section runs the loop to calculate the results for all of the subjects and then performs statistical analysis on it. It takes no input, instead being hardcoded with the patient data; this is easily changed and used here simply for ease of operation. It runs the function DispFunction (Section 2) with iterated force values.

```
function [Pad, FergT, FergL, Cond, deltaSim, deltaAct, CCondR2, Alpha] = Iterator()

tic

%Pads holds the 7 pads: Pad(1,N)=ForceR; Pad(2,N)=Force1, Pad(3,N)=Position
%1, Pad(4,N)=Force2 ...
Pad=zeros(8,7);
%Ferg holds the Ferguson values for each set
FergT=zeros(8,1);
FergL=zeros(8,1);
%Alpha holds the alpha values. Alpha(1,N)=lumbar alpha,
%Alpha(2,N)=thoracic alpha
Alpha=zeros(8,2);
%OC holds original condition
OC=zeros(8,1);

CobbMIAS=[24  9          ; %R
38        23        ; %L
21        25        ;
27        21        ;
29        16        ;
37        17        ;
34        36        ;
```

```
30      26      ;
39      31      ;
33      16      ;
24      13      ;
28      3       ;
13      8       ;
25      5       ;
44      26      ;
42      21      ];

for i=5:-1:1
   %guess range is oldGuess+-14*i
   [Pad(1,:), FergT(1,:), FergL(1,:), Cond(1,:), Alpha(1,:),
OC(1,:)]=DispFunction(8,10,14,1,5,8,'USB25',15.4,-19.5,9.7,6.2,[Pad(1,2),Pad(1,4),Pad(1,6)],i); %RB LB RF
LF
   [Pad(2,:), FergT(2,:), FergL(2,:), Cond(2,:), Alpha(2,:),
OC(2,:)]=DispFunction(7,10,11,1,5,7,'USB24',26.5,-32.2,3.6,25.4,[Pad(2,2),Pad(2,4),Pad(2,6)],i);
   [Pad(3,:), FergT(3,:), FergL(3,:), Cond(3,:), Alpha(3,:),
OC(3,:)]=DispFunction(9,11,16,1,5,9,'USB26',19.3,-25,8.9,4.1,[Pad(3,2),Pad(3,4),Pad(3,6)],i);
   [Pad(4,:), FergT(4,:), FergL(4,:), Cond(4,:), Alpha(4,:),
OC(4,:)]=DispFunction(12,15,16,3,9,12,'USB27',12.9,-12.9,11,11,[Pad(4,2),Pad(4,4),Pad(4,6)],i);
   [Pad(5,:), FergT(5,:), FergL(5,:), Cond(5,:), Alpha(5,:),
OC(5,:)]=DispFunction(7,10,15,1,4,7,'USB31',11.5,-23.8,8.9,6.9,[Pad(5,2),Pad(5,4),Pad(5,6)],i);
   [Pad(6,:), FergT(6,:), FergL(6,:), Cond(6,:), Alpha(6,:),
OC(6,:)]=DispFunction(7,11,15,1,5,7,'USB32',15.8,-27.,2.1,15.3,[Pad(6,2),Pad(6,4),Pad(6,6)],i);
   [Pad(7,:), FergT(7,:), FergL(7,:), Cond(7,:), Alpha(7,:), OC(7,:)]=DispFunction(6,8,10,1,3,6,'FB01',21.6,-
17.1,10.0,18.2,[Pad(7,2),Pad(7,4),Pad(7,6)],i);
   [Pad(8,:), FergT(8,:), FergL(8,:), Cond(8,:), Alpha(8,:),
OC(8,:)]=DispFunction(8,11,15,1,5,8,'USB21',16.5,-13.6,5.8,15.2,[Pad(8,2),Pad(8,4),Pad(8,6)],i);
end

Length=length(CobbMIAS);
```

```
deltaSim=((CobbMIAS(1:2:Length,1)-FergT)./CobbMIAS(1:2:Length,1) + (CobbMIAS(2:2:Length,1)-
FergL)./CobbMIAS(2:2:Length,1))/2;
deltaAct=((CobbMIAS(1:2:Length,1)-CobbMIAS(1:2:Length,2))./CobbMIAS(1:2:Length,1) +
(CobbMIAS(2:2:Length,1)-CobbMIAS(2:2:Length,2))./CobbMIAS(2:2:Length,1))/2;

R=corrcoef(deltaSim,deltaAct);

CCondR2=R(1,2)^2;

toc

end
```

Section 2: Main Calculating Function

This uses the force inputs from Iterator to calculate the optimal brace position and force value. It runs geometryZ (Section 3) to determine the shape of the spine; AlphaFinder (Section 4) to personalize the spine stiffness; and FergPoints (Section 5) to determine the Cobb angle proxy.

```
function [Pad, FergR, FergL, Condition, Alpha, geo.OC] =
DispFunction(PBR,PMR,PTR,PBL,PML,PTL,geoName,T1DispR,T1DispL,flexR,flexL,oldValue,i)

divisions=5;
spineRange=10;
N1=divisions^3*spineRange^3;
N2=2*N1;
NP1=N1/spineRange;
NP2=NP1/spineRange;
NP3=NP2/spineRange;
NF12=spineRange^2*divisions/2;
NF1=N1/(NF12*divisions);
NF22=NF12*divisions/2;
NF2=N1/(NF22*divisions);
NF32=N1/divisions;

%imports geometry from USB24 X-ray data; uses csvread; L5 centroid is at
%0,0
geo=geometryZ(geoName);

%extracts info from geo; Centroid, T1 lateral displacement, centre of
%joints in the vertical direction, ignoring L5-S1
COJZ=geo.COJZ(2:17);

geoCorr=geometryCorrected(geoName);
TCGeoCorr=[geoCorr.Y geoCorr.Z];
```

```
%generates Pos matrices as
% 1 2 3 4 5
% 1 1 1 1 1 2 2 2 2 2
% 1 1 1 1 1 1 1 1 1 2 etc.
Pos1=single(repmat(sort(repmat(1:10,1,1)),1,NP1));
Pos2=single(repmat(sort(repmat(2:11,1,spineRange)),1,NP2));
Pos3=single(repmat(sort(repmat(2:11,1,spineRange^2)),1,NP3));

Force1Min=oldValue(1)-14*i;
if Force1Min < -70
   Force1Min = -70;
end
Force1Max=oldValue(1)+14*i;
if Force1Max > 70
   Force1Max = 70;
end
Force2Min=oldValue(2)-14*i;
if Force2Min < -70
   Force2Min = -70;
end
Force2Max=oldValue(2)+14*i;
if Force2Max > 70
   Force2Max = 70;
end
Force3Min=oldValue(3)-14*i;
if Force3Min < -70
   Force1Min = -70;
end
Force3Max=oldValue(3)+14*i;
if Force3Max > 70
   Force3Max = 70;
end
```

```
%generates Force matrices, same as Pos
Force1=single(repmat(sort(repmat(linspace(Force1Min,Force1Max,divisions),1,NF12)),1,NF1));
Force2=single(repmat(sort(repmat(linspace(Force2Min,Force2Max,divisions),1,NF22)),1,NF2));
Force3=single(sort(repmat(linspace(Force3Min,Force3Max,divisions),1,NF32)));

%Force=[Force1; Force2; Force3];

ForceR=-Force1-Force2-Force3;

%generates centre-of-joint matrices for generating moments
COJZ1Mat = single(repmat(COJZ(Pos1),1,16)');
COJZ2Mat = single(repmat(COJZ(Pos2),1,16)');
COJZ3Mat = single(repmat(COJZ(Pos3),1,16)');

%COJZ matrix for comparisons
COJZMat = single(repmat(COJZ,1,N1));

M1=(COJZMat >= COJZ1Mat).*(Force1.*(COJZMat-COJZ1Mat));
M=M1;
clear M1
M2=(COJZMat >= COJZ2Mat).*(Force2.*(COJZMat-COJZ2Mat));
M=M+M2;
clear M2
M3=(COJZMat >= COJZ3Mat).*(Force3.*(COJZMat-COJZ3Mat));
M=M+M3;
clear M3

% Pos1(:,909711)
% Pos2(:,909711)
% Pos3(:,909711)
%
```

```
% Force1(:,909711)
% Force2(:,909711)
% Force3(:,909711)
% ForceR(:,909711)
%
% MR(:,909711)
%
% M(:,909711)

clear COJZ1Mat COJZ2Mat COJZ3Mat COJZL4Mat COJZT1Mat COJZMat

[alphaR, alphaL] = AlphaFinder(geo,PBR,PMR,PTR,PBL,PML,PTL,T1DispR,T1DispL,flexR,flexL);

Alpha=[alphaR, alphaL];

%stiffness matrix for one-dimensional torsion springs; alpha1 and alpha2
%are in place to adjust stiffnesses for particular patients
K=[alphaL*6400+alphaL*9700   -alphaL*9700   0        0        0        0        0        0        0
        0        0        0        0        0        0        0        ;
-alphaL*9700   alphaL*9700+alphaL*9500   -alphaL*9500   0        0        0        0        0
        0        0        0        0        0        0        0        ;
0        -alphaL*9500   alphaL*9500+alphaL*11400   -alphaL*11400  0        0        0        0
        0        0        0        0        0        0        0        ;
0        0        -alphaL*11400  alphaL*11400+alphaR*9900    -alphaR*9900   0        0        0
        0        0        0        0        0        0        0        ;
0        0        0        -alphaR*9900   alphaR*9900+alphaR*11000    -alphaR*11000  0        0
        0        0        0        0        0        0        0        ;
0        0        0        0        -alphaR*11000  alphaR*11000+alphaR*19700   -alphaR*19700  0
        0        0        0        0        0        0        0        ;
0        0        0        0        0        -alphaR*19700  alphaR*19700+alphaR*12200   -alphaR*12200
        0        0        0        0        0        0        0        ;
```

```
0 0 0 0 0 0 -alphaR*12200 alphaR*12200+alphaR*14300 -
alphaR*14300 0 0 0 0 0 0 0 ;
0 0 0 0 0 0 0 -alphaR*14300 alphaR*14300+alphaR*23900
-alphaR*23900 0 0 0 0 0 0 ;
0 0 0 0 0 0 0 0 -alphaR*23900
alphaR*23900+alphaR*12200 -alphaR*12200 0 0 0 0 0 ;
0 0 0 0 0 0 0 0 0 -alphaR*12200
alphaR*12200+alphaR*15800 -alphaR*15800 0 0 0 0 ;
0 0 0 0 0 0 0 0 0 0 -alphaR*15800
alphaR*15800+alphaR*18700 -alphaR*18700 0 0 0 ;
0 0 0 0 0 0 0 0 0 0 0 -alphaR*18700
alphaR*18700+alphaR*19100 -alphaR*19100 0 0 ;
0 0 0 0 0 0 0 0 0 0 0 0 -
alphaR*19100 alphaR*19100+alphaR*13500 -alphaR*13500 0 ;
0 0 0 0 0 0 0 0 0 0 0 0 0
-alphaR*13500 alphaR*13500+alphaR*21000 -alphaR*21000 ;
0 0 0 0 0 0 0 0 0 0 0 0 0
0 -alphaR*21000 alphaR*21000];

%Rotation R=inv(Stiffness K)*moment M
R=K\M(1:16,:);

%clear M

%Generates matrix for original geometry
CentroidRep=single(repmat(geo.Centroid(:,:),1,N1));

%turns original geometry into a difference between vertebra N and vertebra N-1
Vector1(1,:) = single(repmat(geo.Centroid(1,:),1,N2));
Vector1(2:16,1:2:N2) = single(diff(CentroidRep(:,1:2:N2)));
Vector1(2:16,2:2:N2) = single(diff(CentroidRep(:,2:2:N2)));
```

```
%generates cos and sin for R matrix for used in 2D rotation matrix
RotMat=single(zeros(16,N2));

RotMat(:,1:2:N2)=cos(R);
RotMat(:,2:2:N2)=sin(R);

%2D rotation matrix; Xnew=xcos -ysin; Ynew=xsin+ycos
Vector2(:,1:2:N2)=single(Vector1(:,1:2:N2).*RotMat(:,1:2:N2) - Vector1(:,2:2:N2).*RotMat(:,2:2:N2));
Vector2(:,2:2:N2)=single(Vector1(:,1:2:N2).*RotMat(:,2:2:N2) + Vector1(:,2:2:N2).*RotMat(:,1:2:N2));

%empty translated centroid matrix
TC=single(zeros(16,N2));

%adds differences back up to generate final positions
TC(:,1:2:N2)=cumsum(Vector2(:,1:2:N2));
TC(:,2:2:N2)=cumsum(Vector2(:,2:2:N2));

Cond=sum(abs(TC(:,1:2:N2)));

InRangeCond = (min(TC(:,2:2:N2)) < 0);
Cond(InRangeCond) = 1000;

%finds minimumvalue of condition and its location
[~, minidx] = min(Cond);

%extracts forces and positions of forces
ForceR=ForceR(minidx);
Force1=Force1(minidx);
Force2=Force2(minidx);
Force3=Force3(minidx);
Pos1=Pos1(minidx);
Pos2=Pos2(minidx);
```

```
Pos3=Pos3(minidx);

Pad(1)=ForceR;
Pad(2)=Force1;
Pad(3)=Pos1;
Pad(4)=Force2;
Pad(5)=Pos2;
Pad(6)=Force3;
Pad(7)=Pos3;

Condition = Cond(minidx);

Moment=M(:,minidx);

FergL=FergPoints(TC(PBL,minidx*2-1:minidx*2),TC(PML,minidx*2-1:minidx*2),TC(PTL,minidx*2-
1:minidx*2));
FergR=FergPoints(TC(PBR,minidx*2-1:minidx*2),TC(PMR,minidx*2-1:minidx*2),TC(PTR,minidx*2-
1:minidx*2));

scatter(TC(:,minidx*2-1),TC(:,minidx*2));
axis square
axis([-20 20 0 inf])
title([geoName ' Corrected Coronal View']);
xlabel('Mediolateral (cm)');
ylabel('Vertical (cm)');
saveas(gcf,[geoName ' 2 Corrected'],'png');

scatter(geoCorr.Y,geoCorr.Z);
axis square
axis([-20 20 0 inf])
title([geoName ' In-Brace Coronal View']);
xlabel('Mediolateral (cm)');
```

```
ylabel('Vertical (cm)');
saveas(gcf,[geoName ' 3 IBC'],'png');

end
```

Section 3: geometryZ

Outputs spinal geometry.

```
function [geo] = geometryZ(geoName)
%Extracts info from geometry set named 'geoName' (.csv)
%T1Disp is lateral displacement of T1 centroid in left bending ultrasound
%flex1 is top curve magnitude in bending ultrasound, flex2 is lower curve

% Vertebra number       Centroid          COJ     Joint number
% T2            16        T1-T2       17
% T3            15        T2-T3       16
% T4            14        T3-T4       15
% T5            13        T4-T5       14
% T6            12        T5-T6       13
% T7            11        T6-T7       12
% T8            10        T7-T8       11
% T9            9         T8-T9       10
% T10            8         T9-T10     9
% T11            7         T10-T11    8
% T12            6         T11-T12    7
% L1            5         T12-L1      6
% L2            4         L1-L2       5
% L3            3         L2-L3       4
% L4            2         L3-L4       3
% L5            1         L4-L5       2
%                         L5-S1       1

GeoDataRaw = csvread([geoName ' Measure.csv'],1,1);

GeoDataYZ(:,1) = GeoDataRaw(6:73,1);
GeoDataYZ(1,2) = GeoDataRaw(3,2)-GeoDataRaw(6,2);
GeoDataYZ(2:68,2) = GeoDataRaw(3,2) - GeoDataRaw(7:73,2);
```

```
ScaleFactorYZ = abs(2 / (GeoDataRaw(1,2)-GeoDataRaw(2,2)));

COJY = zeros(17,1);

for i = 1:17
   COJY(i) = (GeoDataYZ(i*4-3,1) + GeoDataYZ(i*4-2,1) + GeoDataYZ(i*4-1,1) +
GeoDataYZ(i*4,1))/4*ScaleFactorYZ;
end

COJYMat=COJY(1)*ones(17,1);

COJY=COJY-COJYMat;

COJZ = zeros(17,1);

for i = 1:17
   COJZ(i) = (GeoDataYZ(i*4-3,2) + GeoDataYZ(i*4-2,2) + GeoDataYZ(i*4-1,2) +
GeoDataYZ(i*4,2))/4*ScaleFactorYZ;
end

COJZMat=COJZ(1)*ones(17,1);

COJZ=COJZ-COJZMat;

HOJZ=zeros(17,1);

for i=1:17
   HOJZ(i) = (-GeoDataYZ(i*4-3,2) - GeoDataYZ(i*4-2,2) + GeoDataYZ(i*4-1,2) + GeoDataYZ(i*4,2))/4 *
ScaleFactorYZ;
end
```

```
WOJY=zeros(17,1);

for i=1:17
   WOJY(i) = (GeoDataYZ(i*4-3,1) - GeoDataYZ(i*4-2,1) - GeoDataYZ(i*4-1,1) + GeoDataYZ(i*4,1))/4 *
ScaleFactorYZ;
end

Centroid = zeros(16,2); %(y,z)

for i = 1:16
   Centroid(i,1) = (COJY(i) + COJY(i+1))/2; %y
   Centroid(i,2) = (COJZ(i) + COJZ(i+1))/2; %z
end

Y = Centroid(:,1);
Z = Centroid(:,2);

%Y-Z plane is coronal

OSpace=linspace(0,1,16)';
OLin=OSpace.*COJY(17);
OC=sum(abs(COJY(2:17)-OLin));

geo = struct('Centroid',Centroid,'Y',Y,'Z',Z,'COJY',COJY,'COJZ',COJZ,'HOJZ',HOJZ,'WOJY',WOJY,'OC',OC);

scatter(Y,Z);
axis square
axis([-20 20 0 inf])
title([geoName ' Uncorrected Coronal View']);
xlabel('Mediolateral (cm)');
ylabel('Vertical (cm)');
saveas(gcf,[geoName ' 1 Uncorrected'],'png');
```

```
end
```

Section 4: AlphaFinder

This personalizes the stiffness of the spine to the individual patient and outputs multipliers to apply to the cadaver stiffness values.

```
function [alphaL, alphaR] = AlphaFinder(geo,PBR,PMR,PTR,PBL,PML,PTL,T1DispR,T1DispL,flexR,flexL)
%finds stiffness matrix coefficient from data taken from bending ultrasound

%PBR->PTL are important vertebrae measured from L5
%T1DispR/L are the displacements of T1 relative to L5 in the bending
%diagram
%flexR/L are the measured flexibility curve angles

alphaLInit=1;
alphaRInit=1;

options=optimset('TolFun',0.01,'TolX',0.01,'MaxFunEvals',10000,'MaxIter',10000,'Display','off');

[shearR]=fmincon(@(V) testForceA(V(1),geo,T1DispR,alphaRInit,alphaLInit),[-30],[],[],[],[],[-70],[-
10],[],options);

[alphaR]=fmincon(@(AR)
testForceB(shearR,AR(1),alphaLInit,geo,PBR,PMR,PTR,flexR),alphaRInit,[],[],[],[],0.1,10,[],options);

% testR = testForceCR(shearR,alphaR,alphaLInit,geo,PBR,PMR,PTR,flexR);
%
% if testR == 0
%     alphaR = alphaRInit;
% end

alphaLInit=1;
```

```
[shearL]=fmincon(@(V)
testForceA(V(1),geo,T1DispL,alphaR,alphaLInit),[30],[],[],[],[],[10],[70],[],options);

[alphaL]=fmincon(@(AL)
testForceB(shearL,alphaR,AL,geo,PBL,PML,PTL,flexL),alphaLInit,[],[],[],[],0.1,100,[],options);

% test = testForceCL(shearL,alphaR,alphaL,geo,PBL,PML,PTL,flexL);
%
% if test == 0
%     alphaL = alphaLInit;
% end

end
```

Section 5: Fergpoints

This determines the proxy Cobb angle.

```
function [Ferg] = FergPoints(TC1,TC2,TC3)

%finds Ferguson angle for three points

FergusonRaw = zeros(2,1);

FergusonRaw(1) = atan((TC1(2)-TC2(2))/(TC1(1)-TC2(1)));
FergusonRaw(2) = atan((TC2(2)-TC3(2))/(TC2(1)-TC3(1)));

for i = 1:2
   if FergusonRaw(i) < 0
      FergusonRaw(i) = pi + FergusonRaw(i);
   end
end

Ferguson = abs(FergusonRaw(1) - FergusonRaw(2));

Ferg = Ferguson*180/pi*1.35;

end
```